Title
Study of Porous Adsorbents for Carbon Capture via Molecular Simulation

Author
Swisher, Joseph Andrew

Publication Date
2012

Peer reviewed|Thesis/dissertation

Study of Porous Adsorbents for Carbon Capture via Molecular Simulation

by

Joseph Andrew Swisher

A dissertation submitted in partial satisfaction of the
requirements for the degree of
Doctor of Philosophy

in

Chemical Engineering

in the

Graduate Division

of the

University of California, Berkeley

Committee in charge:

Prof. Berend Smit, Chair
Prof. Alexis Bell
Prof. Jhih-Wei Chu
Prof. Martin Head-Gordon

Fall 2012

Study of Porous Adsorbents for Carbon Capture via Molecular Simulation

Abstract

Study of Porous Adsorbents for Carbon Capture via Molecular Simulation

by

Joseph Andrew Swisher

Doctor of Philosophy in Chemical Engineering

University of California, Berkeley

Prof. Berend Smit, Chair

Increasing atmospheric CO_2 levels are of concern due to potential links to negative environmental impacts such as increasing global temperatures and ocean acidification. Strategies for reducing CO_2 emissions involve both reducing the use of fossil fuels a primary energy sources and employing processes to capture CO_2 from gas streams incidental to energy generation and store in deep geologic features. The one of the main targets for CO_2 separation are post-combustion gas streams at electricity generating plants, which represent a large fraction of the CO_2 emitted. While current process technology (amine scrubbing) could be scaled to the accomplish the task, it is a relatively inefficient process and would substantially reduce the efficiency of electricity generation. Adsorption-based processes have the potential to reduce the parasitic load on generating plants by reducing the amount and quality of heat diverted from generating cycle.

Adsorption processes involve the use of solid porous materials with large internal surface areas to separate components of a gas mixture. One or more components will preferentially adsorb and be enriched in the adsorbed mixture, which can then be desorbed in a separate part of the process. While a variety of adsorbents have wide application in industry, there is a need to identify the most efficient materials for this process to ensure its economic viability. Some materials of interest are zeolites and metal-organic frameworks, and recent experimental and theoretical work have identified thousands of possible new materials. To evaluate this large range of materials, molecular simulation techniques useful for quickly generating thermodynamic data and understanding the molecular-level mechanisms responsible for selectivity.

This work details efforts addressing several aspects using Monte Carlo simulations to evaluate different materials for CO_2 separations. One aspect is the proper description of how mixtures adsorb in materials with heterogeneous surfaces where components can competitively adsorb at spatially distinct sites. By applying ideal adsorbed solution theory (IAST) to separate Langmuir sites, it is possible to improve predictions of mixture adsorption isotherms compared to applying IAST to the whole isotherm. One critical element of applying IAST accurately is ensuring the saturation loadings of different components in a

mixture are estimated as accurately as possible. Another part addresses how to apply simulation techniques to millions of related structures simultaneously and evaluate them with a simple model of generating plant performance. Using GPU-accelerated Monte Carlo simulations, a database containing thousands of hypothetical zeolite structures was screened for CO_2/N_2 separations, and many structures were identified that potentially would have a lower energy penalty to operate than the standard amine scrubbing process.

Next, a method for fitting parameters for a classical force field from ab initio calculations was developed and used to predict the adsorption of CO_2 in Mg-MOF-74, a promising MOF material for CO_2 separations. Using a modified Buckingham potential with an additional r^{-5} attractive term was able to describe the enhanced interaction between CO_2 molecules and the coordinative-unsaturated Mg atoms. Finally, the adsorption of water in zeolite 13X was studied, showing the strong effect it has on the co-adsorption of CO_2. Rearrangement of sodium cations in the zeolite pores was important for predicting the correct isotherms, and at the highest water loadings, some sodium cations are removed from the pore walls become coordinated by water closer to the center of the pore. This rearrangement may explain the the steep elbow of the isotherm.

Eliminate all other factors, and the one which remains must be the truth.

Sherlock Holmes, *The Sign of Four*

Contents

List of Figures

List of Tables

Acknowledgements

First of all, I would like to acknowledge the support provided by the University of California, Chevron, and the US Department of Energy's Energy Frontier Research Center (EFRC) and Advanced Research Projects Agency ENERGY (ARPA-e) programs. Thank you for making this work possible.

I would like to say thanks to all the wonderful scientists I have had the pleasure of working with during our tenures in the MolSim group. Thanks also to Bei, Jocelyn, Manju, An, Forrest, Ayelet, Roberta, Jihan, Sergey, Fangyong, and Li-Chiang for being great officemates and collaborators. A special thanks to Nils for being a fantastic host and a wonderful guest.

I have had the pleasure of working with several gifted undergraduates during my grad school career. Thank you to Matilda, Anthony, Abe, Theo, Brian, and Christián for doing great work and helping me appreciate the challenges of directing research.

I would also like to say thank you to Jon for helping keep all the computers in order and to Drew and Kristin for helping manage the business of the group. It certainly made my life easier.

Let me thank Prof. Smit for the 5 years of great advising. It was great to have the opportunities to work on all the projects I did and explore what interested me. Thanks also to Prof. Bell for advising me during the early part of my graduate school career. It was a pleasure to collaborate on our common projects and I learned a lot about how to conduct scientific investigation.

Thank you as well to Frederick and Anne. It was a real pleasure getting to know you and sharing your table, which always had a delicious meal on it. Thank you to Mom, Dad, and Nick for the years of encouragement and support that allowed me to get to this point. Finally, let me say thank you to Casey for your patience and support during these past months as many a weekend and evening were consumed with writing.

Chapter 1

Introduction

This dissertation is motivated by the study of porous adsorbents for the removal of CO_2 from post-combustion gases. It covers the use of molecular simulation to predict relevant thermodynamic data for the evaluation of materials and the design of adsorption processes. Grand canonical Monte Carlo simulations were used to predict adsorption isotherms for CO_2 and other gases in zeolites and other nanoporous adsorbents, as well as other simulation techniques to predict relevant thermodynamic properties. Molecular simulation also provides a molecular-scale picture of the adsorbate molecules and their siting and structure within the pores of the material.

1.1 CO_2 in the atmopshere

The concentration of carbon dioxide in the atmosphere has increased Y fold over the past century. Figure 1.1 shows the atmospheric concentration of CO_2 measured since 1959 at Mauna Loa in Hawaii.[1] The annual periodicity in the concentration of CO_2 is superimposed on the monotonic increasing trend in the average concentration. This increase is primarily due to the combustion of fossil fuels (i.e. coal, petroleum, and natural gas), as evidenced by studies of the decreasing O_2 concentration and isotopic composition of atmospheric CO_2.[2,3] The increase in CO_2 concentration has been implicated in the increase in average global temperatures over the past 3 decades.[4] Because CO_2 absorbs (weakly) some of the infrared radiation that would otherwise be radiated back into space an re-emits is back towards the surface, the surface temperature of the Earth is greater than would otherwise be expected from a radiation balance with the Sun.[5] Recent analysis by researchers at Berkeley have shown that this increase in temperature can be attributed to CO_2.[6]

Given the potential negative impacts of CO_2 emission, fossil fuel consumption is projected to continue to increase. Fossil fuels represent a cheap and abundant fuel source for many applications, particularly the combustion of coal for electricity generation. In the US, the EIA has projected that while coal will reduce in its share of total electricity production over the next half-century as renewables (i.e. biomass, wind, solar) increase in utilization,

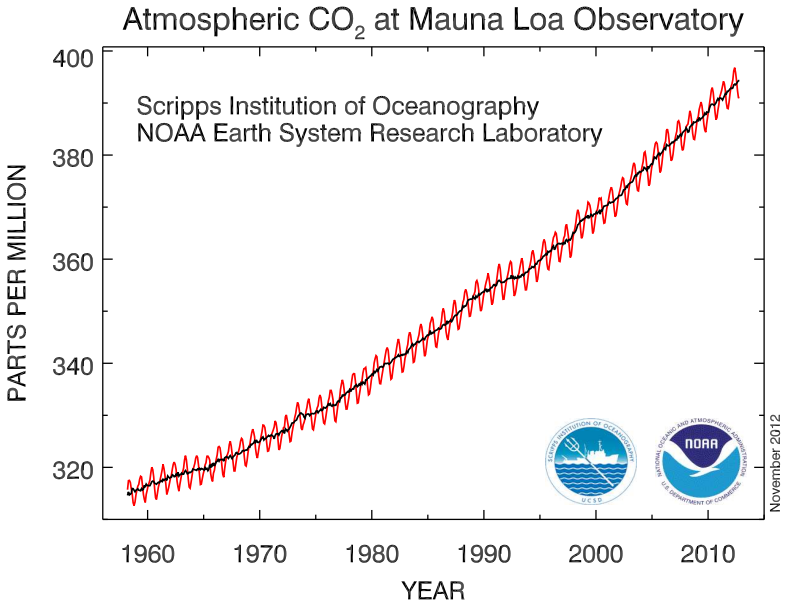

Figure 1.1: Atmospheric concentration of CO_2 measured at the Mauna Loa Observatory, Hawaii.[1]

the absolute tonnage of coal consumed will continue to increase.[7] In light of the accidental release of radioactive material resulting from the tsunami in Japan in 2011, some countries have committed to reducing or eliminating their use of nuclear power,[8,9] and fossil fuel-based generation will likely be required to replace the lost generation capacity. Studies performed by the Electric Power Research Institute have shown that any realistic strategy to reducing carbon dioxide emissions will require some form of carbon capture and sequestration.[10] In this process, CO_2 is separated from some point in the combustion processes, either pre- or post-combustion. Pre-combustion technologies usually involve the gasification of coal via the water-gas shift reaction.[11] This creates H_2, which is combusted to generate steam for the, and a high-purity CO_2 stream that can be cleaned-up and compressed. Post-combustion removal of CO_2 can occur from gas streams that are either rich or lean. Rich streams would result from oxy-combustion of fuels, where air is separated and nearly pure oxygen is fed to the combustor.[11] The resulting stream is mostly CO_2 and relatively easy to dehydrate and compress. Lean streams results from the standard method of combusting fossil fuels with air. The stream will end up at about 1 bar pressure, and 7-14% CO_2 (volume basis), depending on the fuel. The stream will likely be saturated with water an the balance of the gas will be nitrogen and trace impurities. While advanced technologies like gasification and oxyfuel combustion represent potentially useful technologies for newly built generation

plants, the installed base of fossil fuel-combusting generation plants are of the later type and identification of a low-cost technology to separate CO_2 from their effluent is of key importance should regulations require reductions in CO_2 emissions.

1.2 Processes for CO_2 separation

Removal of CO_2 from gas streams is a standard process in some industries. In particular, CO_2 separation of natural gas is an important separation in natural gas production because raw gas from the well often contains a significant amount of CO_2. The most common and robust process used for this separation is absorption via a concentrated aqueous solution of amines.[10–13] The gas stream containing CO_2 is passed through a column opposite the solvent stream. CO_2 dissolves in the solvent and rapidly reacts with the dissolved amine to form a carbamate species. The loaded solvent is then passed to a stripper column where it is heated to reverse the reaction and desorb the CO_2 from the solvent. The amine stream is then condensed and passed back to the absorber column. Heat integration is used extensively to improve the efficiency of the process, however, since a large volume of aqueous solvent is vaporized, it is by its very nature an energy intensive process.[13,14] The heat required for this process would necessarily have to be taken from the output of the plant The most common amine used is monoethanolamine. An additional disadvantage of amine scrubbing processes is that the amine will tend to react with trace impurities in the flue gas and form toxic side products which warrant additional capital investment for proper handling.

Other gas separation processes have been proposed to replace and potentially provide a more efficient method of separating CO_2 including membranes, novel solvents, and adsorption.[10,11] Membranes have the advantage of not requiring any thermal swing affect the separation. However, the low partial pressure of CO_2 and low permeance of existing membranes could require too much compression and/or vacuum to be feasible.[15] Advanced solvents attempt to dissolve a large amount of CO_2 without resorting to chemical reactions, as with amines, but are limited by the slow dissolution rate of CO_2.[16] Adsorption processes rely on differences in the adsorption for different components of a mixture on the surface or in the pores of a solid material. By swinging between different temperatures and/or pressures, very pure gas streams can be achieved. One potential advantage of adsorption processes is that the latent heat of the solvent need not be supplied and the process can be thermally more efficient. However, the required heat transfer and pressurization rates can be slow in packed beds.[17]

Evaluating a material for use as an adsorbent in a sorption process requires some thermodynamic data. The key measurements are the adsorption isotherm and the heat of adsorption. The adsorption isotherm is the amount of particular compound that adsorbs on the material at a fixed temperature and different partial pressures or fugacities of the compound. This can be measured at different temperatures and pressures to determine how the material performs at different conditions that could be visited in a process. The other primary thermodynamic measurement of interest is the heat of adsorption, the amount of

heat that is adsorbed when a given quantity of compounds adsorbs. In terms of the performance of material in real process, the heat of adsorption represents the amount of heat that may need to be supplied to cause a compound to desorb. Other measurements that can be derived from the pure component isotherms and heat of adsorption are the working capacity and mixture isotherms. The working capacity represents the difference in equilibrium loadings between the two state conditions a sorption process swings between and is the maximum practical amount of a compound that can be separated in a single cycle of a process. Because the accurate measurement of mixture adsorption isotherms are difficult, usually a thermodynamic-based model is used to interpolate pure component isotherms to arbitrary mixtures of components, the most common of these approaches being the ideal adsorbed solution theory. Chapter 2 goes into detail about the limits of the applicability of IAST for the mixtures of interest in CO_2 gas separations and some of the subtleties encountered when limited isotherm data is available.

1.3 Outline of dissertation

This dissertation addresses several aspects of using molecular simulations to evaluate porous materials for gas separations relevant to carbon capture. In brief, the chapters body of the dissertation deal with the following topics:

Chapter 2 deals with how isolated adsorption sites and the relative preference of different components in a mixture influence the proper way to model mixture adsorption. The use of a segregated mixture adsorption model provides a better description of adsorption than IAST in materials with spatially separate sites.

Chapter 3 details the use of rapid molecular simulations to evaluate thousands of materials simultaneously for CO_2-N_2 separation and a model for predicting the energy required to separate a single unit of CO_2. Several materials with lower energy penalties than amine scrubbing are identified.

Chapter 4 explains how ab initio calculations were used to parameterize a force field to study CO_2 adsorption in Mg-MOF-74, a promising new material with a high CO_2 selectivity at low partial pressure. Additional terms are required in the potential model to properly describe the interaction between Mg atoms and CO_2.

Chapter 5 shows how the presence of H_2O can dramatically reduce the capacity for CO_2 of zeolite 13X, an industrially relevant adsorbent with a high capacity for CO_2. The shape of the H_2O isotherms could be due to rearrangement of extra-framework sodium cations.

Before getting into the body of the dissertation, the introduction will conclude with some high-level background information on molecular simulation and porous adsorbents.

1.4 Molecular simulation

Molecular simulations have advanced in the last 20 years to become a powerful and widely applied tool to evaluate and study porous adsorbents for a variety of applications.[18] Monte Carlo techniques in particular have been useful for studying both pure components and mixtures of compounds adsorbing in a variety of porous materials, including zeolites,[18] MOFs,[19] ZIFs,[20] and COFs.[21] The natural ensemble for these simulations is the grand canonical ($\mu - V - T$) ensemble.[22] Typically, the partial pressures of components in a gas mixture can be selected and translated to a fugacity or chemical potential via an equation of state. The system is kept at a specified temperature and the atoms of the adsorbent are kept fixed, yielding a constant volume system. The crystal structure of the adsorbent is used directly and a simulation box is constructed out of a tiling of a few unit cells. Then, a Monte Carlo simulation is preformed where random moves of individual molecules are proposed and either accepted or rejected to generate configurations with the proper statistical weights so that averages of observed quantities can be taken as the equilibrium values. In grand canonical simulations, the moves used are typically include:

translation the translation of one molecule in the simulation box by a random vector

rotation the rotation in place of a single molecule in the simulation box

regrowth a single molecule already in the simulation box is removed and reinserted at a random location in the simulation box with a new random orientation or configuration, if it has internal degrees of freedom

swap a single molecule already in the simulation box is removed or a new molecule is inserted

The first three moves above correspond to the canonical ensemble (constant $N-V-T$), so they may be accepted or rejected based upon the following acceptance rule:

$$\mathrm{acc}(o \to n) = \min\left[1,\ \exp(-\beta(U_n - U_o))\right] \tag{1.1}$$

where o is the old configuration, n is the new configuration, β is the inverse temperature ($(k_bT)^{-1}$), and U_i is the energy of configuration i. When the particle number may change, the acceptance probability for inserting a new molecule is:

$$\mathrm{acc}(N \to N+1) = \min\left[1,\ \frac{V\beta f}{N+1}\exp(-\beta(U_{(N+1)} - U_N))\right] \tag{1.2}$$

and for removing a molecule:

$$\mathrm{acc}(N \to N-1) = \min\left[1,\ \frac{N}{V\beta f}\exp(-\beta(U_{(N-1)} - U_N))\right] \tag{1.3}$$

where N is the number of molecules of a given type, V is the volume, and f is the partial fugacity of the component.

In the equations above, the difference in energy between configurations is required. In principle, this energy difference may be specified or evaluated in any manner. Since millions of configurations must be visited to get proper thermodynamic averages, computationally simpler energy expressions are preferred. When studying porous materials, the energy is usually represented using a classical potential that is the typically the sum of a dispersive term and an electrostatic term, and the total energy is taken as a sum over all unique pairs of atoms in the system. The 12-6 Lennard-Jones potential is often used for the dispersive term, while the electrostatics are treated as interacting point charges via Coulomb's law. Due to the long-range nature of the Coulomb potential, the Ewald summation technique is used to allow the electrostatic potential summation to converge using a smaller system.[23] The collection of parameters and charges that parameterize these interactions is known as a force field and can be determined by fitting the results of molecular simulations to experimental data[24,25] or by fitting to a potential energy surface developed from quantum chemical calculations.[26,27]

1.5 Porous adsorbents

A variety of porous materials have been proposed as adsorbents for CO_2 separations via sorption processes. Some of the most promising materials are zeolites and metal-organic frameworks (MOFs). Zeolites are aluminosilicates with pore sizes on the order of one to a few molecular diameters. Aluminum and silicon a tetrahedrally coordinated by oxygen atoms and the tetrahedra are connected in distinct topologies. Formally, aluminum carries a +3 charge, compared to +4 for silicon. This difference gives the framework a net -1 charge for each aluminum, which is compensated by cations that reside in the pores of the material. These cations, typically from the alkali and alkaline earth metals, can be exchanged to provide specific functionality for a particular application, such as the exchange of calcium for sodium in zeolite 4A to reduce the average pore diameter.[28] MOFs are novel materials made of rigid organic molecules that connect metal atoms of clusters in networks with a rich variety of topologies.[29,30] The prototypical porous MOF, MOF-5,[30] and the MTV-MOFs based on its structure,[31] illustrates the chemical customizability that is a key aspect the interest in these materials. Because the materials are primarily made of organic molecules, the chemistry of the pore surfaces can be customized via the addition of functional groups to enhance adsorption properties. One class of MOFs of particular interest to adsorption are the zeolitic imidazolate frameworks (ZIFs), which are composed of tetrahedral networks of imidazole-based molecules and metal atoms, and have some of the same topologies of the aluminosilicate zeolites.[32] Some of these materials have stability with respect to harsh chemical environments, a property that may make them good materials for post-combustion CO_2 separations.[32]

Chapter 2

Evaluating mixture adsorption models using molecular simulation

Predicting mixture adsorption isotherms is of primary importance in the evaluation of solid sorbents for separating gas mixtures. A variety of thermodynamic models have been proposed to interpolate pure component isotherms for arbitrary mixture compositions. However, when the pore structure of the material tends to segregate the adsorbed molecules into separate volumes, a segregated model gives a better description of mixture adsorption. This chapter also demonstrates that correctly estimating the saturation loading of weakly adsorbing components (e.g. N_2) allows ideal models to correctly describe the mixture behavior.

2.1 Background

Separating fluid mixtures via adsorption onto porous materials is a common process technology used in a wide variety of industrial contexts, including the separation of air, scrubbing solvent vapors from exhaust, and separation of xylene isomers.[33] The design of adsorption-based processes requires reliable thermodynamic data for the fluid-adsorbent system over a range of potential process conditions. Collecting this data for the adsorption of mixtures of gases is particularly challenging due to the complexity of the experiments and interpretation of the resulting data. This difficulty is mitigated in practice by the use of a model, such as ideal adsorbed solution theory (IAST), to interpolate mixture data from pure component data, which is simpler to collect.[34] While IAST has been shown to provide good predictions for a wide variety of fluid-adsorbent systems, there are numerous cases where it has been shown that the predictions are inaccurate.[35–42] The IAST model assumes ideal behavior of the adsorbed phase and that all components have access to the same uniform surface. This second assumption is frequently violated in practical adsorbents, and variety of approaches have been proposed to correct for the inaccuracies it introduces, which will be discussed

Material in this chapter was submitted to *AIChE J.*, Oct. 8, 2012.

in more detail below.[35,38–40,42–50] Recent efforts in synthesizing and predicting new materials have led to a plethora of potential new adsorbents, including metal-organic frameworks (MOFs), zeolitic imidazolate frameworks (ZIFs), and novel zeolites. These materials are very promising for several important gas separation applications.[51] It is possible to introduce specific sites in these materials that selectively adsorb one of the components in preference to the others giving them a heterogeneous pore space by definition. From a practical point of view, it is important to reliably predict the mixture adsorption isotherms. This requires a better understanding how the structure of these materials influences the selection of the correct model for the adsorption of mixtures.

The large number of new porous materials that have been demonstrated in recent years introduces the practical problem of evaluating such a large number of materials for a given separation. For example, Deem and co-workers have developed a database of millions of hypothetical zeolite structures.[52] Efforts by many researchers have discovered a wide array of MOFs with diverse structures and compositions.[19] The nature of MOF chemistry suggests there are potentially millions of materials when taking into account all possible combinations of metal nodes and organic linker molecules.[51,53–55] When organized into databases, there is the possibility of screening very large sets of materials simultaneously to find those best suited for a particular application.[19,50,56]

An active area of research is the development of high-throughput screening techniques to identify the most promising materials for desired gas separations. In the absence of sufficient experimental data, direct computer simulations in the grand canonical ensemble[22] can provide the data over a wide range of conditions for microporous materials like zeolites,[57] MOFs,[58] and ZIFs.[27] Both the experimental and the computational approaches focus on obtaining the pure component isotherms and rely on IAST to accurately predict the mixture isotherms.

In this work, we develop a systematic approach to incorporate these chemical inhomogeneities in the IAST. This approach is based on the simple notion that one should divide the pore space into different regions and apply IAST on each region separately. Interesting, variations of this idea have appeared several times in the literature but, as we will demonstrate in this work, it can only be used successfully with a molecular understanding of the adsorption behavior of the pure components isotherms. We illustrate with several practical examples, that such a lack of understanding of the pure component isotherms can lead to incorrect predictions.

At this point we would like to emphasize that we rely on molecular simulations to provide us with accurate data on both the pure components and mixture isotherms. From a purely conceptional point of view, there is no fundamental difference for IAST, in predicting mixture isotherms, whether these pure component data are obtained from molecular simulations or experiments. Of course, only if our simulation are representative for the experimental system our conclusions also hold for the experimental conditions. Therefore we also demonstrate that our molecular simulations give a very reasonable prediction of the known experimental isotherms for these systems.

One of the main conclusions of this work is that a reliable prediction of the mixture

isotherm requires knowledge on the number of adsorption site and which component preferentially adsorbs on which site. For many systems this can be reliably obtained from the pure component isotherms. However, in some, and usually to most interesting, cases this molecular information is lacking. We also demonstrate how molecular simulation can be used to address these questions. Given that the assumption of a uniform surface is often violated in practice, simulations provide a molecule-scale picture can be used to suggest the siting of molecules in the adsorbent's pores. These strong sites have important implications for the best model to interpolate the data. Simulations can also predict adsorption at very high pressures that may be infeasible in practice. Accurate information about the saturation loading of weakly adsorbed components may only be available at these high pressures and can help correctly parameterize the pure-component isotherms.

2.2 Adsorbed solution theories

Ideal adsorbed solution theory

Due to the importance of making reliable predictions of adsorption isotherms for fluid mixtures, many models have been proposed that attempt to predict the adsorbed phase composition and loading based on pure component data and, in some models, properties of the fluid mixture. Most practical models rely on some variant of the ideal adsorbed solution theory (IAST) of Myers and Prausnitz.[34] This approach is popular due to the fact that it relies solely upon the isotherms of the pure components in the fluid mixture and is amenable to rapid solution using numerical techniques. IAST has been used extensively to describe adsorption from multicomponent mixtures in zeolites and other adsorbents, including mixtures of alkanes, CO_2, CH_4, and N_2.[59–62] Extensions to IAST include the real adsorbed solution theory (RAST)[35] and the non-ideal adsorbed solution theory (NIAST),[43] which attempts to account for non-ideal behavior of the adsorbed phase by correlating activity coefficients from binary adsorption data or assumptions about the distribution of sites, respectively. Other approaches have attempted to deal with problems surrounding the assumption of a perfectly uniform surface. One key modification these approaches make to IAST is that the surface is assumed to be composed of independent adsorption sites, and any mixture model should be applied separately for each site. For the sake of clarity, this concept will be called segregated ideal adsorbed solution theory (SIAST) when applied in the context of this work, and the terminology of other authors will be adopted when addressing their work.

The concept of modeling adsorption as independent processes at distinct sites or volumes has been applied many times before to improve mixture adsorption predictions relative to IAST. Valenzuela et al. proposed what they termed heterogeneous ideal adsorbed solution theory (HIAST) where each component is assumed to have a distribution of adsorption sites characterized by an adsorption energy.[44] IAST is applied to each site separately based on a fitted energy difference between sites. Moon and Tien took the analysis a step further and proposed that matching the sites of different adsorbates based on a site-matching criteria

that accounts for correlation of the adsorption of different components on the same site.[38] Eiden and Schlünder applied a similar approach to the analysis of dichloromethane and benzene adsorption on activated carbons.[39,40] Calling the approach multiphase ideal adsorbed solution theory (MIAST), they assumed a pore filling mechanism and applied IAST to separate sites based on a difference in saturation volumes between components. Cerofolini and Rudznski categorized these approaches as patchwise theories, since they treat the surface of the adsorbent material as composed of a set of discrete areas or volumes where a model was applied to each individual patch, but there was no interaction between different patches.[45] One drawback of these approaches from a practical standpoint is that they require additional assumptions about the system, usually in the form of the distribution site energies. These distributions must also be parameterized, which can be difficult given the nature of the inverse problem.[46] Recent work by Ritter et al. attempted to avoid this issue by using a sum of competitive Langmuir sites approach, which they term a dual-process Langmuir (DPL) isotherm, using the parameters from fitting a dual-site Langmuir isotherm to the pure component data.[47] Their approach also permits accounting for non-ideality in the system by applying the site matching approach of Moon and Tien by simply swapping the parameters of a particular component between terms of the isotherm. Unfortunately, there is no clear method for deciding when this switch is appropriate other than comparing with experimental mixture data. A disadvantage of these approaches is that they potentially require a large quantity of detailed adsorption data at a variety of conditions that may not be easy or cheap to generate and often are specific to the material being studied.

In more recent work, several authors have attempted to use molecular simulations to evaluate the usefulness of IAST and similar approaches for predicting mixture properties in zeolites and MOFs. Cessford et al. have provided a comprehensive overview of the topic in their recent paper,[48] and we will only address a few highlights here. Krishna and co-workers have evaluated the use of IAST to predict mixtures of alkanes in the zeolite MFI[63] and CO_2:CH_4 mixtures in cage-type zeolites.[42] In this latter paper, the authors observed that IAST failed to give a good description of the mixture at higher pressures, and ascribed this to a segregation of the two components due to preferential adsorption at either the center of the cages or the windows between cages. Jee and Sholl suggested that using a segregated model for CO_2:CH_4 adsorption in zeolite DDR improves predicted isotherms relative to IAST, but is still inaccurate at high total fugacity.[49] Van Heest et al. performed an extensive screening of MOFs for separating noble gas mixtures, and noted that accounting for regions that would be inaccessible to one component of the mixture was important for correctly predicting adsorption selectivity.[50] A key aspect of these studies is that they were able to correlate specific structural features of the adsorbents to the inaccuracy of IAST.

Segregated ideal adsorbed solution theory

One assumption of IAST that can be easily violated is the assumption of an equivalent surface available to all components. Strictly speaking, for microporous adsorbents like zeolites, the concept of spreading pressure is not applicable because there is no well defined

surface.[43,64] However, the idea of accessible surface area or pore volume is still a useful concept for diagnosing failures of IAST. If the components of the mixture can access different parts of the material, one component may be able to diffuse into cavities not accessible to other components and is thus no longer competing with the other components for the same adsorption sites. In recent work on the screening of zeolites for the separation of CO_2 and N_2, we discovered a class of materials that had particularly strong adsorption sites for CO_2.[56] These were often small pockets that could accommodate a single CO_2 molecule, and the arrangement of the framework atoms around the pocket provides a site with a particularly favorable interaction energy for the molecule. While N_2 is not formally excluded from these pockets, they are more likely to be occupied by CO_2 when the two gases are adsorbing competitively. Materials of this sort typically exhibit an isotherm with a plateau or step at intermediate loading that can be accurately correlated with the dual-site Langmuir isotherm equation. The loading at the plateau corresponds to the density of strong adsorption sites in the unit cell.

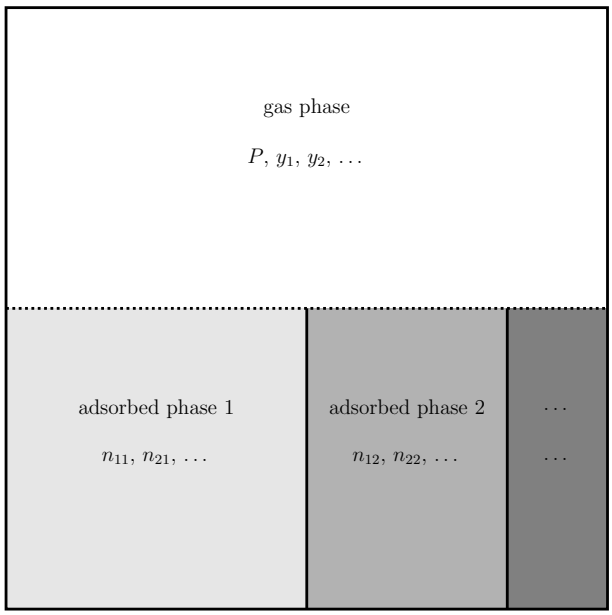

Figure 2.1: Schematic diagram of the phases in the segregated IAST model. A gas phase (white) is in equilibrium with M independent adsorbed phases (shades of gray). The whole system is at a constant temperature. The gas phase is characterized by a total pressure P and its composition, usually expressed as the mole fraction of all components y_i. Each adsorbed j phase is characterized by the loading of each component i, n_{ij} in equilibrium with the gas phase. Each adsorbed phase is in equilibrium separately with the gas phase.

To more accurately describe the total loading of a system that may have spatially distinct adsorption sites, we propose that applying IAST to distinct sites can provide more

accurate predictions in many cases. Instead of considering the available pore volume to be one continuous space, the volume may be subdivided into natural regions where separate competition processes take place. For materials where it is possible to identify segregated sites, it is possible to model the mixture adsorption as the sum of separate competitions, which in turn may be modeled using IAST. Figure 2.1 shows how this might be extended to an arbitrary number of adsorbed phases. Equation 2.1 relates the isotherm of component i on site j to the surface potential.

$$\psi_{ij} = \int_0^{f_{ij}^{\circ}} n_{ij}\left(f\right) dlnf \tag{2.1}$$

In Equation 2.1, the surface potential for adsorption of component i at site j is related to an adsorption isotherm representing only site j. In this work we will assume that each site can be described by a single-site Langmuir isotherm,

$$n_{ij}\left(f\right) = \frac{m_{ij} b_{ij} f}{1 + b_{ij} f} \tag{2.2}$$

giving the following expression for the surface potential

$$\psi_{ij}\left(f_{ij}^{\circ}\right) = m_{ij} \log\left(1 + b_{ij} f_{ij}^{\circ}\right) \tag{2.3}$$

where m_{ij} and b_{ij} are the saturation loading and Langmuir constant for adsorption, respectively, of component i at site j. The condition for equilibrium may be expressed as 2.4 for competitive adsorption between N components at site j.

$$\psi_{1j} = \psi_{2j} = ... = \psi_{Nj} \tag{2.4}$$

Since we treat the adsorbed phase as composed of independent phases, each is related to the gas phase independently.

$$f y_i = x_{ij} f_{ij}^{\circ}\left(\psi_{ij}\right) \tag{2.5}$$

There is an independent mass balance on each phase.

$$\sum_{i=1}^{N} x_{ij} = 1 \tag{2.6}$$

The total loading in phase j is given by

$$n_{tj} = \left[\sum_{i=1}^{N} \frac{x_{ij}}{n_{ij}\left(P_{ij}^{\circ}\right)}\right]^{-1} \tag{2.7}$$

and loading of component i in phase j is given by

$$n_{ij} = x_{ij} n_{tj} \tag{2.8}$$

The total loading of component i is simply the sum of the loadings in the individual phases.

$$n_i = \sum_{j=1}^{M} n_{ij} \tag{2.9}$$

While this method is general, experimental isotherms may not cover a large enough range of pressures to accurately determine the site saturation loadings for all components at each site.

To compare traditional IAST with the current approach, the dual-site Langmuir isotherm model was fitted to the pure component isotherms using non-linear least-squares regression.

$$n_i\left(f\right) = \frac{m_{i1} b_{i1} f}{1 + b_{i1} f} + \frac{m_{i2} b_{i2} f}{1 + b_{i2} f} \tag{2.10}$$

For materials with strongly segregated sites for adsorption, the saturation at the first site was fixed to the same value for both CO_2 and N_2, reflecting the fact that only one molecule of any component can occupy one of these sites at a given time.

2.3 Methods

To investigate different models of adsorption, GCMC simulations were used to generate pure-component and mixture isotherms for mixtures of CO_2 and N_2 in different zeolites and CO_2 and C_3H_8 in the zeolite MOR. These were treated as the reference data that allows us to compare the predictions of different models. Simulations in the grand canonical ensemble involve specifying the temperature and volume of an adsorbent system and the chemical potentials of all the adsorbing components.[22] The simulation box was defined by a tiling of one or more crystallographic unit cells of a given material. All framework atoms were held fixed. Trial configurations were generated by attempting to move, rotate, re-insert, or remove an existing molecule or adding a new molecule to the simulation box. The energy of all interactions was described using the 12-6 Lennard-Jones potential plus an electrostatic term. The Ewald summation technique was used for the electrostatic interactions. All short-range interactions were cut off and shifted to zero at 12.0 Å. Interaction parameters and partial atomic charges were taken from different sources, depending on the system under study. CO_2 and N_2 adsorption in siliceous zeolites were modeled using the parameters of García-Pérez et al.[65] C_3H_8 adsorption in MOR was parameterized using the force field of Dubbeldam et al.[24]

For simulations in aluminosilicate zeolites NaX (NaFAU), CO_2 and sodium interaction parameters were taken from García-Sánchez et al.[66] N_2 interaction parameters in these materials are reported in the Table 2.1. Lennard-Jones epsilon parameters for N_2 were scaled from the parameters of the interaction between the carbon of CO_2 and zeolite sodium and oxygen atoms taken from the force field of García-Sánchez et al.[66] The scaling was performed by taking the ratio of polarizabilities for atomic carbon and nitrogen. N_2-N_2interactions and

partial atomic charges were taken from the force field of García-Pérez et al.[65] Sigmas were computed using Lorenz-Berthelot mixing rules with Na^+ and zeolite oxygen parameters from Calero et al.[67] and Talu and Myers.[68] The resulting predictions of this model compare well with recent experimental data. Figure 2.2 shows that these molecular simulations give a reasonable prediction of the pure component isotherms, which gives us some confidence that our simulation data closely mimic the experimental systems. Hence, our conclusions with respect to the application of IAST to the simulation data also hold for the experimental system.

Table 2.1: Lennard-Jones parameters for sodium and zeolite oxygen interactions with the atoms of N_2 molecules.

Interaction	σ Å	ϵ/k_B K
$O_{zeolite}$-N	3.062	28.23
Na^+-N	2.74	291.6

2.4 Results and discussion

We have broken down the analysis into a three separate cases based on the degree of segregation between adsorption sites and the relative preference of each adsorbing component for each of the adsorption sites. In one extreme case of segregation, the adsorption sites may be spatially separated from one another and diffusion between sites requiring crossing a barrier. Each of these sites can represent a different free energy for each component, and components will occupy the sites in the order that represents the lowest free energy for the component. In this work, we have considered materials with two distinct adsorption sites, and we distinguish whether a given mixture exhibits a normal site preference, that is, components occupy sites in the same order, or reverse site preference, where one component occupies sites in the reverse order that the other component does. This parallels the site correlation concept used by Moon and Tien[38] and Ritter et al.[47] We also consider the case where sites are not isolated from one another and evaluate the use of competitive isotherm models.

Materials with isolated sites, normal site preference

GCMC simulations were performed for pure CO_2 and pure N_2 in hypothetical zeolites PCOD8286959 and PCOD8200029 from Deem's database of hypothetical materials[52] at 300 K. These pure component isotherms are shown in Figure 2.3 A and Figure 2.5 A, respectively. The isotherms were simulated from very low fugacity (on the order of 10 Pa) up to 10^9 Pa fugacity. The very high fugacities are required to ensure that the plateaus in the isotherm are accurately represented. In the case of the more weakly adsorbing N_2, fugacities above 10^7 Pa and 10^6 Pa for PCOD8286959 and PCOD8200029a, respectively, were required for

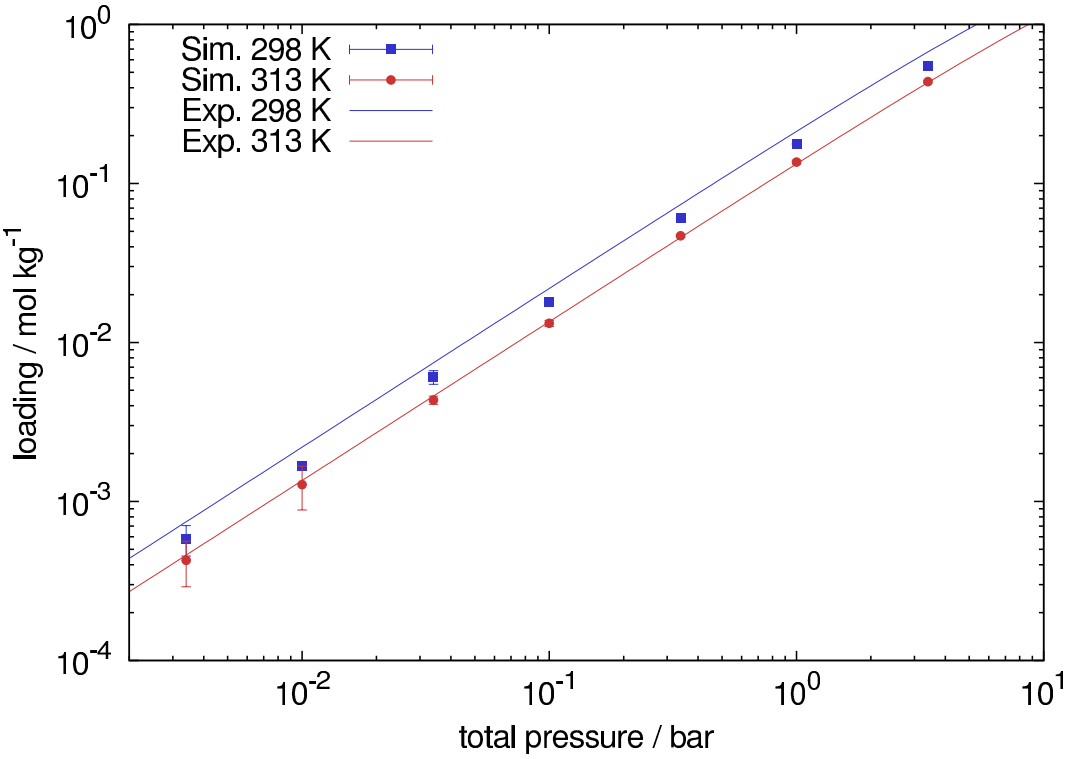

Figure 2.2: Comparison of GCMC-predicted and experimental isotherms for N_2 adsorption in NaX using the force field in Table 2.1. Experimental data are the single-site Langmuir fits reported in Bae et al.[69]

the isotherm to approach a saturation loading. All pure component isotherms were fitted using the dual-site Langmuir isotherm (Eqn. 2.10) with the constraint that the saturation loading of the first adsorption site (m_{i1}) was fixed to be identical for both CO_2 and N_2 (fitted parameters can be found in Appendix A). Previous work[56] has indicated that adsorption in these materials occurs first at small localized pockets in the material that can accommodate only a single molecule. Figures 2.4 and 2.6 show accumulated snapshots of CO_2 and N_2 locations in PCOD8286959 and PCOD8200029a, respectively, taken from the GCMC simulations of the mixture at 10^9 Pa. In PCOD8286959 (Fig. 2.4), large main channels (purple circle) run parallel to the c crystal axis, and small pockets (orange circle) connect between channels in the b direction. The density of these sites is set by the crystal structure of the material and hence should be identical for both components. Although N_2 does not exhibit a pronounced step in the isotherm because it does not have as strong a preference for this site as CO_2does, this constraint is required to ensure the correct description of the total loading of each site in the mixture model. In PCOD8286959 (Fig. 2.4), the molecules can adsorb in two separate pore systems, one running parallel the c crystal axis (orange circle and arrow) and the other running parallel to the b axis (purple circle and arrow). The sizes of these two

channels are slightly different, with CO_2 preferring to adsorb in the channels parallel to the b axis, as shown by the predominance of blue points in Figure 2.4 B.

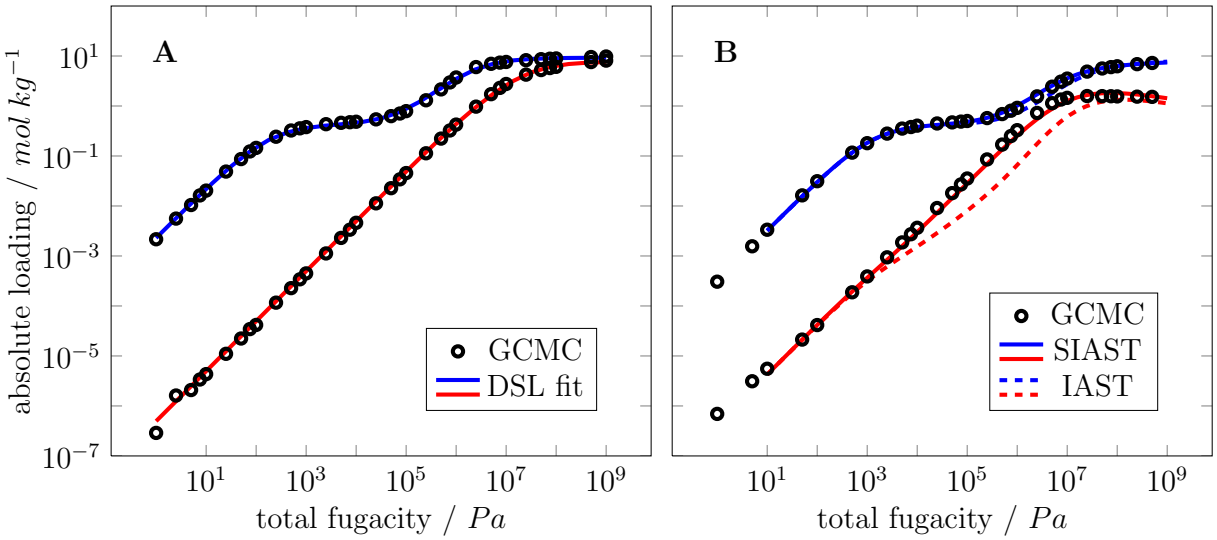

Figure 2.3: Comparison of isotherms computed via GCMC and different mixture adsorption models in pure silica PCOD8286959 at 300 K. (A) Pure component isotherms of CO_2 (blue) and N_2 (red) with lines indicating the fit of the dual-site Langmuir model (Eqn. 2.10). (B) Mixture adsorption isotherms for a 14% CO_2 (blue), 86% N_2 mixture. Symbols indicate GCMC results, solid lines represent the segregated IAST model, and dashed lines represents the traditional IAST model.

Figures 2.3 B and 2.5 B show adsorption isotherms for a 14% CO_2, 86% N_2 mixture at 300 K predicted using GCMC, the segregated IAST model, and the original IAST model in PCOD8286959 and PCOD8200029a, respectively. The original IAST data was generated by integrating Equation 2.1 directly with Equation 2.10 for the two components. For both materials, the models both agree with the GCMC data at very low fugacity. At these low fugacities, adsorption is occurring in the linear or Henry's law regime of the isotherm. Each component is in effect adsorbing independently and is completely described by its Henry coefficient. Both the segregated and traditional IAST model agree up to fugacities commensurate with the first saturation loading in the pure CO_2 isotherm. Above these fugacities, the N_2 loading predicted by traditional IAST is lower than the GCMC results. In the case of PCOD8286959 (Fig. 2.3 B), the IAST-predicted N_2 loading matches the GCMC results at fugacities above 10^7 Pa, whereas in PCOD8200029a, the IAST-predicted N_2 loading is consistently 10 times lower than the GCMC isotherm. For both of these materials, the segregated IAST model provides excellent agreement with the GCMC results at all fugacities.

The effect of using the traditional IAST model is that the step in the CO_2 isotherm induces an effective step in the N_2 isotherm when using IAST because it imposes a competitive

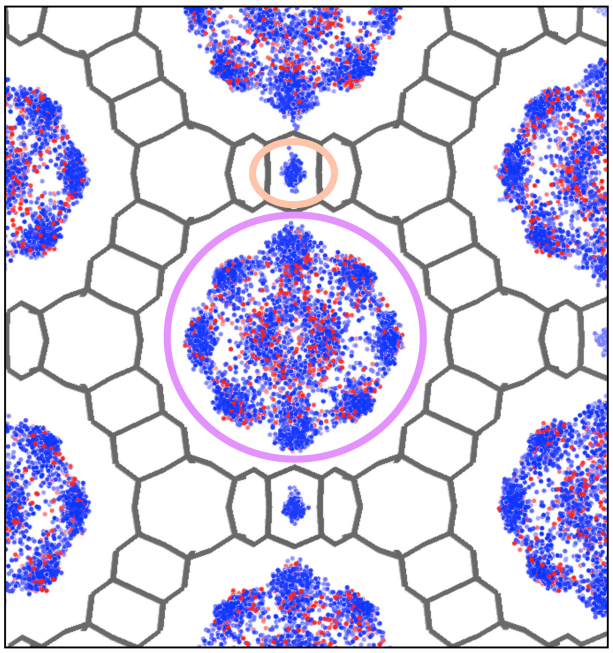

Figure 2.4: Snapshots of CO_2 (blue) and N_2 (red) center-of-mass configurations in zeolite PCOD8286959 during simulation at 10^9 Pa fugacity and 300 K. Framework silicon and oxygen atoms are drawn in dark gray, and the centers-of-mass were collected from 10a,000 samples during the GCMC simulation. The purple and orange circles indicate the main channels and the small pockets of the material, respectively. Due to the affinity of $CO_2$for the small pocket, N_2 is effectively excluded and only adsorbs in the main channel.

adsorption process between CO_2 adsorbing at the stronger adsorption sites and N_2 adsorbing at the weaker adsorption sites. The adsorption of N_2 at the weaker sites in the framework can occur simultaneously and independently of adsorption at the stronger sites due to the fact that there is likely a barrier between adsorption at these distinct sites. The fact that CO_2 is more likely to adsorb at the stronger sites first frees up the rest of the volume of the material where it would otherwise adsorb to provide adsorption sites for N_2. We also note that the relative saturation loadings of the two adsorption sites does not appear to matter. If we compare the fitted isotherm parameters the case of PCOD8286959 (Fig. 2.3), the first saturation loading is 0.4229 mol kg^{-1}, compared to 8.811 mol kg^{-1} for the second saturation loading of CO_2. The same values for the two sites in PCOD8200029 (Fig. 2.5) are 1.510 mol kg^{-1} and 0.7354 mol kg^{-1}, respectively. The first site accounts for 4.6% of the total saturation in PCOD8286959 but over 67% of the total saturation loading in PCOD8200029. Even though one site in the material may provide the majority of all adsorption sites, it is important to partition them correctly, especially to predict mixture adsorption at high fugacity where both sites will likely be occupied to some extent.

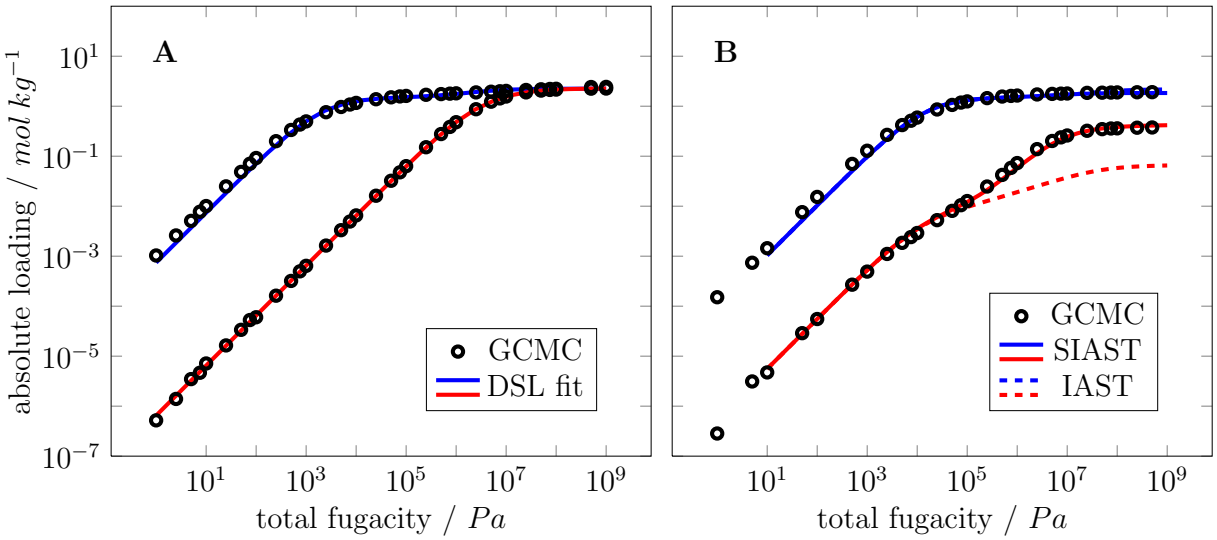

Figure 2.5: Comparison of isotherms computed via GCMC and different mixture adsorption models in pure silica PCOD8200029 at 300 K. (A) Pure component isotherms of CO_2 (blue) and N_2 (red) with lines indicating the fit of the dual-site Langmuir model (Eqn. 2.10). (B) Mixture adsorption isotherms for a 14% CO_2 (blue), 86% N_2 mixture. Symbols indicate GCMC results, solid lines represent the segregated IAST model, and dashed lines represents the traditional IAST model.

Materials with isolated sites, reverse site preference

One set of data that has been used to evaluate different mixture adsorption models was the adsorption of CO_2:C_3H_8 on H-MOR. Valenzuela et al., Moon and Tien, and Ritter et al. all applied their approaches and showed that different segregated models improved predictions for the system relative to IAST.[38,44,47] We computed isotherms for pure CO_2, pure C_3H_8 (Fig. 2.7 A) and a 50:50 CO_2:C_3H_8 mixture (Fig. 2.7 B) adsorbing in the pure-silica form of MOR at 300 K. The MOR topology has well-known side pockets along the main pores of the material, and this is reflected by the step in the isotherms for both components. Figure 2.8 shows center-of-mass configurations of CO_2 and C_3H_8 recorded during GCMC simulations at low (10^3 Pa) and high (10^9 Pa) fugacity of both pure components and the mixture described above. The purple circle indicates the main channels of the material, running parallel to the c crystal axis and the orange circles indicate the side pockets along these channels. As can be seen in the pure CO_2 snapshots, CO_2 is most likely to be found in the side pockets at low fugacity, then as those are saturated, stars to fill the main channels. The reverse is true for C_3H_8. We note that the second saturation for C_3H_8 does not appear until the fugacity goes above 10^8 Pa, whereas CO_2 begins to saturate its second site below 10^6 Pa fugacity. Since these components have opposite preferences, at low fugacity, C_3H_8 occupies the main channels while CO_2 resides in the side pockets. At high fugacity, however, CO_2 has saturated

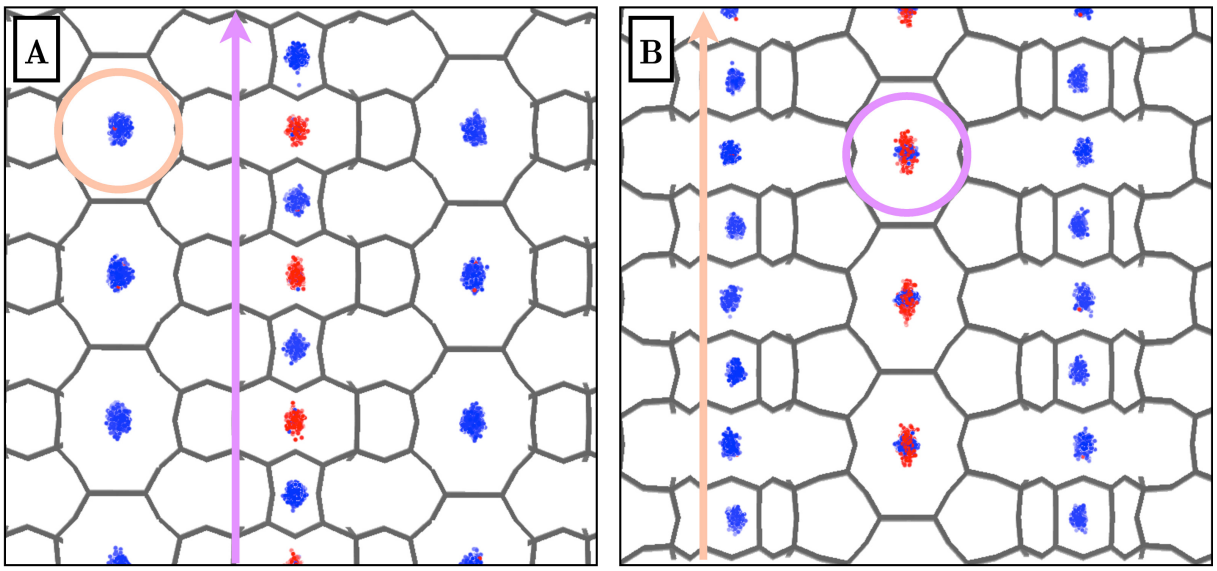

Figure 2.6: Snapshots of CO_2 (blue) and N_2 (red) center-of-mass configurations in zeolite PCOD8200029 during simulation at 10^9 fugacity and 300 K. Framework silicon and oxygen atoms are drawn in dark gray, and the centers-of-mass were collected from 10a,000 samples during the GCMC simulation. The pores of the material consist of two orthogonal pore systems, indicated by the purple and orange arrows and circles. (A) and (B) show the views down the *c* and *b* crystallographic axes, respectively. The pores are small enough in the channel indicated by orange that CO_2 prefers to site there and tends to exclude N_2. Both components are accommodated in the slightly larger channels indicated by purple.

the side pockets and competes for the main channels with C_3H_8, which can be seen by the relatively few red points in the mixture snapshots for this condition.

Figure 2.7 B compares the predictions of IAST, segregated IAST, and the DPL model with the results of the GCMC simulations. The dual-site Langmuir parameters for both pure components were fit without restriction. Although we did not constrain them as in the previous case, we observed that the first saturation loading for CO_2 (4.165 mol kg^{-1}) was comparable to the second saturation loading for C_3H_8 (4.993 mol kg^{-1}). As shown by Ritter et al., reversing the sense of the two sites in the isotherms of CO_2 and C_3H_8 provided the best predictions of experimental mixture compositions on H-HOR.[47] In our application of the segregated IAST and DPL models, we also made this switch so that the first site in the CO_2 isotherm competes with the second site in the C_3H_8 isotherm and vice versa. Traditional IAST does not provide for this reversal since the entire isotherm is integrated simultaneously and provides the poorest description of the data. SIAST and the DPL model provide good agreement with the GCMC results at low fugacity. At high fugacity, the DPL model predicts a constant composition after the fugacity increases beyond 10^6 Pa. This is expected for competitive isotherm models since the limit for this form of isotherm as

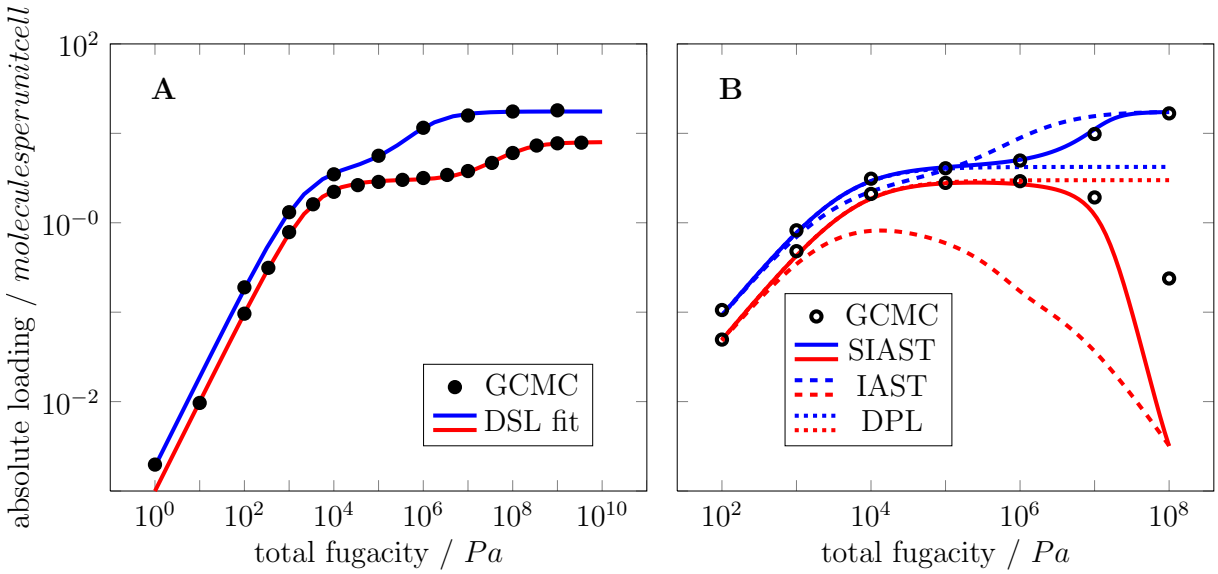

Figure 2.7: Comparison of isotherms computed via GCMC and different mixture adsorption models in pure silica MOR at 300 K. (A) Pure component isotherms of CO_2 (blue) and C_3H_8 (red) with lines indicating the fit of the dual-site Langmuir model (Eqn. 2.10). (B) Mixture adsorption isotherms for a 50% CO_2 (blue), 50% C_3H_8 mixture. Symbols indicate GCMC results, solid lines represent the segregated IAST model, dashed lines represents the traditional IAST model, and densely dotted lines are predictions of the dual-process Langmuir model of Ritter et al.[47]

fugacity or pressure approaches infinity is simply the saturation loading of the component. The GCMC simulations predict that the loading of C_3H_8 will eventually decrease. The replacement of C_3H_8 by CO_2 in the pores should be expected at very high fugacity due to the entropic effect of smaller molecule CO_2 filling the available volume more effectively than C_3H_8. The segregated IAST model provides a good fit to the GCMC results for CO_2 over the entire fugacity range, and C_3H_8 is well-described up to about 10^7 Pa total fugacity. Above this fugacity, the predicted C_3H_8 loading decreases more rapidly than observed via GCMC. This may be due to other features in the isotherm that would be observed by simulating the pure components at higher fugacity then we did and would require an additional site in the isotherm to describe.

The segregated IAST and DPL model required that the second site in the C_3H_8 isotherm was matched with the first site of the CO_2 isotherm to provide accurate predictions. This is due to the fact that CO_2 readily enters the side pockets along the channels of MOR, while C_3H_8 first adsorbs in the main channels and enters the side pockets at high pressure. This behavior can readily be seen in snapshots of the molecular configurations recorded during the GCMC simulations. Since only one molecule can occupy these side pockets at a time, it

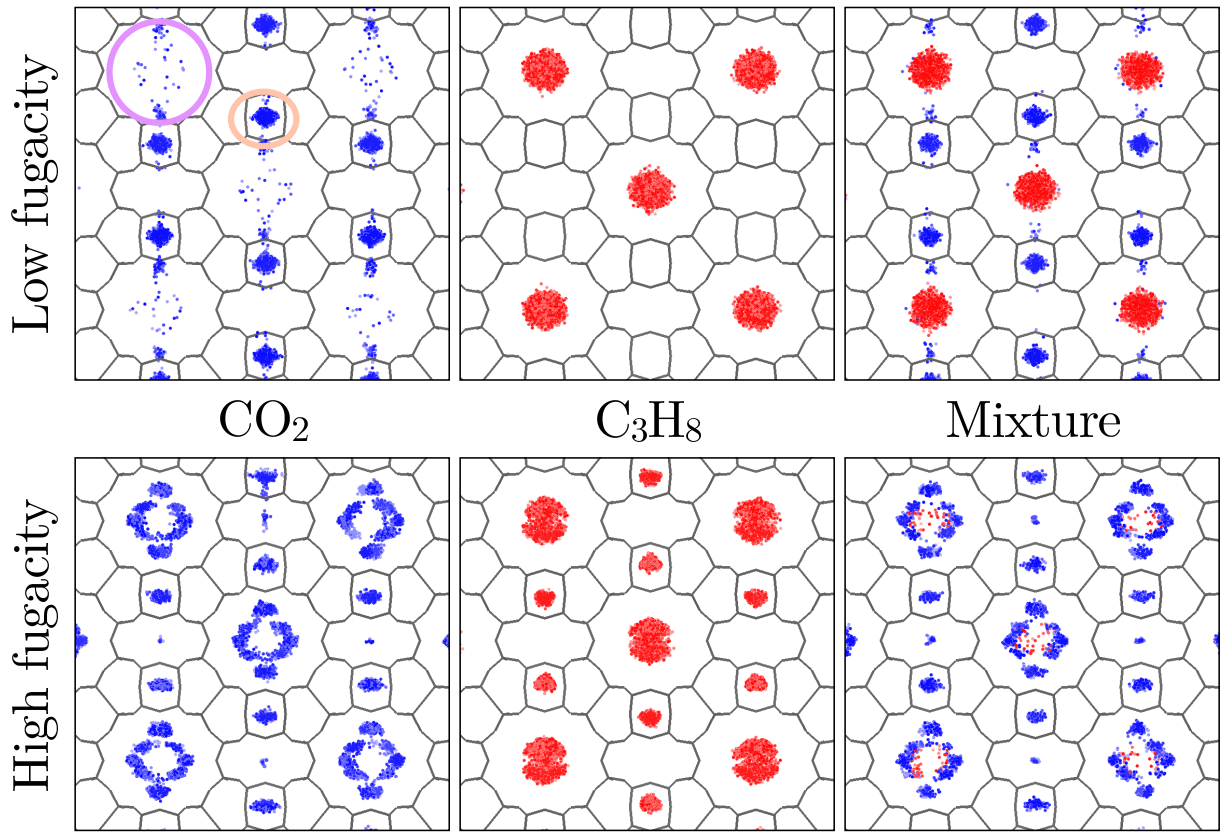

Figure 2.8: Snapshots of CO_2 (blue) and C_3H_8 (red) center-of-mass configurations in zeolite MOR during simulation at low (10^3 Pa) and high (10^9 Pa) fugacity and 300 K. Framework silicon and oxygen atoms are indicated in gray and all views look parallel to the *c* crystal axis. The centers-of-mass were collected from 10a,000 samples during the GCMC simulations. The purple and orange circles in the top left figure show the main channels and side pockets of the material, respectively. While both components can occupy either site, CO_2 tends to adsorb in the pockets first, while C_3H_8 only enters the pockets at high fugacity.

is appropriate that the loading of the first site in the CO_2 isotherm and second site in the C_3H_8 isotherm are comparable. The non-ideal nature of this system arose solely from this difference in siting behavior and is not a necessarily the result of non-ideality in the CO_2:C_3H_8 fluid mixture. Unfortunately, the matching of the correct spatial placement of the sites is not easy to ascertain from simply fitting the pure component isotherms. The complementary site-matching or perfect negative correlation described by Moon and Tien and Ritter et al. , respectively, accounts for this ordering, but requires either additional parameterization or evaluation against experimental data to work. Information about the siting of molecules is a direct result of GCMC simulations and can provide a direct method for determining the correct pairing of sites when applying SIAST with no additional assumptions.

Materials where sites are not isolated

Another important class of materials for gas separations are aluminosilicate zeolites. The presence of aluminum atoms in the framework creates a charge imbalance that is compensated by the presence of cations in the pores of the material. These cations can be exchanged by washing the materials with solutions of metal salts, and a mixture of different cations can be used to modify the adsorption properties of the materials for a specific purpose. Recent studies on the common type X and type A zeolites suggest that they may be selective adsorbents for separating mixtures of CO_2 and N_2.[69–71] They typically exhibit a very large selectivity for CO_2 over N_2 due to the stronger interactions with the larger quadrupole moment of CO_2. We simulated adsorption of CO_2, N_2, and a 15%:85% CO_2:N_2 mixture in zeolite 13X (NaFAU). This material has a Si:Al ratio of approximately 1.24:1. Adsorption of these gases occurs in the supercages of the material, which are connected by 7.4 Å windows. The relatively large distances in these materials suggests that there are not volumes where an adsorbed molecule is segregated from the other pores space and can exclude other molecules. Figure 2.9 A shows the adsorption isotherms for the pure gases at 313 K.

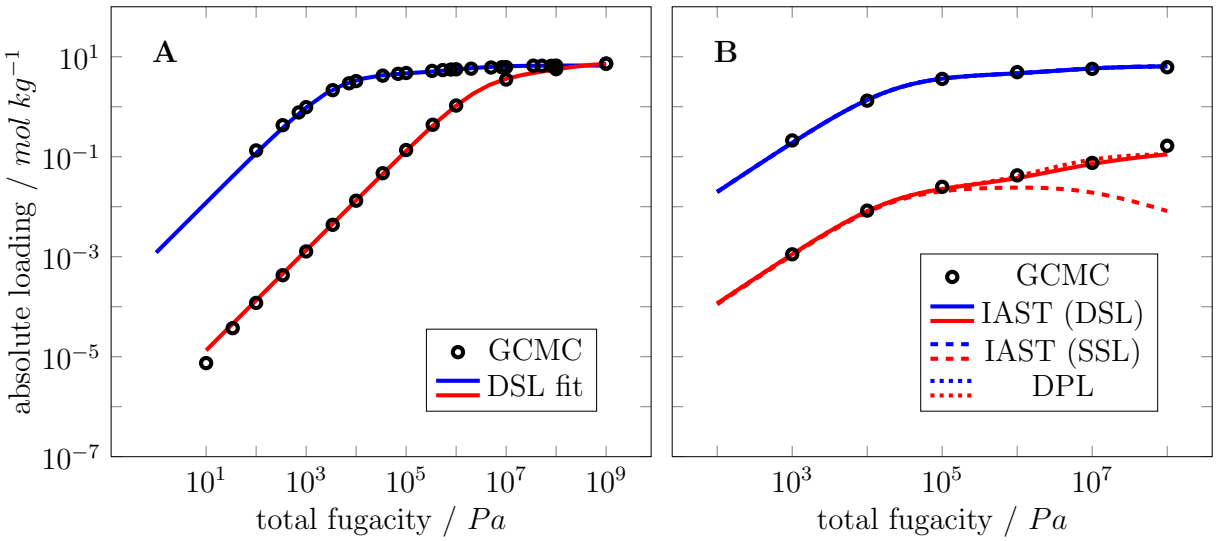

Figure 2.9: Comparison of isotherms computed via GCMC and different mixture adsorption models in aluminosilicate NaFAU (13X) at 300 K. (A) Pure component isotherms of CO_2 (blue) and N_2 (red) with lines indicating the fit of the dual-site Langmuir model (Eqn. 2.10). (B) Mixture adsorption isotherms for a 14% CO_2 (blue), 86% N_2 mixture. Symbols indicate GCMC results, solid lines represent the segregated IAST model, and the dashed line represents the traditional IAST model.

The CO_2 isotherm exhibits two-site behavior that can be well correlated using the DSL isotherm. Due to the weak adsorption of N_2 at ambient conditions, it is difficult to estimate the saturation loading from typically experimental isotherms. As seen in Figure 2.9 A, it

would take on the order of 10^8 Pa fugacity to observe saturation loading of N_2. In the absence of the required saturation loading, it is often assumed that the saturation loading for one component eventually takes the same value as the other component and a single-site isotherm. This assumption, in and of itself, is not a bad approximation for this system. At the highest fugacity simulated (10^9 Pa), the loading of CO_2 and N_2 agree well (Fig. 2.9 A). However, it is possible to fit a dual-site model to the N_2 data with a high level of confidence. Figure 2.9 B compares the application of traditional IAST using a dual-site model for CO_2 and either a single-site or dual-site model for N_2. We have also included the dual process model of Ritter et al. to demonstrate the utility of using competitive models for describing this system.

Figure 2.9 B shows that the application of IAST with a dual-site model for both components improves the prediction of mixture isotherms for N_2 in NaX compared to using a single-site isotherm for N_2. The CO_2 isotherm is not strongly influenced by the choice of isotherm model for N_2, reflecting the fact that the stronger adsorption of CO_2, reflected by its larger adsorption constants, means that it will always be the preferred molecule to adsorb at a given site. Even though it is the more likely component to adsorb at either site, CO_2 will tend occupy the strongest site first, since this site represents the lowest free energy for the molecule. It is important that the isotherm for N_2 also reflects this choice of adsorption site, even if the preference between the sites is not as strong as the other component. When CO_2 adsorbs at its lowest free energy site, it will tend to compete with N_2 to a lesser extent at the higher free energy site, and consequently the N_2 adsorbs to a greater extent than would otherwise be expected. If a single-site isotherm is used to describe N_2 adsorption, the predicted mixture contain less nitrogen because CO_2 will always be preferred at a given adsorption site and N_2 does not have the option at adsorbing at another site that represents a relatively high free energy for CO_2. In contrast to the materials considered in the sections above, there is not a spatial segregation of adsorption sites, and both the traditional IAST and the DPL model provide a similar description of adsorption in these materials. Correct modeling of the mixture adsorption requires that each pure component is represented by a model that represents all possible sites where it may adsorb.

2.5 Summary

We have evaluated the prediction of adsorption isotherms for mixtures of gases in nanoporous materials using IAST on segregated adsorbed phases. This approach can provide a better description of adsorption in these materials, especially when there are distinct adsorption sites with different saturation behaviors. We think simplicity of this model makes it sufficiently cheap to calculate for use in the screening of databases of materials for separations or for use in other computational modeling that would benefit from a computationally cheap description of mixture adsorption. High pressure isotherm data is important to accurately fit saturation loadings. Any model of a pure component used to predict mixture adsorption should describe any multiple-site behavior, even if the preference for different sites is

weak. This is especially important when interpreting isotherms where good estimates of the saturation loadings of all components are not available.

Chapter 3

In silico screening of carbon capture materials

Molecular simulations are a powerful tool for evaluating materials based on their adsorption properties. That being said, an adsorption isotherm is an insufficient criteria for selecting the best material for a given separation. The work detailed in this chapter discusses the use of an equilibrium process model to estimate the minimum energy that would be diverted from a power plant's output to separate CO2 with an adsorption process. Since each material can have its own optimal operating conditions, the model optimizes over a range of possible process conditions. Rapid molecular simulations provide the data to run the model, and we were able to identify many materials with a lower energy penalty than the standard amine process.

3.1 Background

One can use simple thermodynamics to estimate the minimum energy required to separate CO_2 from flue gases (typically, 70-75% N_2 13% CO_2 5-7% H2O, 3% O2 at 40C and 1 atm). If we capture 90% of the CO_2 from a coal-fired power plant with the separation performed at 40C, the minimum energy required is of the order of 4-5% of the energy produced by the power plant.[16] Near-term capture technologies are projected to use five times the thermodynamic limit.[16] This suggests that capture processes that use less energy may be feasible. The technology for CO_2 capture considered near-term for power plants was developed as far back as the 1930s.[12,13] This technology uses aqueous solutions of amines that react with CO_2 to form carbamates and are therefore highly selective in capturing CO_2Ȯne drawback of these amine solutions is that they contain 70% water by weight, and the regeneration cycle involves heating and evaporating large volumes of water, making the process energy intensive. Alternative separation processes that use other solvents, solid adsorbents, or

Material in this chapter is based on Lin et al., *Nat. Mater.*, *11*, **2012**, 633-641 (doi:10.1038/NMAT3336).

membranes have the potential to require less energy.[16] One of the main challenges here is that many properties of CO_2 and N_2 are similar, and hence success of these approaches relies on the development of novel materials sensitive to these small differences.

For adsorbent-based gas separations, it is important to have adsorbents with a large internal surface;[72] examples of such material include zeolites, metal-organic frameworks (MOFs), and zeolitic imidazolate frameworks (ZIFs).[30,32,53,73] The number of possible structures of these materials is very large: hundreds of thousands of possible zeolites with different pore topologies exist in the zeolite database,[52] and a nearly infinite number of different types of MOFs can be created by changing the type of the metal and the organic linker. In practical terms, synthesizing and testing all these structures for CO_2 separation would be an impossible task. Therefore, we have developed a viable computational strategy to characterize large databases of carbon capture materials and identify optimal materials for CO_2 separation.

Several articles on screening for optimal separation materials have been published.[74–76] These articles consider a limited set of 10-20 different materials, which is insufficient to characterize the hundreds of thousands of different possible topologies.[52] In addition, these studies often focus on a single material property, such as selectivity or residence time, at a specific condition. However, optimizing the residence time[75] or uptake[76] in the adsorption step, for example, ignores that a material effective at adsorbing CO_2 might be difficult to regenerate. More importantly, these studies do not consider that different materials perform optimally at different conditions. In this work, we take another approach. For each material we determine the optimal process conditions by minimizing the electric load imposed on a power plant by a temperature-pressure swing capture process using that material followed by compression. This minimum load, which we call parasitic energy, is introduced as a metric to compare different materials.

Separation of gases using nanoporous materials exploits the fact that at flue gas conditions CO_2 selectively adsorbs in the pores of these materials. By increasing the temperature, decreasing the pressure, or a combination of both, nearly pure CO_2 can be recovered. Figure 3.1 illustrates such a temperature-pressure swing separation process. Regardless of the regeneration method, the parasitic energy of a CCS process can be readily modeled if equilibrium adsorption and desorption are assumed. While there are many possible process configurations, they all rely on the difference between adsorption and desorption conditions to capture CO_2The processes vary primarily in their method of gas-solid contacting and heat transfer, though neither of those factors affects performance under equilibrium assumptions. The energy required for this process has three main components: (1) energy to heat the material, (2) energy to supply the heat of desorption (equal to the heat of adsorption), and (3) energy required to pressurize CO_2 to 150 bar, which is a standard requirement for transport and storage.[77] For a specific material and a fixed adsorption condition, we vary the desorption conditions and calculate the CO_2 and N_2 loading differential between the adsorption and desorption conditions to compute the quantity and purity of CO_2 captured. The thermal energy requirement (Q) of the process per unit mass of CO_2 captured (Δq_{CO_2}) is the sum of the sensible energy needed to heat the bed to the desorption temperature and the energy

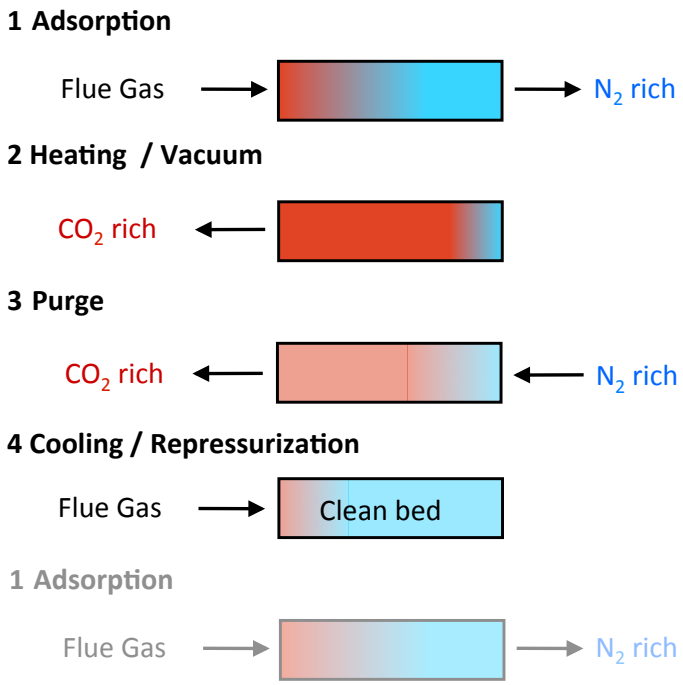

Figure 3.1: Hybrid pressure and temperature swing adsorption. In the adsorption step (1) the flue gas is brought into contact with the solid adsorbent. The material selectively adsorbs CO_2 and (nearly) pure N_2 leaves the adsorber. When the adsorber is saturated, it is regenerated (2) by heating the system and/or applying a vacuum. The purge (3) and cooling or repressurization step (4) brings the system in its original state (1). The amount of CO_2 that is removed from the flue gas in a single cycle defines the working capacity of a material. The regenerated CO_2 is subsequently pressurized to 150 bar for geological storage.

needed to supply the heat of adsorption.

$$Q = \frac{C_p m_{sorbent} \left(T_{final} - T_{flue}\right) + \left(\Delta q_{CO_2} \Delta h_{CO_2} + \Delta q_{N_2} \Delta h_{N_2}\right)}{\Delta q_{CO_2}} \tag{3.1}$$

where C_p is the specific heat capacity of the adsorbent, $m_{sorbent}$ is the mass of the adsorbent, $T_{final} - T_{flue}$ is the temperature differential between the adsorption and desorption conditions, Δq_i is the difference in loading and Δh_i is the heat of adsorption for each species. The loading at specific conditions is calculated using competitive adsorption isotherms, and the

heats of adsorption are obtained directly from the molecular simulations. In a power plant, this thermal energy is supplied by diverting steam from the power cycle. Diverting steam effectively imposes a parasitic load on the power plant, which we compute as the product of the thermal energy requirement (Q), the Carnot efficiency (η) of the extracted steam, and the typical efficiency of a turbine (75%).[14] The compressor work, W_{comp}, is obtained from a multi-stage intercooled compressor model with real gas properties using NIST REFPROP[78] for fluid property data. We assume a staged compression, intercooled to 40C, with a maximum pressure ratio of 2.5 and an isentropic efficiency of 85% below the supercritical point and 90% above it. Finally, the parasitic energy, E_{eq}, imposed on the power plant of the CCS process, is given by:

$$E_{eq} = 0.75\eta_{T_{final}}Q + W_{comp} \tag{3.2}$$

For each material we find the optimal process conditions by minimizing this parasitic energy. Using a similar analysis, a state-of-the-art amine capture process would have a parasitic energy of 1060 kJ/kg CO_2Å more rigorous engineering analysis of an amine process retrofitted to a coal-fired power plant which includes pressure drop through equipment, losses in heat exchangers, and other energy losses, shows a parasitic load of 1327 kJ/kg CO_2 about 25% higher.[77] Therefore, we seek materials that exhibit a parasitic energy significantly lower than 1060 kJ/kg CO_2 with the expectation that, similar to the amine process, a more detailed analysis of a process attached to a power plant will increase this number. We also emphasize that for the present analysis we treat the flue gas as a binary gas mixture of 14% CO_2 and 86% N_2This assumption allows us to focus first on the energy consumption of these materials. If the energy consumption looks sufficiently attractive relative to other processes, additional criteria such as sensitivity to other flue gas components (e.g., H2O, SOx, NOx), as well as cost, attrition, stability, and availability can be examined.

3.2 Methods

Since for most of the materials experimental data do not exist, we use molecular simulations to predict the adsorption isotherms. As input, these simulations require the crystal structure of the materials and a force field describing the interactions. In addition, by accelerating computationally expensive steps in molecular simulation using GPUs, we enable screening of materials in a high-throughput manner.

Crystal Structures

For the all-silica zeolite structures, we used the experimental zeolite crystal structures[28] and the database with predicted, fully optimized zeolite crystal structures.[52,79] This database was constructed by searching the chemical space of possible SiO2 structures that are zeolite-like. This was done by examining all 230 space groups and a wide range of unit cell dimensions and silicon densities. Symmetry operations acting upon crystalographically unique atoms were used to generate the full unit cell structure. A Monte Carlo procedure was used to sample

this vast space of possibilities giving 2.6 million topologically distinct zeolite-like structures. These structures were optimized by detailed interatomic potentials.[80,81] Depending on the force field 330,000-590,000 of these structures are thermodynamically accessible, with energies 0-30kJ/mol-Si above αquartz. Of these structures we only considered those with pores with a diameter sufficiently large (above 3.25Å) for CO_2 to enter.[82] The structures in this database have topological, geometrical, and diffraction characteristics that are similar to those of known zeolites.[52,79]

In most zeolites the Si can be exchanged with Al, which creates a charge deficit that is compensated by cations (e.g., Na+, H+, Ca2+). The location of these Al sites is known only for a limited number of structures.[18,83] A reasonable starting point[18] is to assume a random distribution of Al over the T-sites such that Loewensteins rule[84] is obeyed, which implies a maximum Al/Si ratio of one. For this ratio and for Al/Si equal to zero we have one unique structure. For the other Al/Si ratios there are many different possible distributions of the Al atoms over the T sites. For these ratios we generated at least ten different Al atom distributions and the cations were subsequently added at the minimum energy positions.[67] Each distribution can have a slightly different adsorption isotherm and we averaged the parasitic energy.[83] In addition, we compared the results for systems in which the cations were fixed at the minimum energy configurations, with simulations in which the cations were free to move. For structures with a low Henry coefficient, we found a lower parasitic energy compared to a system with moving cations. For those structures with optimal Henry coefficients, these differences were negligible.

Zeolitic imidazolate frameworks (ZIFs) are a class of metal-organic frameworks that have a pore topology that is isomorphic with the zeolite structures.[29,32] In ZIFs the transition metal atoms (M) replace the Si atoms and imidazolates (IM) replace bridging oxides in zeolites. Given that the MIMM angle is similar to the SiOSi angle, ZIFs form 3D networks with topologies that are similar to zeolites. We applied this analogy to the zeolite database to generate ZIFs using the ZEO++ code.[82] In the reported zinc and IM-based ZIFs with IZA zeolite topologies[29] the distance between zinc atoms and the center of IM rings is about 1.95 times larger than the Si-O distance in zeolites. A ZIF structure was generated by scaling the unit cell of the corresponding zeolite structure by the same factor and exchanging each oxygen atom with an IM group and each Si atom with a Zn atom. We have validated the resulting ZIF geometries by comparing geometries of two structures for which the experimental geometries are known: ZIF-3 (DFT) and ZIF-10 (MER). The observed differences in the geometries do not translate into significant differences in the parasitic energy.

Model and Simulation details

Calero and co-workers[65,66] have developed a force field that accurately reproduces the experimental isotherms in zeolites. For ZIFs, parameters for the framework atoms were taken from the DREIDING force field[85] and parameters for CO_2 and N_2 were taken from the TraPPE force field.[86] Framework-molecule interaction parameters were calculated using the Lorentz-Berthelot mixing rules. Partial charges for ZIF framework atoms were computed using the

connectivity based approach of Zhong and Xu.[87] Adsorption isotherms were calculated using grand canonical Monte Carlo simulations (GCMC).[22] The experimental equations of state are used to convert the chemical potentials into (partial) pressures.

GPU Calculations

To screen a large number of zeolite and ZIF structures we developed a graphics processing unit (GPU) code to accelerate the molecular simulations. We focus on computing the Henry coefficients and the heats of adsorption. The algorithm is divided into three different routines: (1) energy grid construction, (2) pocket blocking, and (3) Widom test particle insertion.

1. Energy grid construction: To save computational time we construct a grid, giving the energies of the atoms at the grid positions in the unit cell of a framework.[18] The energy grid has a mesh size of 0.1 and the interaction between the gas molecule and all of the framework atoms is modeled by the Lennard-Jones potential and the Coulomb potential, with Ewald summations used to calculate the latter. Each of the grid points maps to a single CUDA (Compute Unified Device Architecture) thread and the pairwise potentials are computed in parallel across different CUDA blocks.[88] The positions of the framework atoms are put inside the fast constant memory in the GPU to expedite calculations. At the end of the routine, the array that contains the energy values is transferred from the GPU to the CPU as an input to the pocket blocking routine.

2. Pocket blocking: In a GCMC simulation, one can insert molecules in pockets that are inaccessible from the outside.[89] The void space analysis algorithm[90] is used to detect and block these inaccessible pockets.[91] We use the values from the energy grid to determine the accessibility of a particular configuration/point in the unit cell using the (multicore) CPU, as this routine does not map well to the GPU architecture. The discrete energy grid is mapped to a binary grid of accessible/ inaccessible points based on a certain threshold value that is chosen to be large enough such that on an experimental time scale, the pocket is considered inaccessible. Finally, we utilize a parallel flood fill algorithm to segment the grid into connected, accessible regions. These regions are then classified as either channels or inaccessible pockets, and we set all grid points inside pockets to a very high-energy value.

3. Widom test particle insertion: utilizing this revised energy grid, we can calculate both the Henry coefficients and the heats of adsorption using Widom insertion moves.[22] We randomly insert a guest molecule inside the simulation box and calculate both the Boltzmann factor and the energy values for the particular guest molecule configuration. We can use interpolating functions to estimate the energy values at points that are not directly on the grid. In the GPU architecture, each CUDA thread can conduct independent Widom insertion.

Overall, most of the computational wall time is spent in the GPU energy grid construction routine. In this routine, there is roughly a factor of 50 in performance improvement going to the GPU (Tesla C2050 Fermi) from the CPU (single core of a 2.4 GHz Intel 5530 Xeon).

3.3 Results and discussion

To determine the minimum parasitic energy of a material, the most important data are the (mixture) adsorption isotherms. As the experimental adsorption isotherms are known for only very few materials, we rely on molecular simulation to predict these isotherms for the different materials. Conventional grand canonical Monte Carlo (GCMC) simulations allow us to predict a complete isotherm on the basis of the crystal structure of the material.[18,22] These simulations, however, require on the order of days of CPU time, which is prohibitively slow to screen hundreds of thousands of materials. To obtain adsorption isotherms in a high-throughput manner, we have developed an efficient algorithm that allows us to obtain a complete isotherm in a few seconds on a graphical processing unit (GPU). Our method relies on the observation that pure component adsorption isotherms in these materials can be accurately described using dual- or single-site Langmuir isotherms:[63]

$$q = \sum_{j=1}^{N} \frac{K_{i,j} P_i}{1 + \frac{K_{i,j}}{q_{sat_{i,j}}} P_i} \tag{3.3}$$

where q_i is the loading at the partial pressure P_i of the component i, $K_{i,j}$ is the Henry coefficient, and $q_{sat_{i,j}}$ is the saturation loading of the component i corresponding to adsorption site j. In our model, only the single-site (N equal to 1) isotherm was adopted for N_2 while either single- or dual-site (N equal to 2) isotherms were applied for CO_2The temperature dependence of the Henry coefficients follows directly from the heats of adsorption, both of which were obtained from molecular simulations. The total saturation loading of the pure component gas was calculated using a correlation of guest molecule density in the framework to pore diameter. For CO_2 adsorption, the use of dual-site isotherms is required for structures that contain particularly strong adsorption sites; this behavior arises because CO_2 first adsorbs at these sites, and only once all these positions are saturated in the rest of the material. Figures 3.2a and 3.2d illustrate the difference between materials best described by single-site and dual-site isotherms, respectively. The long tail at low energies in the energy distribution is a signature of the presence of these strong adsorption sites. If such a signature exists, we use a dual-site description; otherwise, the isotherms are described using a single site. Figure 3.2e shows a typical case of such a dual site isotherm for pure CO_2One observes a plateau in the isotherm at low pressure, which results from the saturation of the strong adsorption sites. Each strong adsorption site can generally accommodate only one CO_2 molecule, so the saturation loading for these sites is just the sum of the number of unique sites. We have developed an automated algorithm to identify the presence of these sites during molecular simulation and accordingly divide the structure into two regions, computing their

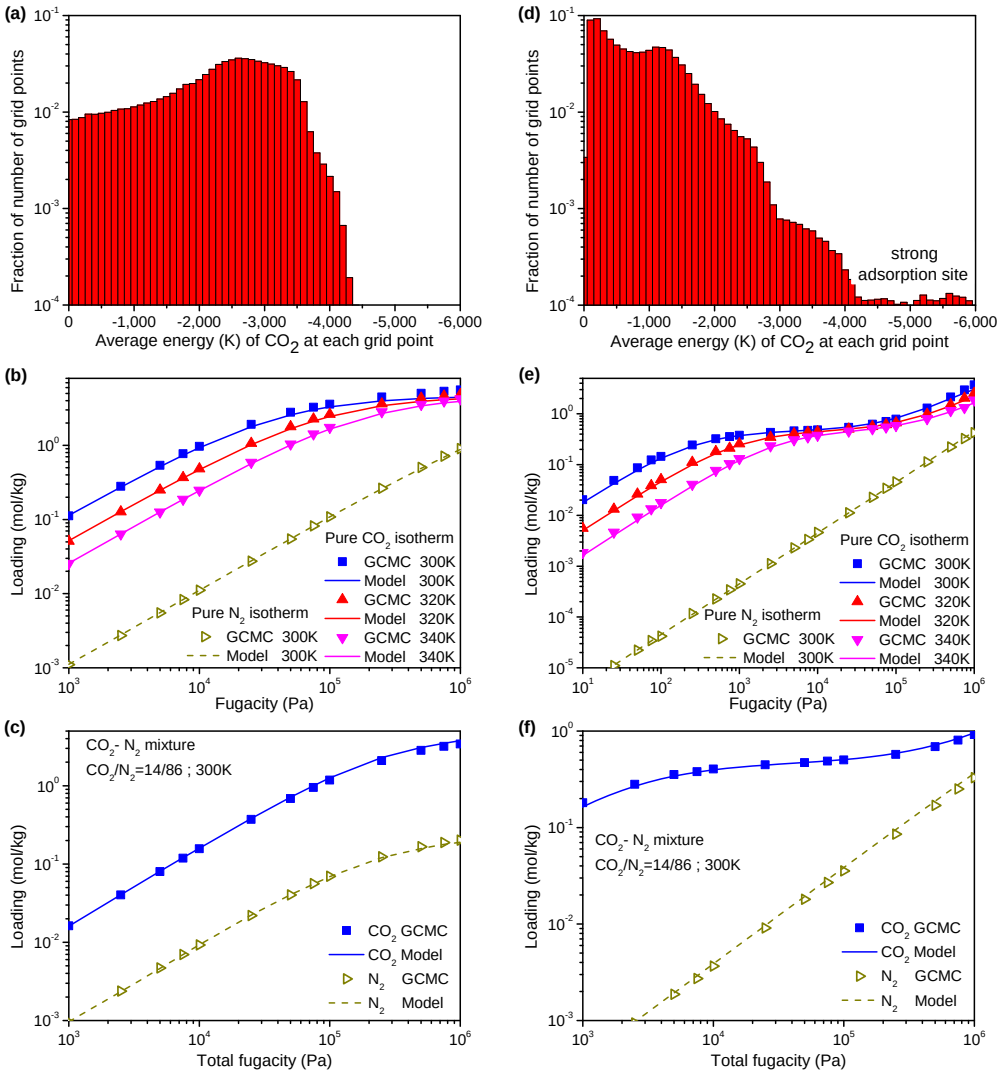

Figure 3.2: (Mixture) adsorption isotherms. Probability distribution of the energies of a particle inserted in the pores (top), pure component isotherms for CO_2 and N_2 and pure CO_2 isotherms at different temperatures (middle) and mixture isotherms (bottom) for two materials: the zeolite SIV ((a), (b), (c)) and the predicted zeolite PCOD8286959 ((d), (e), (f)). The symbols are the results from the GCMC simulations and the lines are the results of our methodology utilizing the GPU calculations.

own associated Henry coefficients, heats of adsorption, and saturation loadings. Figures 3.2b and 3.2e demonstrate that our model is able to predict the correct temperature dependence of the pure component isotherms.

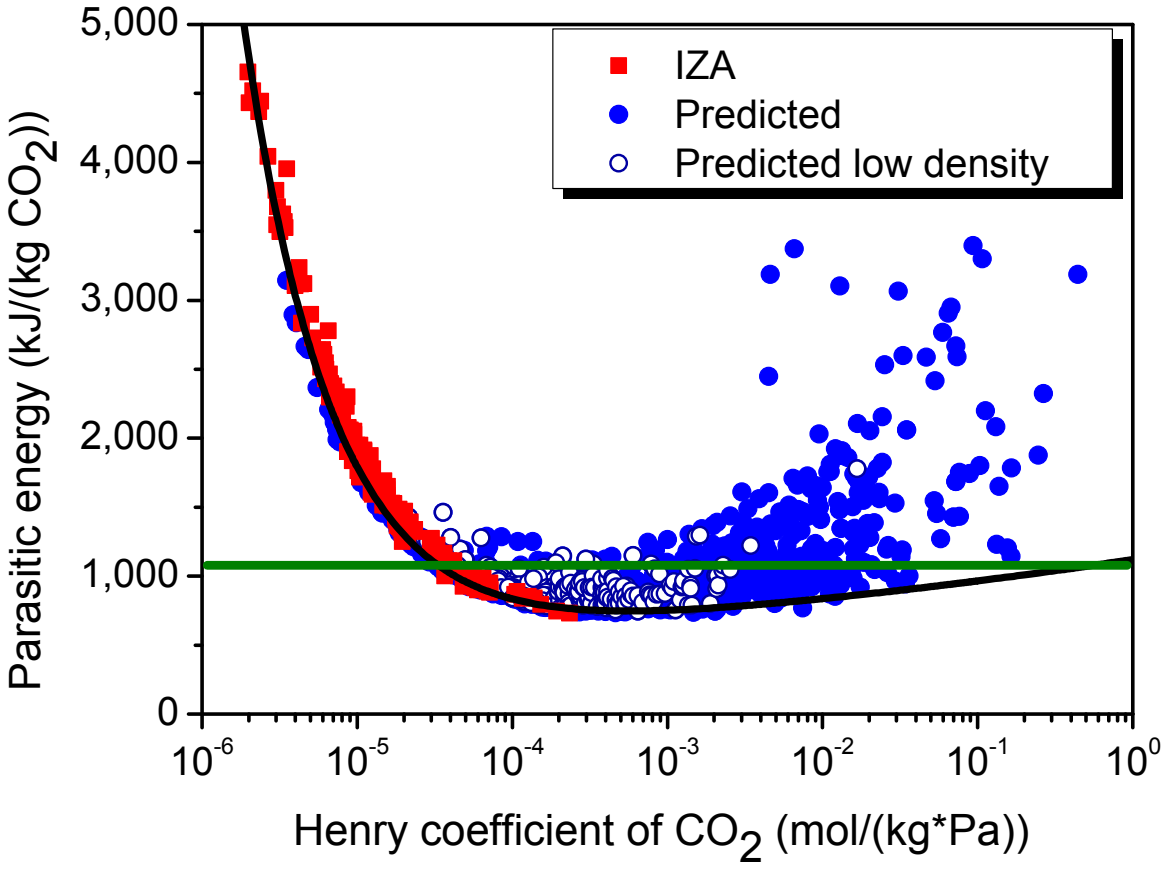

Figure 3.3: Parasitic energy as a function of the Henry coefficient of CO_2 for all silica zeolite structures. We compare the International Zeolite Association (IZA) zeolite structures (red squares) with the predicted structures (blue circles). The open blue circles are computationally predicted structures near the low-density feasibility line, which are most likely to be synthesizable. The green lines give the parasitic energy of the current MEA technology, and the black line is the minimal parasitic energy observed for a given value of the Henry coefficient in the all-silica structures.

The most commonly used method to predict mixture adsorption isotherms is ideal adsorbed solution theory (IAST).[34] However, as carbon capture of flue gases occurs at relatively low pressure, competitive Langmuir isotherms give an equally good description. In case a dual-site model for CO_2 is used, we assume that N_2 is not able to compete with CO_2 at the stronger adsorption site, and take the saturation value for N_2 to be the same as CO_2

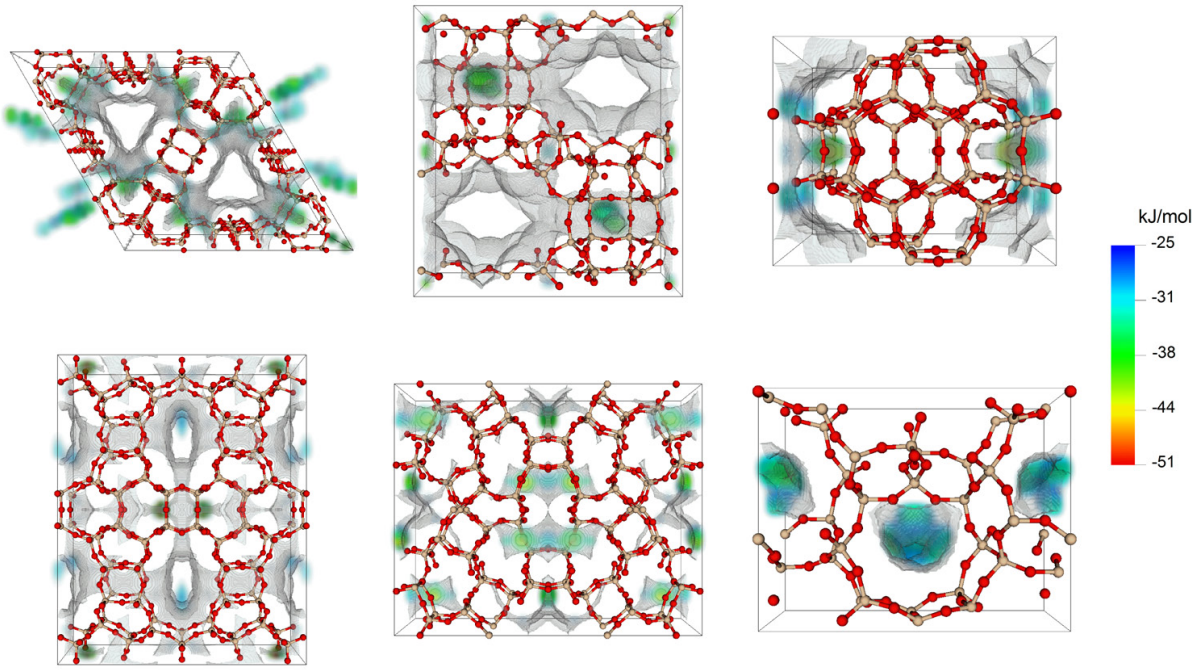

Figure 3.4: Some examples of the optimal all-silica structures; out of the 50 top performing materials we selected the six most diverse. The figures show the atoms of materials as ball and stick (O, red; Si, tan). The surface gives the local free energies in the pores of the material, where warmer colors indicate the dominant CO_2 adsorption sites.

outside of the strong adsorption region, which is required for consistency with the assumption of the competitive adsorption isotherm.[92] To test the reliability of the competitive Langmuir model in predicting the mixture isotherms on the basis of the pure components, we used the GCMC simulated mixture adsorption isotherms as experimental data to test whether the Langmuir model correctly predicts these mixture isotherms given the predicted pure component isotherms. We have tested over 50 different structures and for all systems, the competitive model accurately reproduces the mixture isotherms over a large range of pressures, including the partial pressures relevant for flue gas separations. Figures 3.2c and 3.2f demonstrate the performance of the competitive isotherm model with the corresponding GCMC simulations.

To analyze the effect of these uncertainties on the overall parasitic energies, we selected a set of materials that spanned the range of parasitic energies. To simulate the propagation of possible errors on the thermodynamic input parameters in the parasitic energy, we changed each of these values by multiplying the actual value of a parameters by a factor, which was randomly selected from the interval [0.8, 1.2], i.e., a maximum possible error is plus or minus 20% on each of the thermodynamic variables. In this way, we generated, for each of

the selected parasitic energies, 25 different sets of parameters. Figure 3.5 shows how these uncertainties propagate for a given value of the parasitic energy. We see that for high values of the parasitic energy, the results are much more sensitive. The reason is that small changes in the Henry coefficient have a large effect on the parasitic energy. In contrast, for low values of the parasitic energy the results are robust. This is consistent with the observation that we have for these materials a very broad optimum. Hence, some variations in the parameters have little influence, as at slightly different conditions a very similar optimal parasitic energy can be found. As we are mainly interested in materials with a low parasitic energy, this analysis shows that a 20% uncertainty in the main thermodynamic parameters should not have a significant influence on our estimates of the parasitic energy.

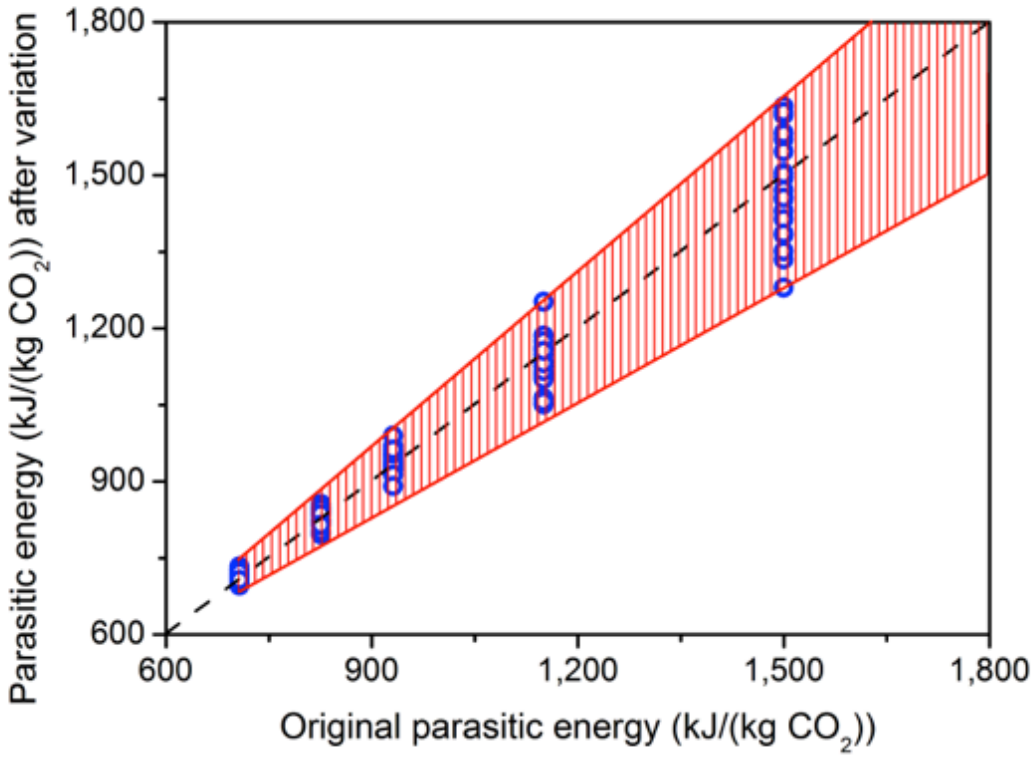

Figure 3.5: Uncertainties in the estimates of the parasitic energies. The blue dots are the 25 parameters sets for which we recalculated the parasitic energy after a change of +/- 20% of all parameters. The red line gives the upper and lower bounds of the errors in these sets.

Figure 3.3 shows the optimized parasitic energy as a function of the CO_2 Henry coefficient for all known zeolite structures. For these materials we observe a monotonically decreasing parasitic energy as a function of the Henry coefficient. To investigate the lowest parasitic

energy that can be obtained using these materials, we perform calculations on a database containing over three hundred thousand predicted zeolite structures.[52] These calculations identify predicted structures with parasitic energy that is lower than can be obtained for the known structures. Figure 3.4 shows some of the structures that have near-optimal parasitic energy.

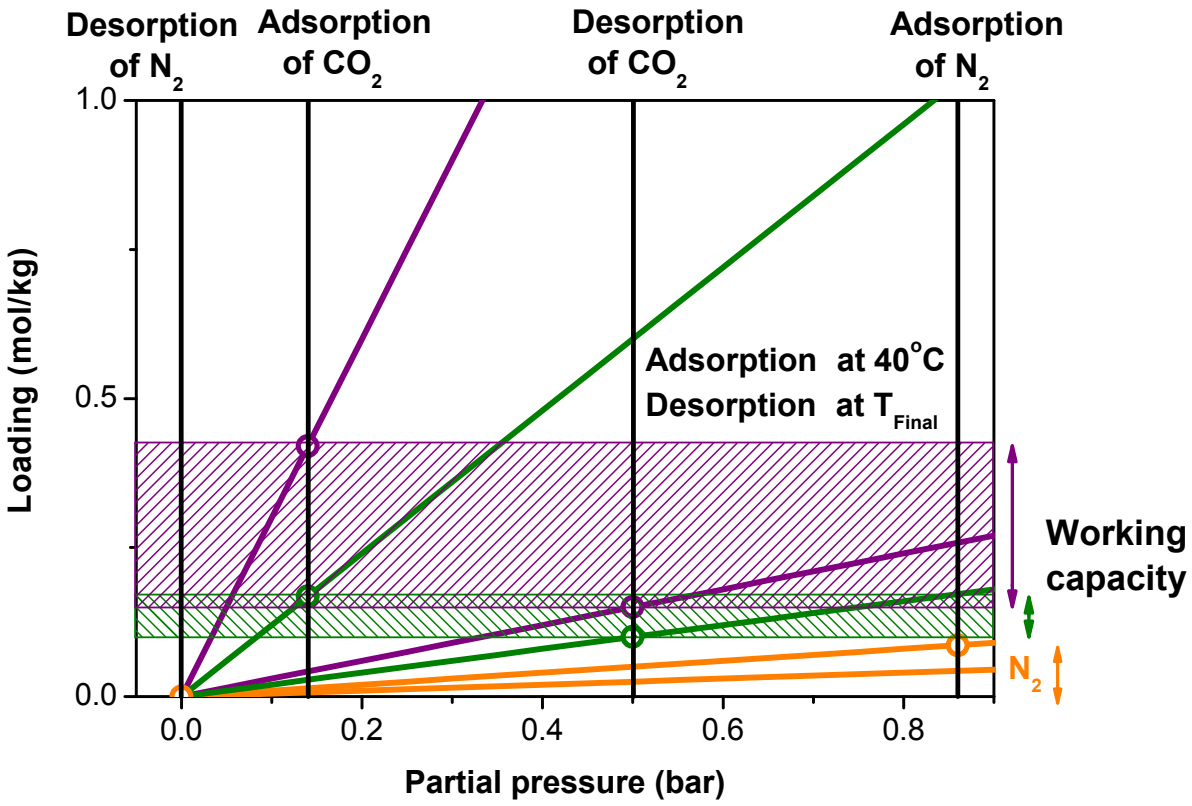

Figure 3.6: Adsorption isotherms. The loading in the zeolite is plotted as a function of the partial pressure of CO_2 (green or purple) or N_2 (orange). Adsorption is set by the flue gas conditions (40C, 1 atm and 14% CO_2 and 86% N_2). The working capacity follows from the difference in the amount of adsorbed CO_2 at adsorption and desorption conditions. A material for which the Henry coefficient is sufficiently low that both the adsorption and desorption are in the Henry regime. A low Henry coefficient (green) gives a relatively small working capacity and purity of the product stream. Increasing the Henry coefficient (purple) gives a significant increase of the working capacity.

The parasitic energy as a function of the Henry coefficient shows three regimes. The mixture isotherms in these regimes are shown schematically in Figures 3.6, 3.7, 3.8. Adsorption of CO_2 takes place at flue gas conditions (1 atm and 40 °C). The subsequent desorption is achieved by decreasing the (partial) pressure and/or increasing the temperature. The differ-

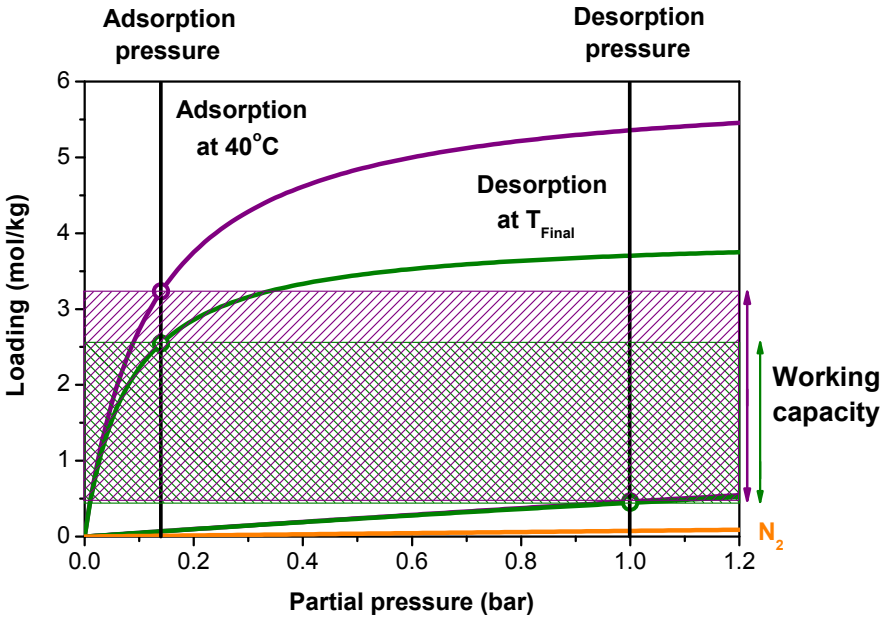

Figure 3.7: Adsorption isotherms and working capacity for a material with a moderate Henry coefficient for CO_2 that saturate in the pressure range relevant for post-combustion separations. If the Henry coefficient becomes much larger, the number of adsorbed CO_2 molecules is so large that CO_2-CO_2 interactions in the materials are important at the partial pressure of CO_2 corresponding with flue gas conditions. Hence, the adsorption cannot be characterized with a Henry coefficient only.

ence in CO_2 concentration between adsorption and desorption defines the working capacity of a material and gives the amount of CO_2 that is removed in an adsorption cycle. For materials with a small Henry coefficient (see Figure 3.6), the performance is poor because the working capacity is small, yet the entire system needs to be heated to the desorption conditions, giving a high parasitic energy. In addition, the adsorption of CO_2 is of the same order of magnitude as N_2 in these materials and hence the selectivity of such a material is unusably low. Materials with a larger Henry coefficient have a significantly larger working capacity and correspondingly lower parasitic energy. This trend continues until the Henry coefficient of the material is so large that at flue gas conditions the pressure is too high for the CO_2 adsorption to be in the linear regime. Figure 3.7 shows that at these conditions the CO_2 loading at the adsorbed state is not fully determined by the Henry coefficient anymore, and that materials with the same Henry coefficient have different working capacities depending on the pore volume. Figure 3.8 illustrates that at even larger Henry coefficients the adsorption of CO_2 becomes so strong that it becomes increasingly difficult to regenerate the material. Another important observation is that we have a broad optimum. The reason for this broad minimum is that the Henry coefficient shows a strong correlation with the heat

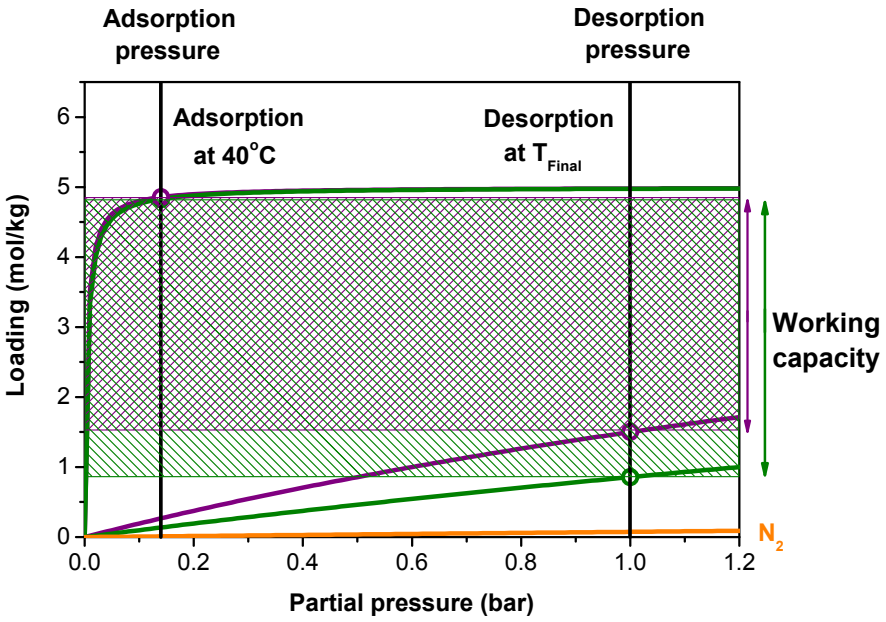

Figure 3.8: Adsorption isotherms and working capacity for a material with a high Henry coefficient for CO_2. For those materials with a very high Henry coefficient, a further increase of the Henry coefficient will have little effect on the uptake value at adsorption as this is now dominated by the pore volume. For desorption, however, increasing the Henry coefficient will further decrease the working capacity.

of adsorption, and the heat of adsorption has two opposing contributions to the parasitic energy. As the temperature dependence of the Henry coefficient is proportional to the heat of adsorption, a higher heat of adsorption increases the working capacity. While this reduces the parasitic energy, it is offset by the requirement to supply more energy to desorb CO_2 which again increases the parasitic energy.

Our screening shows a large set of zeolite structures that have a parasitic energy well below the current technology (1060 kJ/kg CO_2). Inspection of these optimal structures highlights their diversity: we find one-, two-, or three-dimensional channel structures, cage-like topologies, and more complex geometries. To illustrate this point we show in Figure 3.4 a diverse sample of structures[93] contained in the optimal zeolites. It is interesting to compare these with the optimal known zeolite structures in Figure 3.3. Several of the known zeolite structures have a sufficiently low parasitic energy, however, most of these known structures are one-dimensional channels, which may suffer from severe diffusion limitations.[74] By contrast, many of the predicted zeolite structures have adsorption sites, where CO_2 strongly adsorbs, along channels with larger diameters. Transport of CO_2 to and from the sites of adsorption occurs via the larger channels, so diffusion is not expected to be a limiting factor here. Interestingly, none of the known zeolites has this characteristic feature, and we

consider this observation to be a significant discovery. This discovery was facilitated through the screening of an exhaustive number of possible topologies.

A common feature of most optimal materials is a set of local regions of the structure that bind CO_2 preferentially, leading to dual-site adsorption behavior. Figure 3.9 shows the parasitic energy as a function of the binding energy of a CO_2 molecule. To this figure we added those materials that have (near) optimal Henry coefficients, but without such dual-site behavior, which includes some of the known zeolite structures. We observe a similar correlation as for the Henry coefficient, since the binding energy dominates the Henry coefficient for structures with these preferential sites. The binding energy needs to be optimal: too low and the material adsorbs too little CO_2 too high and the material becomes too difficult to regenerate. Figure 3.9 further shows that the parasitic energy is influenced by the density of strong adsorption sites in the material; the optimal materials exhibit the largest number of strong adsorption sites per unit volume. This observation is important as it explains why these materials exhibit a lower limit for the parasitic energy. The existence of a strong adsorption site requires a minimum amount of zeolite material, which, combined with the size of a CO_2 molecule, gives an upper limit to the total number of such local regions that can exist per unit volume.

An important practical question is whether we can synthesize these optimal materials. As the synthesis conditions of the known zeolites favor the formation of low-density structures,[79] one expects that among the predicted structures these low-density structures are the most likely ones to be synthesized. As highlighted in Figure 3.3, this subset has many structures with optimal performance indeed. Recent developments[94] in novel structure directing agents may make it possible to synthesize some of these structures.

An alternative strategy to create optimal Henry coefficients is to synthesize zeolites with different Al:Si ratios. In aluminosilicate zeolites, cations are present in the pores to compensate for the charge imbalance introduced by the Al^{3+} that replaces a Si^{4+}. Figure 3.10 shows the effect of cations on the parasitic energy for the known zeolites for different Al:Si ratios. Cations create adsorption sites for CO_2 but also reduce the pore volume. The net result on the parasitic energy of these two effects depends on the particular structure. The addition of cations to low Henry coefficient structures causes a decrease in the parasitic energy due to the increased number of adsorption sites; however, additional cations eventually increases the parasitic energy as the pore volume decreases. By contrast, addition of cations to near-optimal Henry coefficient structures increases the parasitic energy since the decrease in pore volume dominates. It is important to stress that every structure has its own optimal Al:Si ratio. Comparison with the parasitic energy for the all-silica structures shows that the addition of cations does not yield a material that has a lower parasitic energy for the same Henry coefficient. This observation is consistent with the notion that one has to create an adsorption site with exactly the right adsorption strength and that there is a limit to the maximum number of adsorption sites per unit volume.

Figure 3.11 shows the parasitic energy for ZIFs. For these materials, the overall parasitic energy is higher than for zeolites. As we have focused on the simplest linker (imidazole), the selectivity towards CO_2 is rather low: linkers with higher selectivity will increase the

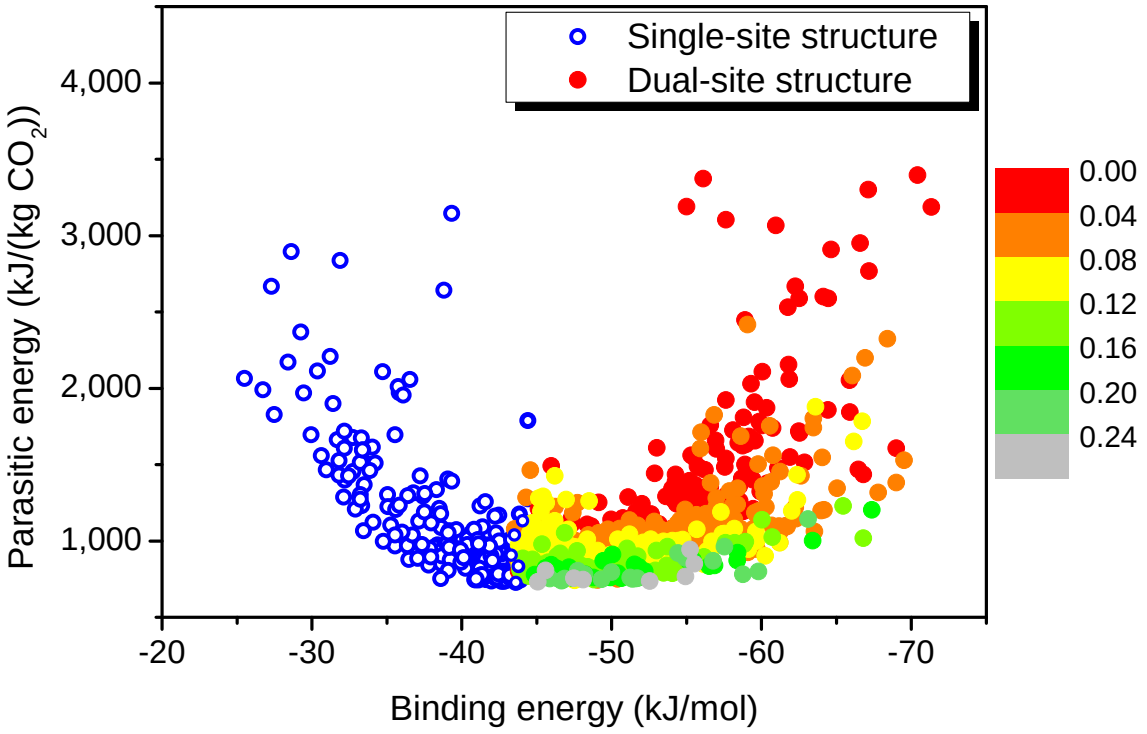

Figure 3.9: Optimal materials. The parasitic energy as a function of the binding energy for a CO_2 molecule. The binding energy is defined as the lowest energy that can be observed in a given structure. If this binding is sufficiently strong, dual-site adsorption behavior will arise. The fraction of each materials volume which is occupied by low-energy strong adsorption sites is displayed as colored solid circles. Structures without these specific features (i.e., single site adsorption behavior) are displayed as open blue circles.

Henry coefficient to a more optimal value and reduce the parasitic energy. Figure 3.12 gives a set of optimal ZIF structures. These structures look very different from the optimal zeolite structures; optimal ZIFs are those in which there are channels where CO_2 can access the non-hydrogen atoms of the structure.

3.4 Summary

There are important experimental consequences to our results. Our metric provides a direct insight into the overall performance of a material in an actual carbon capture process. In this

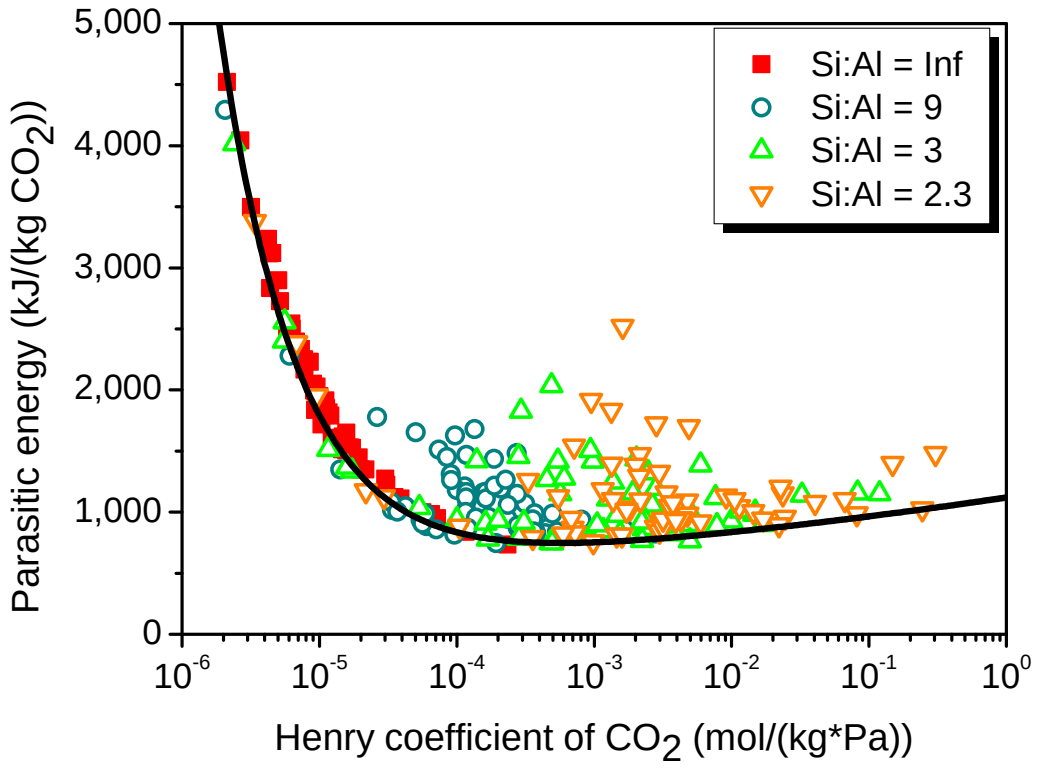

Figure 3.10: Parasitic energy for zeolites with cations. The parasitic energy as a function of the CO_2 Henry coefficient for known zeolite structures with different Al/Si ratios is shown. The all-silica IZA structures are shown as red squares and the corresponding structures with different cation concentrations are labelled as follows: Si:Al=9 (blue circles), Si:Al =3 (green triangles up), and Si:Al =2.3 (orange triangles down)).

context, it is instructive to compare our metric with the recently proposed alternative metric based on the adsorption breakthrough time.[75] Materials with a higher Henry coefficient, for a given saturation loading, will give a longer breakthrough time. However, as this study shows, materials with extremely high Henry coefficients perform poorly because the regeneration step cannot be ignored in a carbon capture process. This illustrates the limitation of focussing on a single material property rather than the entire process.

Our screening establishes a theoretical limit for the minimal parasitic energy that can be achieved for a class of materials. Such a target will be useful to focus experimental efforts to synthesize such materials. Our screening gives for each class of material a unique structure that gives the best performance. However, from a practical point of view, 1-3% higher parasitic energies will not make the difference. To have many near optimal structures

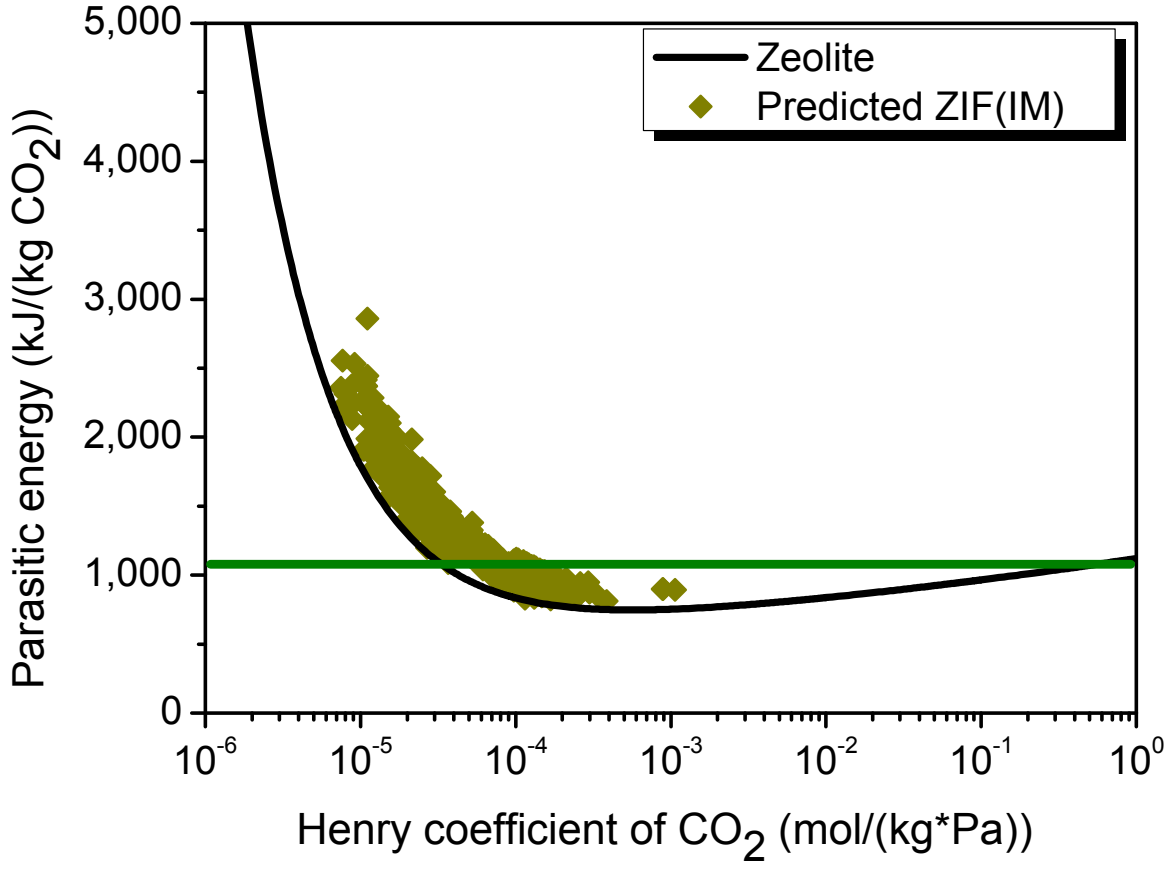

Figure 3.11: The parasitic energy as a function of the CO_2 Henry coefficient for ZIFs is shown. The green lines give the parasitic energy of the current MEA technology, and the black line is the minimal parasitic energy calculated for a given value of the Henry coefficient in the all-silica structures. In this graph, we plotted a representative fraction of all structures. More data can be found at *www.carboncapturematerials.org*.

is very important as it increases the changes one of these structures can be synthesized. To facilitate this synthesis effort, all of these structures, together with all physical properties that lead to the increase in performance, are available online (see Appendix B for details).[95]

A specific outcome of our study is that an optimal carbon capture material has a sufficient number of adsorption sites with a binding energy that is sufficiently large to be selective, but not so large that it becomes difficult to desorb. This is a very general conclusion and explains why our parasitic energy curve holds for all materials we have studied. This parasitic energy curve can be used as a reference to benchmark other materials.

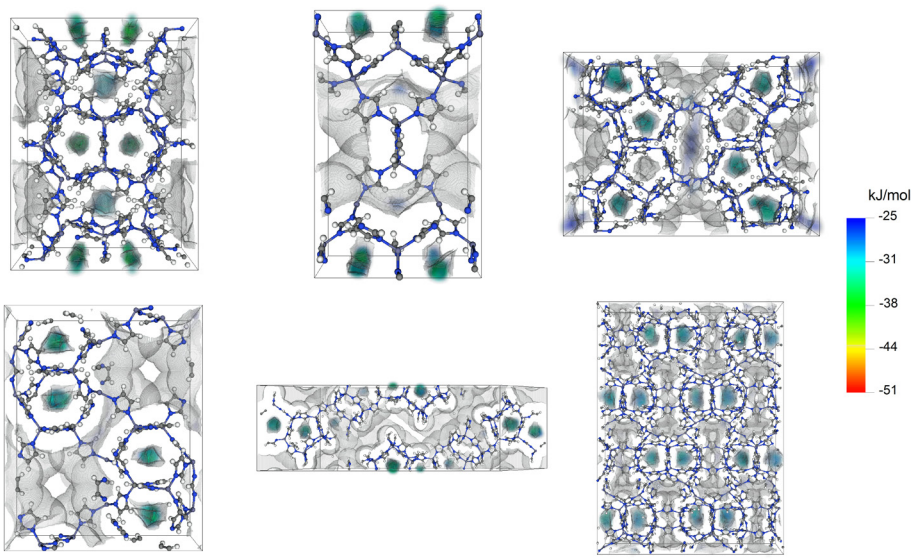

Figure 3.12: Out of the 50 top performing ZIFs, we selected the six most diverse. The figures show the atoms of materials as ball and stick (Zn blue-grey, N blue, H white, and C grey). The surface gives the local free energies in the pores of the material.

Chapter 4

Ab initio carbon capture in open-site metal organic frameworks

Molecular simulations rely on accurate parameterization to correctly predict adsorption and diffusion data required to evaluate materials for use as solid adsorbents. Force fields used in grand canonical Monte Carlo simulations can be parameterized by fitting to experimental data, however, when considering new materials or materials that have not yet been synthesized, a different approach is required. Quantum chemical calculations can be used to map out the potential energy surface for an adsorbate molecule inside the pores of a material and can be fit to a classical potential form. In this work, we studied the use of quantum calculations to parameterize a force field for CO_2 and N_2 in MOF-74, a new MOF material that has been shown to selectively adsorb CO_2 at the partial pressures relevant to carbon capture. This selectivity is a result of metal atoms that are not saturated at all its coordination sites and can interact strongly with CO_2.

4.1 Background

A promising class of adsorbent materials for CO_2 separations is metal organic frameworks (MOFs).[53,54] MOFs are crystalline materials consisting of metal centers connected by organic linkers. These materials have an extremely large internal surface area and, compared to other common adsorbents, promise very specific customization of their chemistry. By changing the metal and the linker one can generate many millions of possible materials. In practice one can only synthesize a very small fraction of these materials, and it is important to develop a theoretical method that supports experimental efforts to identify an ideal MOF for carbon capture. A key aspect is the ability to predict the properties of a MOF before the material is synthesized. At present it is possible to carry our accurate quantum chemical

Material in this chapter is based on Dzubak et al., *Nat. Chem.*, *4*, **2012**, 810-816 (doi:10.1038/nchem.1432).

calculations on these types of systems.[96] State-of-the-art density functional theory (DFT) calculations provide important insights in the energetics and siting of CO_2 at zero Kelvin.[96] The separation of flue gas, however, requires thermodynamic information (e.g. adsorption isotherms) at flue gas conditions (40 ^{circ}C and 1 atm). This type of information can be obtained from molecular simulation using classical force fields.

For some classes of MOFs these predictions still pose significant difficulties, namely for MOFs with open metal sites.[97–104] These materials crystalize in such a way that both linkers and solvent molecules coordinate to the metal centers. The stability of the materials allows the removal of the solvent, which creates an open metal site. This site has a very high affinity to CO_2 making the material very promising for carbon capture. Reasonable predictions on the ability of a material to adsorb CO_2 can be often made using existing generic force fields.[74,76,105] However, for these materials Krishna and van Baten observed that, exactly at the conditions that are important for flue gas capture, the universal force field (UFF[106]) fails to correctly describe the adsorption of CO_2.[74] The reason is that an open metal site imposes a very different chemical environment compared with those considered in the development of these force fields.[101]

Ideally one would like to use state-of-the-art quantum chemical calculations to evaluate the energy for each state point of a grand canonical Monte Carlo (GCMC) simulation to compute the adsorption isotherm. However, such calculations would require millions of years of CPU time. In this work, we have developed a methodology to obtain accurate force fields from quantum calculations that correctly predict the adsorption isotherms of CO_2 and N_2 on MOFs with open metal sites. Our approach is based on the NEMO methodology,[107,108] which decomposes the total electronic interaction energy obtained from quantum chemical calculations into the various contributions (electrostatic, repulsive, dispersion, etc.). The force field expression closely matches the functional form of the NEMO decomposition, allowing us to accurately fit the parameters of the force field to reproduce the quantum calculations. We have developed a strategy to obtain the interaction for each atom type of the MOF with CO_2 (or N_2).

The UFF[106] or Dreiding[85] force fields are frequently used to describe the interaction of gas molecules with the atoms of the MOF.[76,105,109] In these force fields, the non-bonded energy is described by a Lennard-Jones potential plus Coulomb interactions. As these force fields are employed for many different systems, the parameters should give a reasonable description of the interaction of CO_2 with Mg in many different chemical environments (for example, a zeolite instead of a MOF). Our quantum calculations show that, due to the open metal site, CO_2 (and N_2) can get closer to the metal site than what predicted by the UFF/Dreiding force fields. The aim of this work is to develop a systematic methodology to obtain force fields from quantum chemical calculations that correctly describe the interaction of the guest gas with the open metal site. To our knowledge no existing force field is able to describe this interaction correctly.

Our aim is to determine a complete isotherm at flue gas conditions, and this requires taking into account ensemble averages involving billions of different configurations. When developing a force field one has therefore to ensure that a large number of different configu-

rations are described in a reasonable way, and not just the minimum energy configuration, which is usually the focus of a quantum chemical calculation.

4.2 Methods

In our force field, the electrostatic interactions were described by charges estimated using the LoProp scheme.[110] Initial tests showed that the repulsive interactions could not be accurately described with a Lennard-Jones potential. A modified Buckingham potential was used in addition to the Coulomb interaction:

$$u^{rep}(r) = \begin{cases} \infty & r \leq r_{min} \\ A\exp(-Br) & r > r_{min} \end{cases} \tag{4.1}$$

which can be fitted very accurately. For the attractive part we used, in addition to the conventional r^{-6} term, an r^{-5} term to obtain a better representation of the decomposed energies:

$$u^{att}(r) = \frac{C}{r^5} + \frac{D}{r^6} \tag{4.2}$$

To determine the parameters of this force field, we used the following procedure. First, we generated sets of configurations organized into paths, with one path for each type of atom in the framework, i.e., Mg, O_a, O_b, O_c, C_a, C_b, C_c, and C_d in Mg-MOF-74 (see Figure 4.1). Along each path CO_2 (or N_2) approaches a specific atom type in such a way that for each configuration on this path the MP2 energy mainly represent the interaction of CO_2 (or N_2) with this particular atom type. These energies should thus contribute the most to the fitting of the parameters of the force field for this particular atom type. As it is infeasible to carry out MP2 calculations for the full periodic MOF, we define for each atom type (and corresponding path) a finite cluster of atoms within the MOF that should represent the electronic environment of this atom type in the MOF. The size of the cluster is set such that the interaction of CO_2 (or N_2) with this atom-type mimics the interaction in the full MOF.

The decomposition in electrostatic, repulsive, and attractive interactions for each path allowed us to fit this relatively large number of force field parameters efficiently and accurately. This procedure was used to determine the interactions of the end atom of the guest molecules (O of CO_2) with the atoms of the MOF. We then performed Monte Carlo simulations, which showed that the oxygen atoms dominate the interactions with the framework. The interactions with the interior atom of the guest molecules (i.e. carbon of CO_2) were too weak to be included in this process.

MP2 calculations

In this work, we have used second-order Møller-Plesset perturbation theory (MP2) to describe interactions of CO_2 and N_2 with MOF sites. MP2 is adequate for the treatment of electron correlation in cases where strong correlations are not present. In Mg-MOF-74, we have

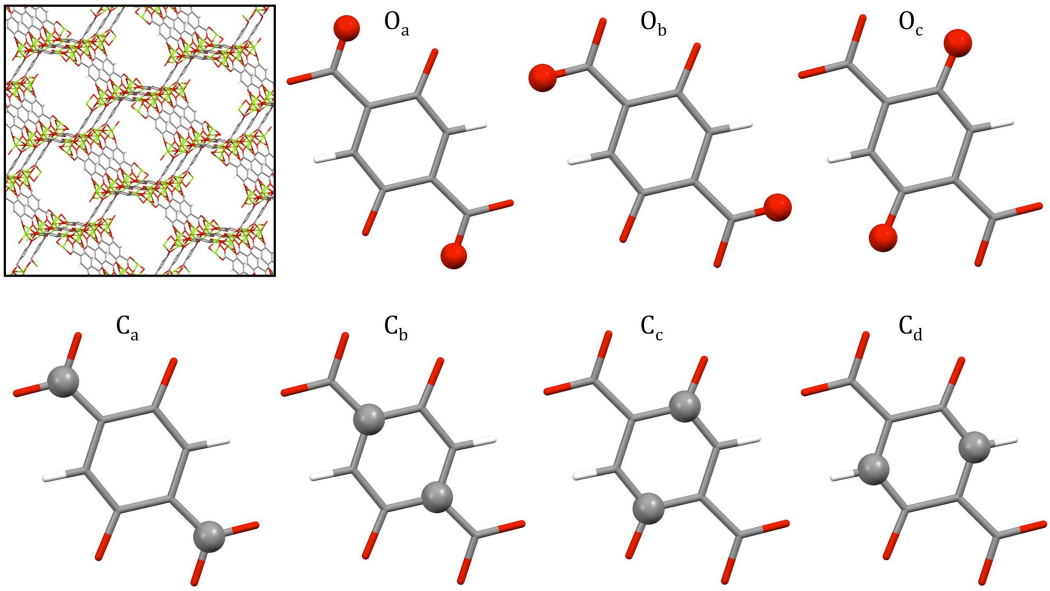

Figure 4.1: Atom types used to model the DBC linker molecule in Mg-MOF-74

defined 8 representative clusters of the MOF to compute interactions with the guest, each cluster chosen to best represent the atom type to be parameterized (excluding H atom type). Within each cluster, the basis functions were chosen such that a larger contraction was used for the guest atoms, the atom type being approached in the MOF, and its nearest neighbors, while a smaller contraction was used for all atoms father away. The choice of clusters, basis function contractions, and discussion of convergence are given in Appendix C. The interaction energies were determined by the supermolecular approach, counterpoise corrected for basis set superposition error.[111] All calculations have been performed using the MOLCAS[112] software version 7.6. Resolution of the identity (RI) and Cholesky decomposition (CD) techniques were employed to treat the two electron integrals.[113–115] The Douglas-Kroll Hess Hamiltonian[116] was used in conjunction with atomic natural orbital relativistic correlation consistent (ANO-RCC)[117,118] type of basis functions. At every point of interaction between a molecule and a cluster, three calculations were require to compute the interaction energy, defined by the following equation (dummy functions provide the counterpoise correction for BSSE[111]).

$$E_{int} = E_{\text{MOF + Guest}} - E_{\text{MOF + Dummy Guest}} - E_{\text{Guest + Dummy MOF}} \tag{4.3}$$

Atomic charges

The LoProp method[110] (based on MP2 densities[119]) was used to compute the localized electrostatic moments to second order and the dipole-dipole polarizabilities. This was done for each cluster, CO_2 and N_2. The choice of basis set contractions are identical to those used in computing the interaction energy. Output from this procedure provides for each atom: scalar charge, 3 components of dipole moment, 6 components of quadrupole moment, and 6 components of the polarizability. While only the interaction between point charges is used directly in the GCMC simulation, the other values contribute to the NEMO decomposition of the interaction energy.

It is important to note that these charges will be slightly different in each cluster due to the choice of truncation. Since the restriction is not imposed that each atom type has the same charge in the LoProp method (and that the symmetry of the various clusters is different than the symmetry of the periodic structure), the following was performed to assign the atom type charges for direct use in the GCMC simulations. For Mg-MOF-74, the charge for Mg atom type comes from the LoProp charge of the Mg being approached in the Mg cluster; this is not an average of the Mg charges since the local environment around the single Mg is best represented. The same was done for the 7 other atom type clusters, and H atom type was used to balance the overall charge such that the periodic structure remains neutral. All the charge parameters are given in Appendix C.

DFT calculations

Density functional theory (DFT) calculations were used to optimize the crystal structure and to compute the CO_2-MOF interaction energy along some representative paths. Our DFT calculations were performed using the SIESTA,[120] VASP,[121,122] and QuantumEspresso[123] (QE) implementations.

We have tested the validity of the localized-basis set approach (SIESTA) by comparing structural data and energetics with those obtained from a plane-waves approach (QuantumEspresso and VASP). We used the PBE gradient-corrected exchange-correlation functional in SIESTA and VASP while PW91 was employed in QuantumEspresso. Since these two functionals do not account for dispersive forces, we also employed a recent van der Waals functional (vdW-DF)[124] as implemented in SIESTA,[125] in order to properly describe interaction energies.

VASP calculations use projector-augmented-wave (PAW) potentials to describe the interaction between core and valence electrons. C [2s2p], O [2s2p], Mg [3s3p] and Zn [4p3d] valence electrons are explicitly included in the valence. A plane-waves kinetic energy cutoff of 500 eV is used and the integration over the irreducible Brillouin zone is carried out over a 2x2x8 Monkhorst-Pack grid. Atomic positions are relaxed until forces are lower than 0.02 eV/Å.

SIESTA calculations used variationally optimized double-Z polarized basis sets[126] implying the presence of d-orbitals for C, N and O. Non-local, norm-conserving fully separable

Trouiller-Martins pseudopotentials were used. C [2s2p], O [2s2p] and Mg [2s2p3s] electrons were explicitly included in the valence. Real space integrals were performed on a mesh with a 300 Ry cutoff. Geometries were optimized until Hellmann-Feynman forces were smaller than 20 meV/Å. For the interaction energy with CO_2 a counterpoise correction was applied to correct for basis set superposition error. A 2x2x8 Monkhorst-Pack grid was used for the integration over the irreducible Brillouin zone. The integration over the irreducible Brillouin zone is carried over 64 grid points.[127]

Crystal structure

Our calculations relied on an accurate representation of the crystal structure of Mg-MOF-74. Unfortunately at present, single crystals of Mg-MOF-74 have not been obtained and the structural information is therefore obtained from powder diffraction data[128–130] Detailed inspection of these experimental structures shows a significant distortion of the bridging ligand in powder diffraction data (Mg-MOF-74), which is not observed in our DFT calculations.

We used PW91 (QE) and PBE (SIESTA and VASP) to obtain the fully relaxed structure of the MOF. The good agreement between these two approaches confirms the validity of the localized basis set approach employed within SIESTA. The lattice parameters and the C-C bond lengths within the ligand of the relaxed geometry obtained with PW91 (QE) and PBE (SIESTA and VASP) are reported in Table 4.1. Similar results were obtained with D3LYP by Valenzano et al.[96] The fact that four different approaches predict nearly identical crystal structure gives us confidence in the reliability of the theory. It is therefore surprising that a comparison with the experimental structure show such large deviations. For example, we found a deviation of the C_a-C_b and C_d-C_b bond distances by as much as 8% and 7%, respectively.

For Zn-MOF-74, a closely related material, it is possible to synthesize a single crystal and for this material crystal structure can be determined with higher accuracy.[129] In Table 4.1 we have compared the structural data for this material from our DFT (PW91, QE and PBE, VASP) calculations, previous calculations,[96] and experiments.[128,130] For this material our calculated lattice parameters and atomic positions are in an excellent agreement with the experimental data (the largest deviation for C_a-C_b bond length is 1.2%). Given the uncertainties with the experimental structure for Mg-MOF-74 and the excellent agreement we obtained using our DFT approach for Zn-MOF-74, we conclude that the computational structure of DFT is most likely the most reliable representation of Mg-MOF-74. The PBE-VASP structure is therefore used in this work for all our calculations of adsorption isotherm.

Force field parameterization

Tests have shown that the influence of the parameters for the carbon atom of CO_2 on the predicted adsorption behavior was very small, and variations by as much as 30% of the Universal force field parameters[106] had a negligible effect on the adsorption isotherms.

Metal, source	Lattice parameters		Bond lengths			
Method	a	c	C_a-C_b	C_b-C_c	C_c-C_d	C_d-C_b
Mg, this work PW91, QE	26.114	6.917	1.483	1.433	1.399	1.401
Mg, this work PBE, SIESTA	26.260	7.036	1.490	1.436	1.405	1.406
Mg, this work PBE, VASP	26.136	6.942	1.484	1.434	1.401	1.402
Mg, calc.[96] DFT-B3LYP	26.109	6.969	1.493	1.430	1.396	1.399
Mg, exp.[130]	26.026	6.759	1.540	1.314	1.430	1.509
Mg, exp.[128]	25.922	6.863	1.613	1.490	1.526	1.260
Zn, this work PW91, QE	26.095	6.888	1.482	1.430	1.397	1.400
Zn, this work PBE, VASP	26.190	6.935	1.484	1.432	1.399	1.402
Zn, exp.[129]	25.932	6.837	1.500	1.420	1.391	1.398

Table 4.1: Lattice parameters and bond distances for the MOF materials investigated in this work from DFT calculations and experiments. All parameters and distances are expressed in Å

Therefore, we only refined interactions between the oxygens of CO_2 and the atoms of the MOF.

In order to fit the parameters for a particular pair-wise interaction separately, it is important to determine a set of configurations that is dominated by the interaction with the specific atom type of interest. Paths composed of several configurations were generated using the Universal force field for the framework atoms and TraPPE force field[86] for guest molecules (CO_2 or N_2). The orientation of this approaching molecule was calculated by minimizing the repulsive energy between the guest molecule and atoms of the cluster, excluding the atoms with the specified atom type for that cluster. This procedure ensured that the repulsive interaction between the guest molecule and the atoms of the specified atom type dominates the total repulsive energy. Based on the 12-6 Lennard-Jones potential, paths with the minimized repulsive energies (12th order term) between the guest molecule and atoms of the cluster, excluding the atoms with the specified atom type for that cluster, will also have the minimized attractive energies (6th order term), and the same paths can be used to explore both parts of the potential.

For an each configuration on a given path of a guest molecule around a cluster, a MP2 calculation and NEMO decomposition (describe below) were performed to get the individual components of total interaction energy. The repulsion energy and attraction energy were identified for each path with a given guest molecule and were used to build the new force field using the fitting procedure proposed below. In the new force field, a modified Buckingham potential model (equations 4.1 and 4.2) was used to describe the repulsion and attraction energy between the structure and the end atoms of the guest molecules, respectively.

As mentioned above, the repulsion energy between the guest molecule and the target atom type in its corresponding cluster was designed to be the dominant component of the total repulsion energy. The interaction energy between the target atom and the end atoms of the guest molecule can be regarded as the most important component of the total energy. Consequently, during the parameterization procedure only the force field parameters for the interaction between the target atom type and the guest molecule were adjusted to minimize the norm of the difference between NEMO-decomposed repulsion energy and calculated repulsion energy.

Initial guesses for all pair-wise interactions were taken from the Universal force field[106] and TraPPE force fields[86] with the Lorentz-Berthelot mixing rules. The fitting was carried out in two phases. To improve the initial guess, we first took all atoms of a particular element (all O atoms or all C atoms) and simultaneously minimized the error over all paths for that element. This adjustment was done in the order: Mg, O, and C. These parameters were used as the initial guesses for the second phase, where we optimized the force field parameters for each atom type individually with an ordering based on its relative contribution to the total repulsion energy. The ratio of the repulsion energy of the target atom type and the guest molecule to the total repulsion energy was computed, and the paths were taken in order from the highest to lowest ratio. This procedure was repeated iteratively until all the parameters were converged. For the fitting to attractive part of the potential, the procedure is exactly the same as the one described above for the repulsive part, using the same paths identified

above. For these parameters, however, we set the attractive interaction between the interior atom of the guest molecule and the framework atoms to be zero.

NEMO decomposition

Using the MP2 interaction energies as a reference, the NEMO[108] decomposition was used to partition the energy into repulsion, polarization, dispersion, and electrostatic components for all clusters and paths. The electrostatic moments to second order and dipole-dipole polarizabilities were obtained using the LoProp[110] method based on the MP2 densities.[119] The terms were then grouped into repulsive, attractive, and electrostatic terms, where the charge-charge interactions and repulsion remained constant, while the polarization, dispersion, and effects of dipoles and quadrupoles were grouped into attraction terms, for which the parameters were then fitted by atom pairs as described above. Detailed equations for the decomposition are given in Appendix C.

Grand canonical Monte Carlo simulations

Adsorption isotherms for CO_2 and N_2 in Mg-MOF-74 were predicted using the grand canonical Monte Carlo (GCMC) technique, where a constant chemical potential (fugacity), volume, and temperature are imposed.[22] The heat of adsorption was calculated directly using the procedure developed by Vuong and Monson.[131] The energies of guest-framework interactions were computed using the potential model described above and guest-guest interactions were described using the TraPPE force field.[86] Electrostatic energy was computed using the Ewald summation technique. Short-range interactions were cut off and shifted to zero at a distance of 12.8 Å, and the simulation box extended at least twice this distance in all orthogonal directions. No tail correction was used. To accelerate the calculation of molecule-framework interaction energies, the short-range part of the interaction was stored in a pre-computed grid with a spacing of 0.10 and linearly interpolated between grid points. Trajectories were equilibrated for at least 20 million configurations before taking averages over a further 4 million configurations.

4.3 Results and discussion

Figures 4.2A and 4.2B show a typical outcome of the NEMO decomposition of the total MP2 energies of the Mg atom-CO_2 interaction into a repulsive and an attractive contribution, respectively, together with the fitted force fields. The electrostatic (charge-charge) contribution is identical to the leading term of the grouped-term NEMO decomposition, so no fitting is required. This figure illustrates that indeed the interaction of CO_2 with Mg dominates the total energy along this path. The repulsive interactions on this path are accurately described with our force field. Since the attractive interaction contains many different contributions and the functional form of the attractive interaction in our model only approximates the

corresponding MP2 interactions, the fit of the attractive part is less accurate than the one of the repulsive part. Similar results have been obtained for the other paths. Figure 4.2C and 4.2D show that our force field can reproduce the total MP2 energies for all paths within 1-2 kJ/mol.

To further validate our procedure, we compared the energies obtained from our force field with those obtained from DFT calculations on the fully periodic framework for two different paths. These DFT calculations include dispersive interactions as implemented in vdW-DF and the computed CO_2MOF binding energies and geometries are similar to those reported by Valenzano et al.[96] Figure 4.3 shows that our results are in good agreement with the DFT results. It is important to note that the path shown in Figure 4.3A includes the minimum energy configurations, a feature which is reproduced well by our force field. The detailed force fields for the interactions of CO_2 and N_2 with Mg-MOF-74 are reported in Appendix C.

It is instructive to compare our force field with the Universal force field. In Figures 4.2C and 4.2D we compare the UFF predictions of the total energies on the eight different paths. For the Mg path, we observed that the UFF force field does not allow the CO_2 molecule to approach the Mg atom as close as the MP2 calculations predict. As a consequence, the electrostatic and dispersive interactions are underestimated significantly. The fact that we can incorporate these chemical differences in our force field is essential for a correct description of these systems; otherwise, it would not possible to reproduce the results of the quantum calculations.

Predictions from simulations utilizing new force field

As a first test of our force field we computed the heat of adsorption and compared it with the experimental values obtained by Simmons et al.[132] Dietzel et al.[99] and Mason et al.[100] (Figure 4.4). Our simulations quantitatively reproduce the observed dependence of the heat of adsorption as a function of loading. We predict an inflection at exactly one CO_2 molecule per Mg. The experiments show this inflection at slightly lower loadings (0.8 CO_2 molecule per Mg). In our simulation we assumed a perfect crystalline material in which every Mg atom is activated. As all Mg atoms are equivalent, one would expect this inflection to occur at exactly one CO_2 molecule per Mg. These observations support the conclusion of Dietzel et al.[99] According to their work, not all Mg sites are accessible in the real system. Our simulations, in agreement with the experimental data of Dietzel et al.[99] and Simmons et al.[132] show an increase of the heat of adsorption as a function of the loading. Mason et al.[100] did not report such an increase. They obtained the heat of adsorption from a fitting procedure to a dual-site Langmuir isotherm. This procedure imposes a monotonic decrease of the heat of adsorption as a function of loading. In this study we computed the experimental heat of adsorption directly from our simulations,[131] and hence our results are independent of the interpretation of the isotherms.

In Figure 4.5 we compare the predicted adsorption isotherms with the experimental isotherms for CO_2 and N_2 in Mg-MOF-74.[99,100,132–137] We obtain excellent agreement with

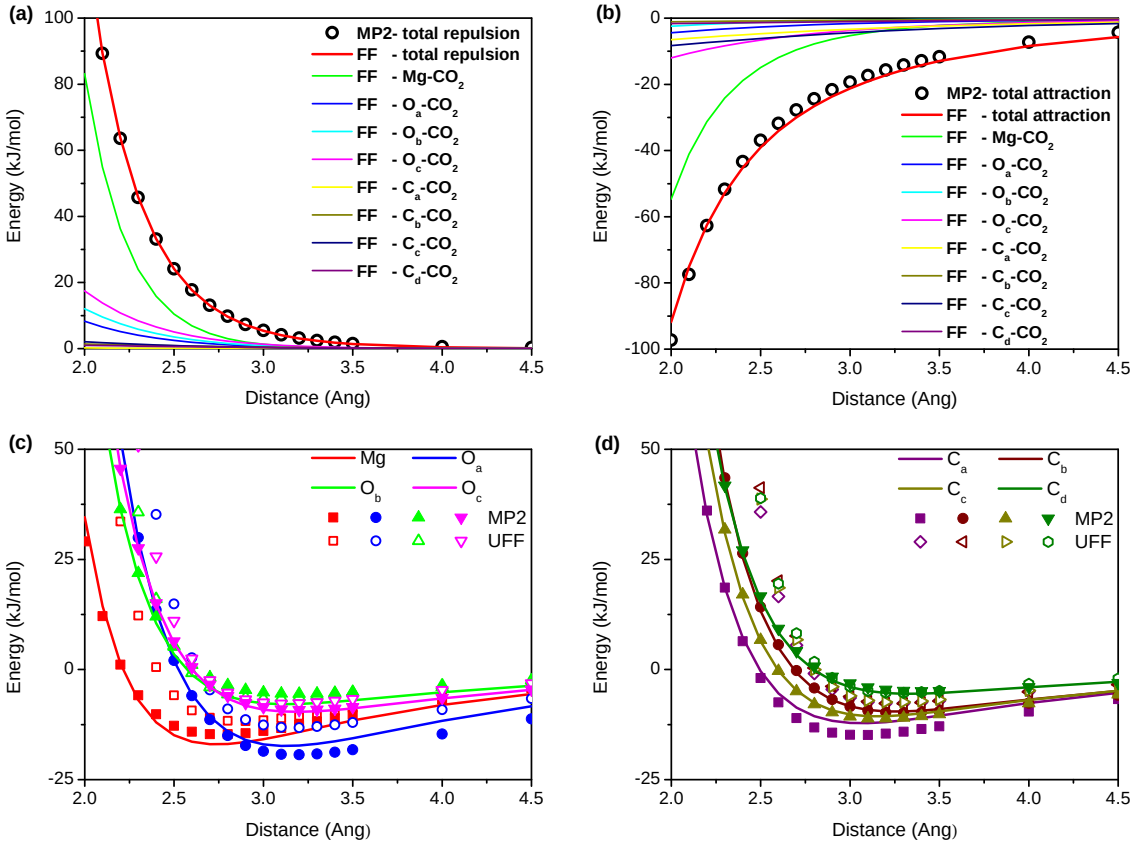

Figure 4.2: Interaction energy comparison of force field with decomposed MP2 and UFF. (a) and (b): NEMO decomposition of the MP2 energies on the Mg path into (a) repulsive and (b) attractive interactions. The black circles are the MP2 results and the solid lines the fitted force fields for the various atoms. The red line gives the contribution of Mg. (c) and (d): Comparison of the MP2 repulsive plus attractive energies for the eight different paths (given by closed symbols) with the results from the force field (solid lines). For comparison, we have added the predictions from the UFF force field (open symbols).

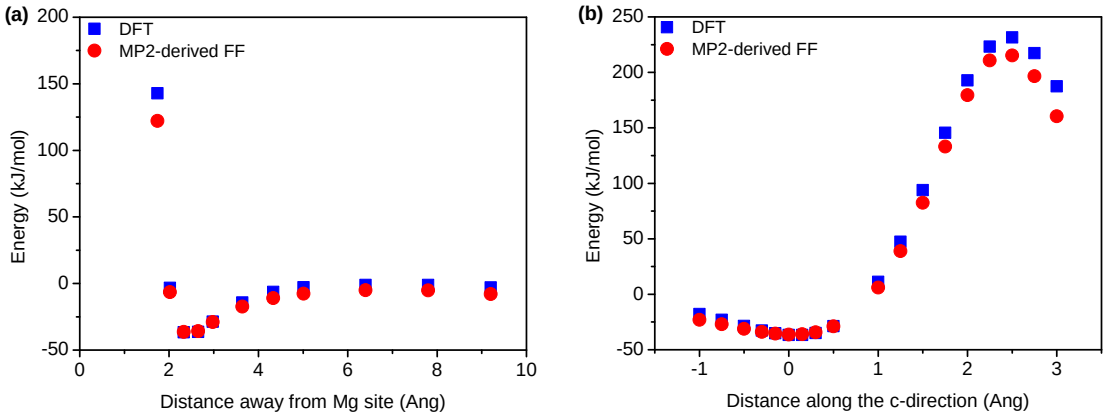

Figure 4.3: Interaction energy comparison of force field with periodic DFT. The MOF-CO_2 interaction energy is plotted along two different paths crossing the minimum energy configuration of CO_2 in Mg-MOF-74. (a) path of CO_2 approaching the open-metal site from the center of the pore, and (b) path of CO_2 approaching the open-metal site in the c-direction. Blue curves are DFT calculations including van der Waals interactions and red curves are obtained from our force field. Both paths are computed in the periodic system.

experimental data, and the agreement is best when we take into account that not all Mg sites are accessible in the experiments. Comparison with the simulation using the UFF force field illustrates the significant improvement in predictions made by our force field. In the Henry regime, the conventional force field underestimates the adsorption by as much as two orders of magnitude. An interesting observation is that we are not able to describe the simulated (and experimental) adsorption isotherms for CO_2 with a dual-site Langmuir isotherm (see figure 4.6). Langmuir isotherms assume that each adsorption site is independent. The heat of adsorption data already shown that CO_2-CO_2 interactions cannot be ignored for the CO_2 binding to the Mg sites and, because of these interactions, it becomes easier to add another CO_2 molecule in the MOF. If we have a loading of approximately 1 CO_2 per 6 Mg, we observe a significant collective effect that makes it easier to add an additional CO_2 molecule adjacent to the ones already adsorbed. Figure 4.6 shows that these relatively small energies (1.6 kJ/mol), provided from the CO_2-CO_2 interactions, essentially enhance the uptake of CO_2 up to 15% at the condition of carbon capture. This suggests that in the design of a carbon capture material one would also like to optimize these collective effects inside the material.

At this point it is instructive to compare our approach with the multi-Langmuir approach developed by Sauer and co-workers.[138] In the multi-Langmuir method, the MP2 energies at the binding sites are directly used to estimate the corresponding adsorption coefficient (or Henry coefficient) of the different adsorption sites and hence the use of force fields is avoided.

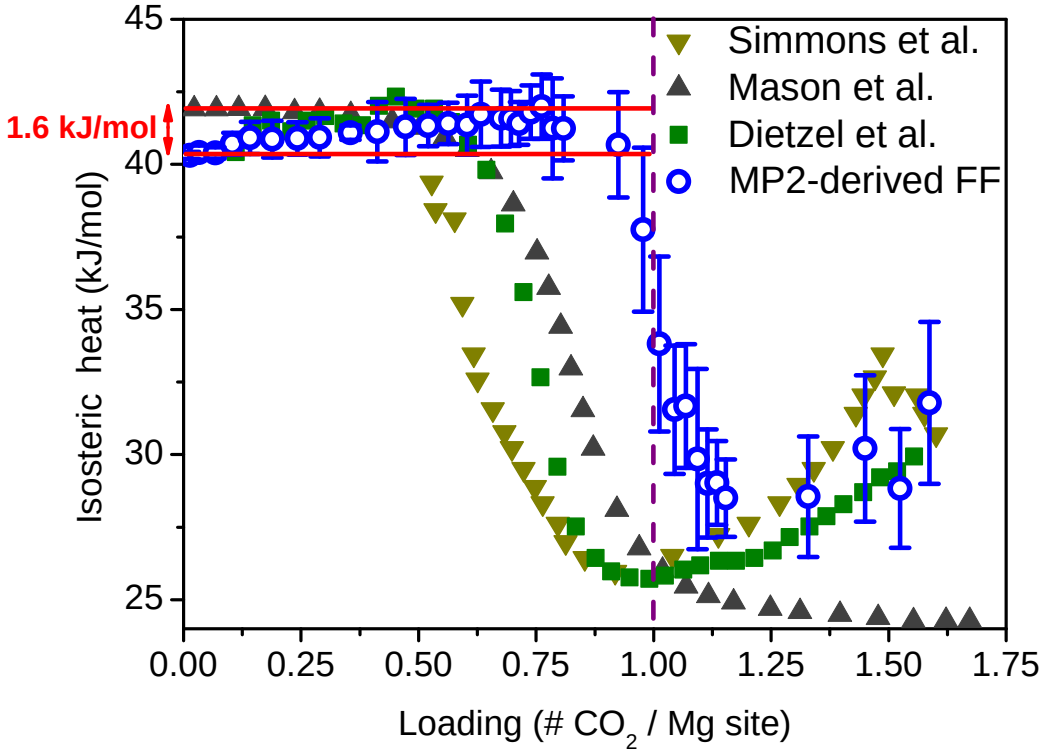

Figure 4.4: Comparison of the experimental and simulated isosteric heats of adsorptions as a function of loading. The loading is plotted as the number of CO_2 per open-metal site. For an ideal material, for which all metal sites are active, the molecular simulations predict (blue symbols) that one CO_2 binds to one open-metal site. The black, green, and olive symbols give the reported experimental data in the literature by Mason et al., Dietzel et al., and Simmons et al., respectively. Red lines indicate the enhancement of CO_2 heat of adsorption due to cooperative effects that has been predicted from the molecular simulations.

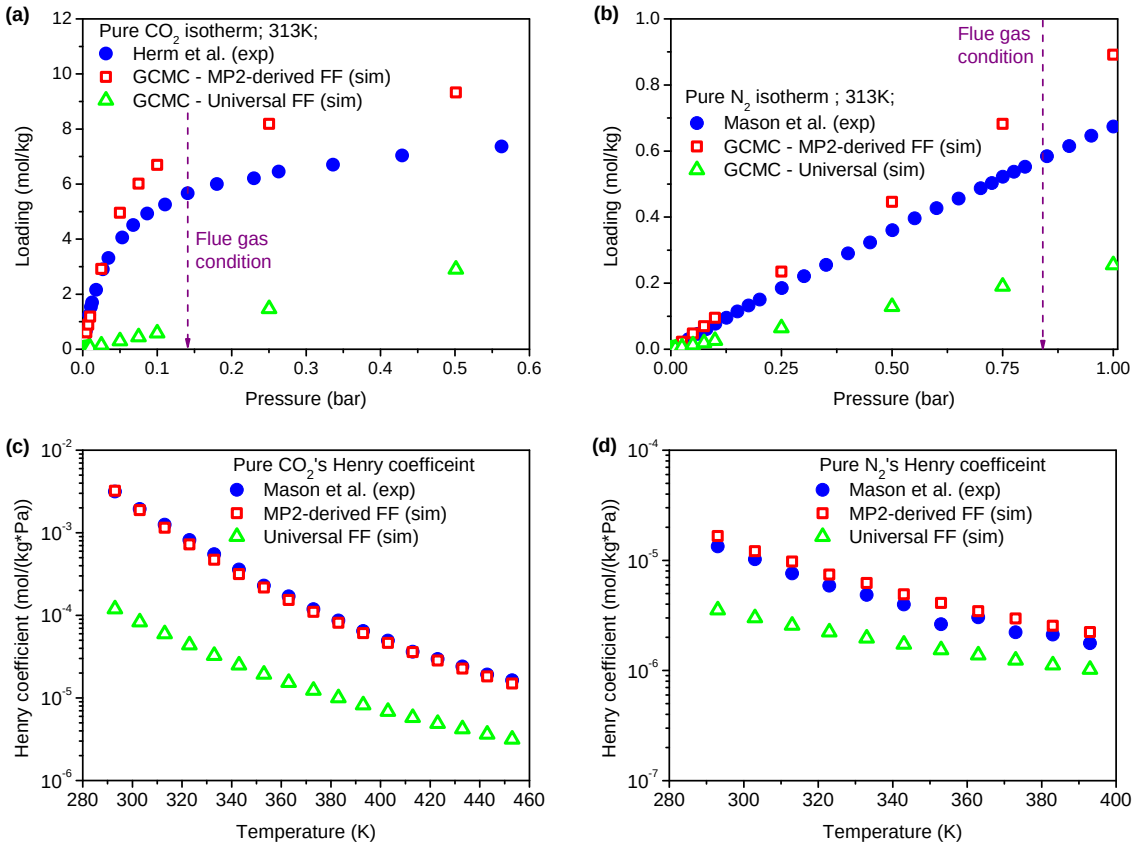

Figure 4.5: Comparison of simulated and experimental adsorption isotherms and Henry coefficients. Experimental and predicted adsorption isotherms are shows for (a) CO_2 and (b) N_2 in Mg-MOF-74. The blue circles are the experimental data of Herm et al. or Mason et al. The open symbols are the simulation results; the green symbols are the results of using the UFF force field and the red symbols are from the present force field. At low pressure the adsorption is linear in the pressure; the proportionality coefficient is defined as the Henry coefficient. This Henry coefficient is shown in the bottom figures as a function of the temperature for (c) CO_2 (d) and N_2.

The multi-Langmuir approach relies on the assumption that the isotherms can be described with a Langmuir equation and a few well-defined binding sites dominate adsorption. As for the adsorption of CO_2 in Mg-MOF-74, the use of a force field is essential to capture the enhancement at low loading and to correctly describe the adsorption at high loading.

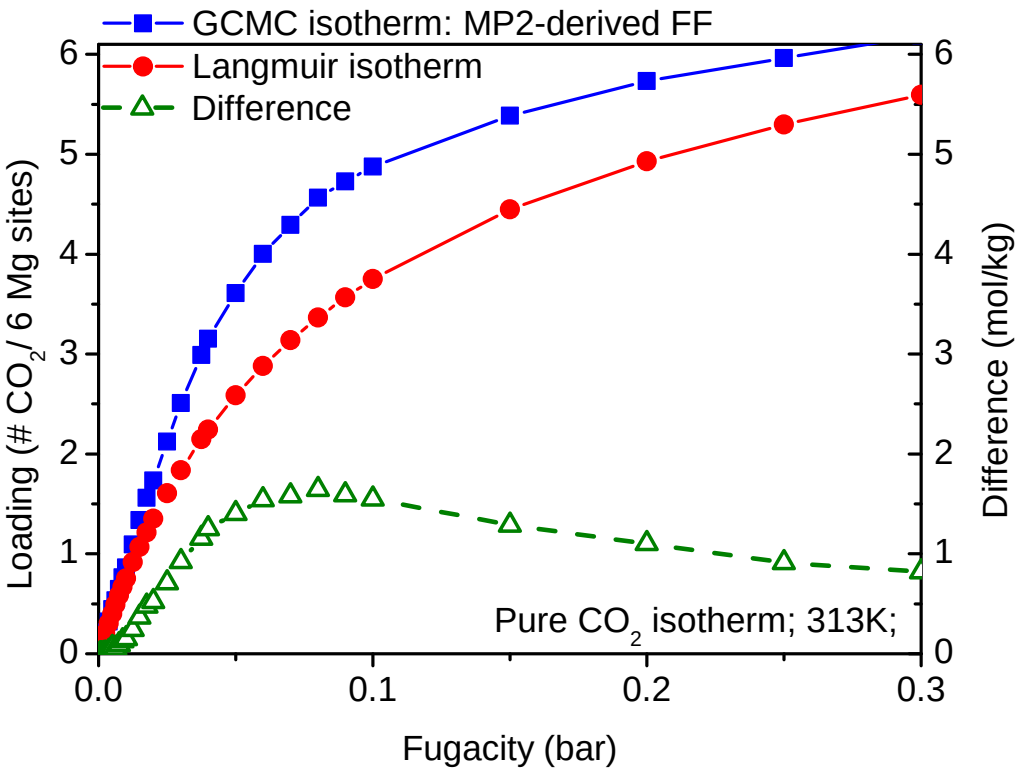

Figure 4.6: Enhancement of the adsorption of CO_2 as a function of loading. In this figure we compare a Langmuir isotherm (red) with the results from GCMC simulations (blue). The parameters of the Langmuir isotherm are obtained from the Henry coefficient from the GCMC simulations and the maximum loading, which is set to one CO_2 per Mg site. The difference between these curves (green) indicates the enhancement induced by the presence of other CO_2 molecules.

Transferability

We should now discuss the transferability of our approach. Recently, McDonald et al.[104] synthesized Mg_2(dobpdc), a material similar to MOF-74, but with an extended linker. Since this linker contains the same chemical groups as MOF-74, we can compute the isotherms for Mg_2(dobpdc) using the force field derived for Mg-MOF-74, only requiring one quantum calculation to provide atomic charges (see Figure 4.7 for atom types and Tables C.1,C.4, and C.6 for charges and parameters). Figure 4.8 shows that the predicted isotherm is in good agreement with the experimental data reported by McDonald et al.[104] It is interesting to see whether similar to MOF-74, this material also has an enhancement of the adsorption

because of the CO_2-CO_2 interactions. Figure 4.9 clearly illustrates that the collective effect in this extended system is far less pronounced. Because the linkers are longer, CO_2-CO_2 interactions are less important in this material and we observe a normal Langmuir behavior.

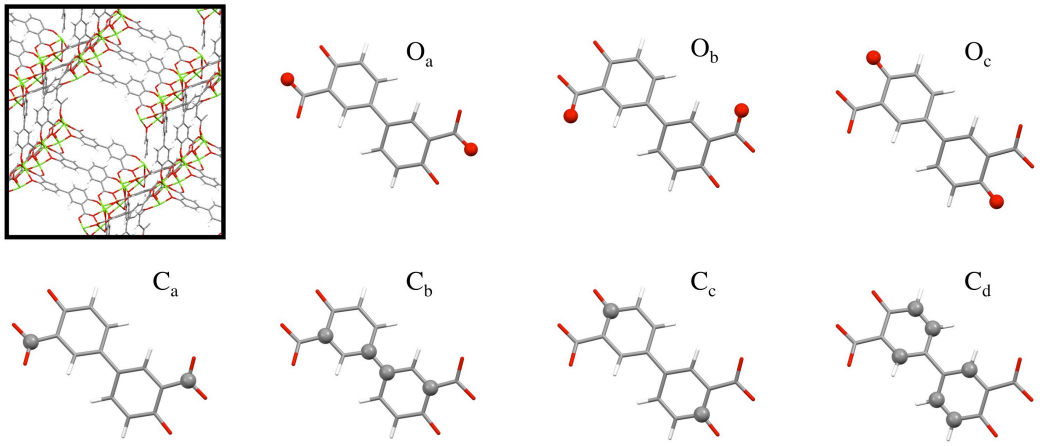

Figure 4.7: Image of Mg_2(dobpdc) (top left) and force field atom types. The three oxygen atom-types and four carbon atom-types are shown, along with the same naming scheme as for Mg-MOF-74.

We also investigated the effect of changing the metal in MOF-74. By following the same procedure described above for Zn-MOF-74, we developed parameters for the Zn-CO_2 interactions, but kept all other interactions the same as in Mg-MOF-74. This result is a further confirmation that our approach is transferable. In Figure 4.10 we compare the predicted isotherms for Zn-MOF-74 with the corresponding isotherm for Mg-MOF-74. Unfortunately, Zn-MOF-74 is much more difficult to activate and hence there are not definitive experimental results against which we can compare our predictions. Parameters and charges for Zn-MOF-74 are given in Tables C.2 and C.7.

Finally, we employed our approach to study CO_2 in MOF-5, which does not have open-metal sites. This required the development of new cluster geometries, shown in Figures C.9-C.11 in Appendix C. The structure and atom types are shown in Figure 4.11 and the charges and force field parameters are in Tables C.3 and C.8. Figure 4.12 shows that the CO_2 simulated isotherm is in excellent agreement with the experimental one reported by Walton et al.[58] This set of results confirms that our methodology is applicable to different types of structures.

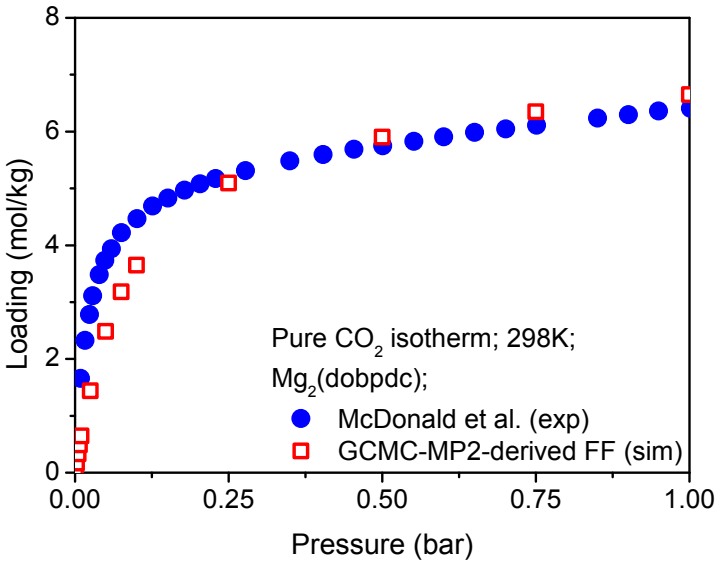

Figure 4.8: Adsorption isotherms of CO_2 in Mg_2(dobpdc).Closed and open symbols to represent the experimental and simulation adsorption isotherms, respectively. Mg_2(dobpdc), is a material with an extended linker using the same atom types as in the Mg-MOF-74 material.

4.4 Summary

In summary, a novel methodology that yields accurate force fields for CO_2 and N_2 in an open site MOF from high-level quantum chemical calculations has been developed. These force fields take into account the subtle changes in the chemical environment induced by the presence of open-metal sites in metal organic frameworks. Our new method allowed us to reproduce the experimental adsorption isotherms for both CO_2 and N_2 in Mg-MOF-74. We have also shown that our methodology is transferable to systems containing different metals, linkers, and different topologies. The same approach will be used to predict properties of open-site MOFs that have not yet been synthesized.

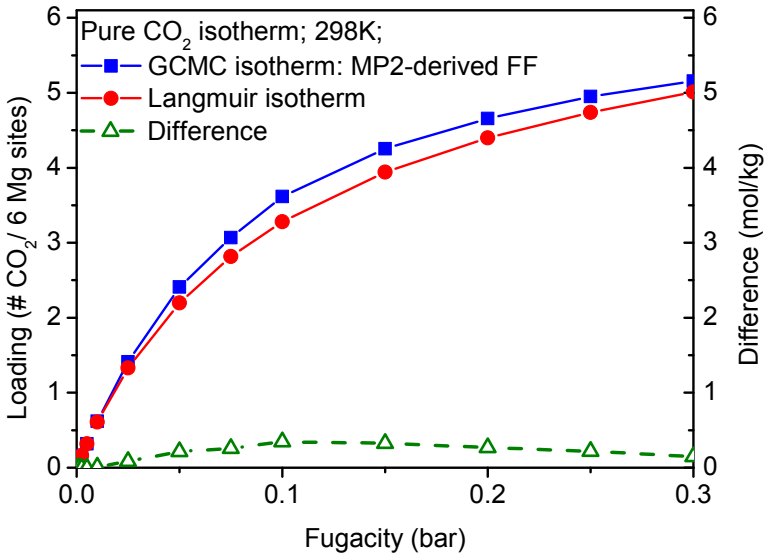

Figure 4.9: Enhancement of the adsorptions of CO_2 as a function of loading in extended Mg-MOF-74. The comparison between a Langmuir isotherm (red) with the results from GCMC simulations (blue). The parameters of the Langmuir isotherm are obtained from the Henry coefficient from the GCMC simulations and the maximum loading, which is set to one CO_2 per Mg site. The difference between these curves (green) indicates the enhancement induced by the presence of other CO_2 molecules.

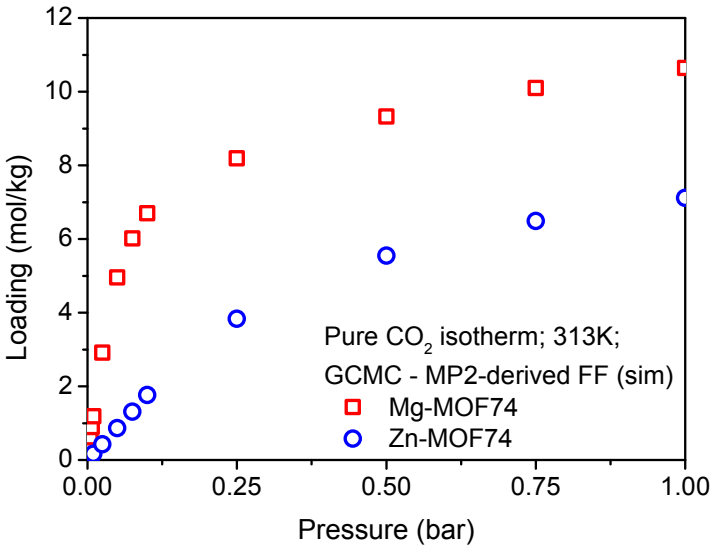

Figure 4.10: Adsorption isotherms of CO_2 in additional Zn-MOF-74. The parameters all atoms except Zn in Zn-MOF-74 are transferred directly from our force field for Mg-MOF-74.

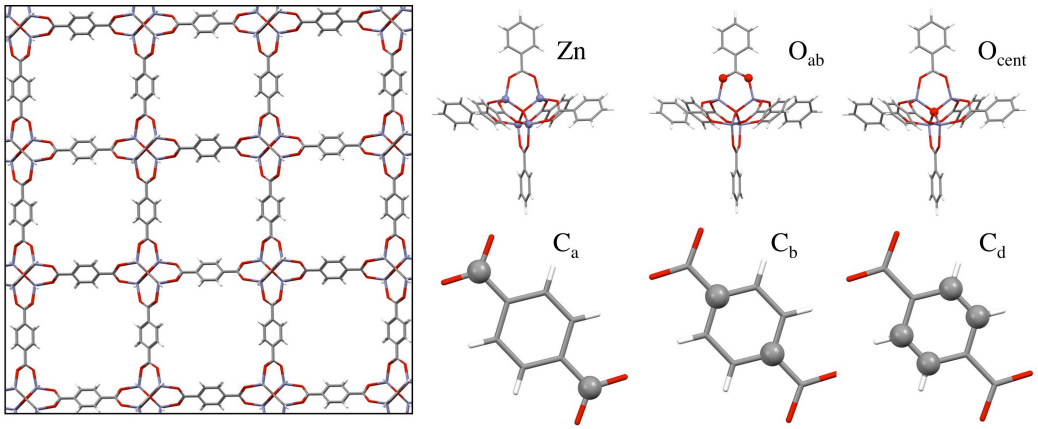

Figure 4.11: Image of MOF-5 structure (left) and the 6 force field atom types (excluding H) along with the naming scheme adopted here.

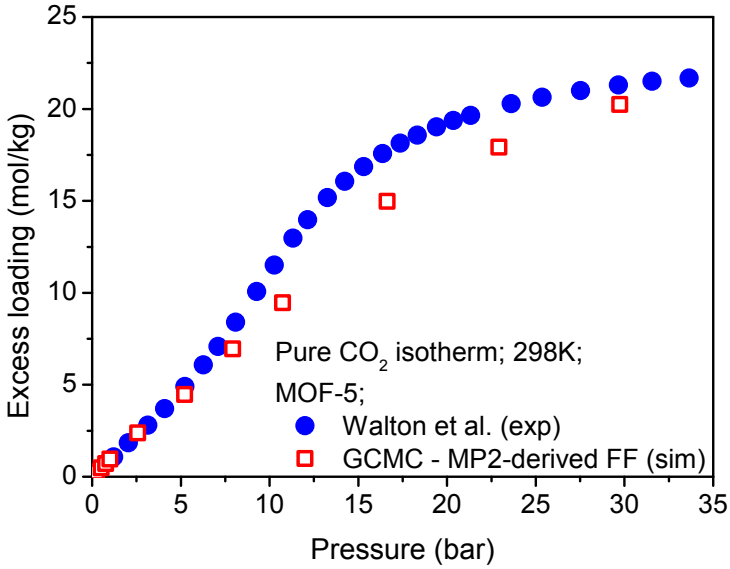

Figure 4.12: Adsorption isotherms of CO_2 in MOF-5, a material that does not have open metal sites. In these figures the we use closed and open symbols to represent the experimental and simulation adsorption isotherms, respectively.

Chapter 5

Molecular simulation study of the competitive adsorption of H2O and CO2 in zeolite 13X

The presence of H_2O in post-combustion gas streams is an important technical issue for deploying CO_2-selective adsorbents. Due to its permanent dipole, H_2O could potentially interact strongly with materials where the selectivity for CO_2 is a consequence of its quadrupole interacting with charges in the material. This chapter investigates the issue of H_2O adsorption in 13X, a popular zeolite for CO_2 capture processes. Adsorbed H_2O reduces the capacity of these materials for adsorbing CO_2. A rearrangement of extra-framework sodium cations may be responsible for the shape of the H_2O isotherms.

5.1 Background

A variety of processes have been considered to replace amine scrubbing as the preferred technology, including membranes, advanced solvents, and adsorption. Recent work investigating materials for separation of CO_2 from N_2 via adsorption processes at relatively low pressures has shown that there are a variety of materials which could potentially provide acceptable performance.[11,16] However, most of these studies have not focused on the performance of these materials with gas mixtures that contain water. Post-combustion gas streams contain relatively large quantities of water (around 5 to 15 vol.%),[139] and streams that have been subjected to desulfurization processes will be saturated with water at the process temperature. Studying the influence of water on CO_2 adsorption is important because it could potentially reduce the capability of these materials to selectively adsorb CO_2 efficiently enough for a practical process. For example, the high selectivity for CO_2 over N_2 of cation-containing zeolites and metal-organic frameworks (MOFs) with open-metal sites is attributed to strong interactions with the cations or metal sites in these materials, respectively.[51,53,69] The presence of these strongly interacting cation sites also makes zeolites like 13X good adsorbents

for water as well. In fact, 13X is marketed as a desiccant in some contexts and has been studied as a medium for storing solar thermal energy (with water as the working fluid).[140,141] Because most streams where CO_2 would be removed also contain some amount of water, it is important to study the effect that the presence of water has on the capacity of the material to adsorb CO_2.

Due to it's high selectivity and ready availability on the ton scale, zeolite 13X (NaFAU) has been used as a reference material in a variety of process design studies for carbon dioxide removal.[142–144] Zeolites are porous aluminosilicate materials that have been used extensively in industrial processes as adsorbents and as catalysts of catalyst supports. The small pores of these materials are on the order a one to a few molecular diameters, and depending on the topology, can potentially sieve molecules based on size. The presence of aluminum gives these frameworks a net negative charge that is compensated by a cation that resides outside the aluminum-silicon-oxygen bond networks and instead occupies some of the pore space. Due to this relatively weak coordination by the framework, these cations can be exchanged using salt solutions to customize the pore diameter and chemical affinity of a particular zeolite. These cations also provide a good adsorption site for the polar water molecule. Recent work has shown that these materials selectively adsorb CO_2 in preference to N_2 by a factor of about 100 to 300, depending on the cation, at the conditions relevant for post-combustion CO_2 capture processes.[69]

Wang and LeVan studied both the pure component and mixture isotherms of water and CO_2 on commercial 13X and 5A samples and noted that while small amounts of water can reduce the CO_2 capacity slightly, once the material nears saturation with water, the CO_2 capacity is an order of magnitude lower than the dry materials.[71,145] Brandani and Ruthven studied the effect of water on CO_2 and propane adsorption at different loadings of water on low-silica forms of X and CaX and correlated the water loading with an exponential decrease in the Henry's law coefficient for CO_2.[146] Ferreira et al. measured breakthrough curves for CO_2 and H_2O on different commercial 13X zeolites, as well as activated silica and alumina and concluded that silica and alumina were superior adsorbents for dehydrating gas streams because the reversible capacity on these materials was larger.[147] Lee et al. studied X-type zeolites with different cations exchanged and showed that after adsorbing dilute CO_2 from air there is a substantial reduction in the cyclic capacity of the materials in the absence of a high temperature regeneration step.[148]

There have been a variety of simulations performed on water in aluminosilicate zeolites. Castillo et al. compared different H_2O models in pure-silica zeolites and showed that the predicted isotherms were sensitive to the partial charges and crystal structure of the zeolite framework.[149] Lee et al. and Faux et al. performed molecular dynamics (MD) simulations of water and sodium molecules in zeolite 4A using a fixed and flexible zeolite framework, respectively.[150,151] Jaramillo and Chandross and Wu et al. simulated H_2O adsorption in zeolite 4A (NaLTA) and showed that the SPC/E and TIP3P water models gave similar adsorption isotherms. Beauvais et al. simulated water in NaX and NaY (NaFAU at $\tilde{2}.4$ and $\tilde{1}.24$ Si/Al, respectively) and observed that since water coordinates the cations, it can cause a rearrangement of the cations from their preferred sites in the dehydrated structure.[152] Other

work by Bellat et al. demonstrated that there is a small amount of hysteresis at relatively low pressures in NaY, which they attribute to rearrangement of cations between the supercage and sodalite cages of FAU as water adsorbs.[153] DiLella et al. studied water adsorption and desorption in different NaFAUs and showed that a model that models the Si/Al ratio through changes in T-atom and framework oxygen partial charges generally agreed with experimental data.[154] Hutson et al. performed both simulations and experiments on LiLSX (low-silica X) and showed that even a small amount of adsorbed water caused a precipitous drop in the N_2 adsorption capacity that required regeneration above 500 K to recover.[155] Boddenburg et al. performed experiments and derived a statistical mechanical isotherm model and proposed that near saturation some Na cations would be coordinated by up to 6 water molecules.[156]

In this work, we aim to study the adsorption of water and water/CO_2 mixtures in hydrophilic zeolites. Grand canonical Monte Carlo (GCMC) simulations were used to predict adsorption isotherms and heats of adsorption for H_2O CO_2 and H_2OCO_2 mixtures. These results indicate that CO_2 has a negligible effect on the co-adsorption of H_2O. Canonical Monte Carlo (CMC) simulations were performed to study the average structure of sodium cations, H_2O and CO_2 molecules at different loadings. Once saturated with water, these materials adsorb a much smaller amount CO_2 and although this adsorption appears reversible, it dramatically reduces the utility of these materials for post-combustion capture.

5.2 Methods

Grand canonical Monte Carlo simulations were preformed to estimate the loading of pure components and mixtures at different temperatures.[22] Simulations were carried out on a model of zeolite 13X, which has the FAU topology, based on the structure reported by D. H. Olson.[157] Aluminum atoms were placed randomly at the T2 position to give the framework 86 Al per unit cell, or a Si/Al ratio of about 1.24. Figure 5.1 shows two views of the 13X framework, viewed through the 12-ring connecting the supercages (along $< 111 >$ direction). Figure 5.1A shows the atomic structure of the material. The spheres in the pore space are the extra-framework sodium atoms, taken from one configuration of a Monte Carlo simulation. For reference, Figure 5.1B shows a simplified view of the FAU topology. The bonds in the Figure 5.1B connect the T-atom positions. The red circle in the center shows the center of one supercage, which is connected to 4 other supercages by 12-rings of T-atoms. The blue circles indicate the sodalite or β-cages of the material. In these simulations, sodium and H_2O are allowed to enter both the supercages and sodalite cages, but CO_2 only can access the supercages.

Sodium atoms were placed randomly and equilibrated using canonical Monte Carlo moves. During GCMC simulations, sodium atoms were also allowed to move. Adsorbate molecules were allowed to make either translation, rotation, swap, and regrowth moves. Swap moves involve the insertion or deletion of a single molecule to or from the simulation box. The regrowth move involves taking an existing molecule in the simulation and placing it at another location in the box at random. Interactions between the framework, cations, and ad-

sorbed molecules were modeled using a sum of a 12-6 Lennard-Jones (LJ) term to represent dispersive interactions and a Coulombic term to represent electrostatic interactions. The Ewald summation technique as used to compute the electrostatic contribution. Parameters and partial atomic charges for the zeolite and cations interacting with CO_2 were taken from the force field developed by García-Sánchez et al.[66] Water-water interactions were modeled using the SPC/E model[158] and water-framework and water-sodium interactions were parameterized by computing the ratio of the LJ parameters for the CO_2-framework and CO_2-sodium interactions relative to the CO_2-CO_2 interaction parameters. The SPC/E water parameters were then scale by the average ratio for the CO_2 molecule, and the parameters are list in Table 5.1. Although the sigma parameters for the water-framework and water-sodium interactions are relatively large, this force field appears to reproduce the adsorption isotherm for H_2O in 13X (see below). However, these parameters may not be transferrable and a more detailed analysis of the force field was out of the scope of this work.

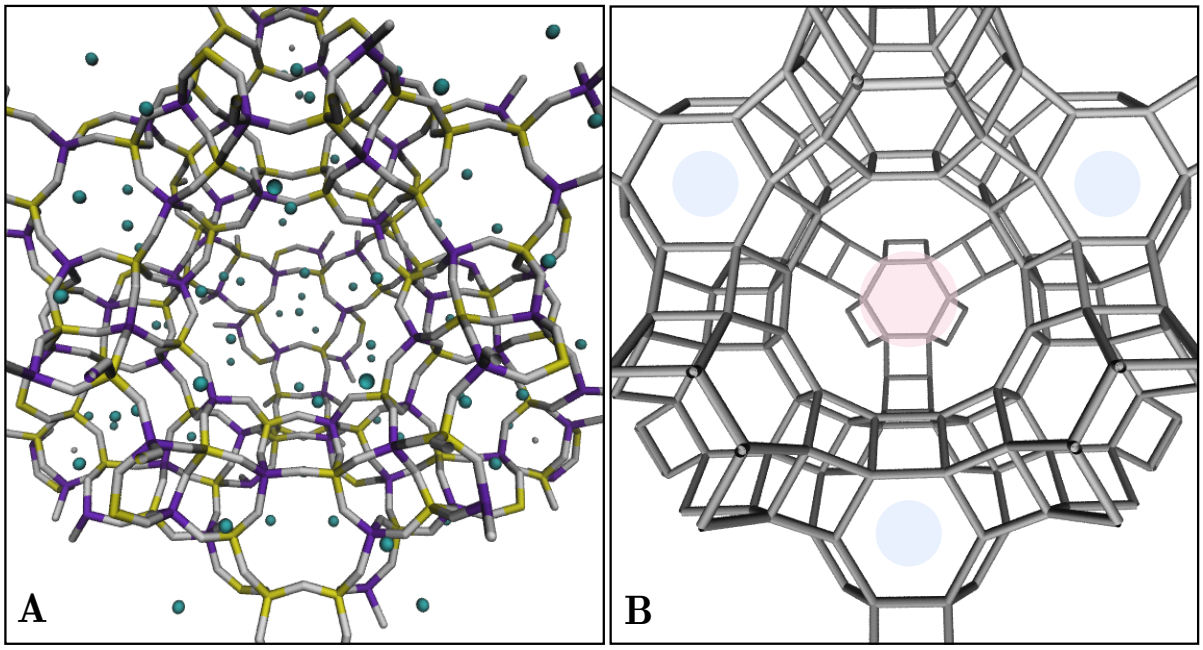

Figure 5.1: Views of the structure of 13X. (A) A view of the unit cell of 13X (NaFAU) with sodium positions taken from one configuration of a Monte Carlo simulation. Oxygen atoms are gray, silicon are yellow, aluminum are violet, and sodiums are cyan. (B) Schematic of the FAU topology showing the connection between T-atom positions. The blue circles indicate the sodalite cages and red indicates the center of the supercage.

Atom pair	ϵ/k_b K	σ $\AA$
$O_{zeolite}$-O_{water}	564.88	3.361
Na-O_{water}	85.15	3.723

Table 5.1: Parameters for water-zeolite interactions used in this work. They are based on scaling the SPC/E model parameters by the average ratio between the CO_2-zeolite and CO_2-CO_2 interactions reported by García-Sánchez et al.[66]

5.3 Results and Discussion

We performed GCMC simulations of water at different fugacities and temperatures adsorbing both by itself and simultaneously with CO_2 in zeolite 13X, a prototypical aluminosilicate zeolite. Figure 5.2 compares GCMC simulations of water adsorbing in zeolite 13X with experimental data reported in Wang and LeVan.[145] While there appears good agreement between simulations and experiment at all temperatures, the experiments were conducted on pelletized zeolite samples, so correcting for the mass of the particles composed of binder material would likely shift the experimental loadings to slightly higher values. However, the slopes of the isotherm should not change substantially and they appear to agree quite well. The isotherms could be classified as Type V,[159] with a relatively linear region at very low pressures, a steep elbow over a narrow intermediate pressure range, and a plateau region where the rate of loading increase with increasing pressure diminishes. Our simulations show that the water partial pressure has to be well below 1 Pa to be in the Henry's law regime. From a practical point of view, it is useful to consider the predicted loadings when a gas stream would be saturated with water. Table 5.2 shows the saturation vapor pressures for water at the temperatures where the isotherm was simulated.[160] For a post-combustion process around 323 K, the partial pressure is about 12 kPa, which would place the equilibrium loading within the plateau regime.

An interesting question is what causes the shape of the H_2O isotherms. We observed that the elbow region of the isotherm is defined by a sharp rise in the loading of water over a narrow range of pressures. To study the structure of the adsorbed molecules, we performed NVT Monte Carlo simulations and recorded the positions of atoms at regular intervals. Histograms were calculated by computing the distance between a particular atom and the closest atom of another type and computing the frequency of a range of distances over many configurations. Figure 5.3 shows histograms of distances between sodiums and the oxygen of H_2O molecules at different total loadings of H_2O (expressed as molecules per unit cell). The average distance is about 3.5 Å and the peak shifts to slightly smaller distances as the H_2O loading increases. The average distance is larger than the 2.76 Å distance reported for the coordination of sodium cations by water in aqueous solution,[161] and the discrepancy between these values is almost certainly due to the relatively large value of σ used for the Na-H_2O interaction in this work (see Table 5.1). Figure 5.4 shows the

histogram of nearest distances between the oxygen and hydrogen atoms on different water molecules. The taller peak at shorter distances (1.7-1.9 Å) represents the interaction of hydrogen bonded molecules, while the smaller peak at (3.1-3.3 Å) represents another water molecule coordinated to the same sodium, but not hydrogen bonded. At the lowest water loading, there is a long tail that extends across the unit cell, representing the fact that the waters are likely to coordinate isolated sodium atoms. As the loading of water increases, the density at higher distances disappears and the shorter peak becomes smaller as the hydrogen-bond peak increases. As the pore fills up with water, it is able to form as complete as a hydrogen bond network as possible. Due to the density of sodiums at 86 per unit cell, water molecules can both coordinate a sodium cation and hydrogen bond with another water. This explains the saturation of these materials with water at relatively low fugacities, there are many sites where the water molecule can be stabilized. However, this does not appear to explain the elbow, as water molecules can incrementally coordinate more sodium atoms cations or hydrogen bond with other waters, even up to high loading.

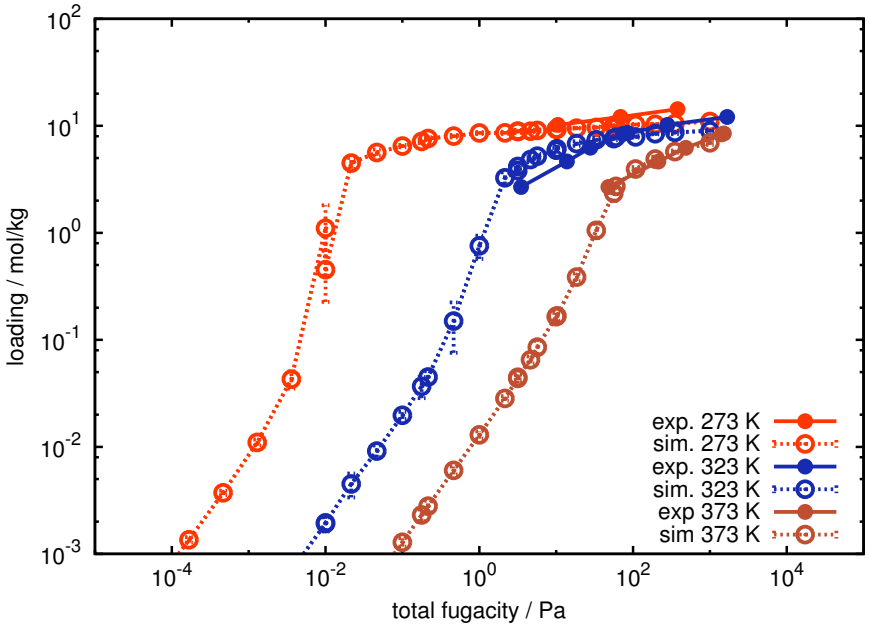

Figure 5.2: Pure component isotherms for H_2O adsorbing in zeolite 13X at 273, 323, and 373 K. Open symbols are the results of GCMC simulations and the filled symbols are from the experimental data reported by Wang and LeVan.[145]

A related system where Type V isotherms are observed is the adsorption of water on porous carbons. The shape of the isotherm is attributed to a balance between adsorption at hydrophilic functional groups, which occurs at low pressures, and adsorption of water clusters in the hydrophobic micropores.[162–164] The elbow in the isotherms for these materials reflects the formation of sufficiently large clusters that water-water interactions are the dominate

$T\ (K)$	$P_{vap}\ (kPa)$
273	3.14
323	12.25
373	100.78

Table 5.2: Saturation vapor pressure of water from the Antoine equation.[160]

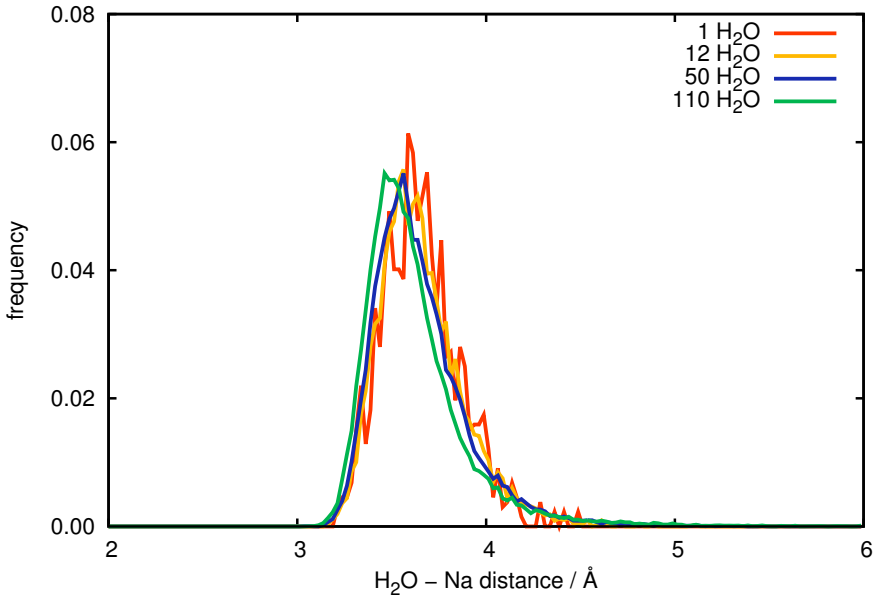

Figure 5.3: Histogram of nearest-neighbor distances for water and sodium cations in 13X at 323K and different loadings of water. The distance was taken as the oxygen cation distance between each water molecule and it's nearest sodium cation.

interactions and can stabilize water in hydrophobic regions. In 13X, however, water interacts strongly with the sodium cations and does not require hydrogen bonding to access all parts of the material. Hydrogen bonding takes place at relatively low water loadings (see Figure 5.4). Although the adsorption of water is stabilized by the ability to form a hydrogen bond network, water is still interacting strongly with the cations in the zeolite pores. Figure 5.6 shows the distribution of nearest distances between sodium cations and the aluminum in the framework at different water loadings and 323 K. At low water loading, there is a single peak, indicating that the sodium tends to stay close to the aluminum sites, as expected, since these represent the concentration of negative charge in the framework that the cations are balancing. At intermediate water loading, the height of the peaks is smaller and there is a longer tail in the distribution, which is due to the fact that water can stabilize sodium farther away from the aluminum sites. At the highest water loading, a small second peak appears

centered about 7.4 Å, showing how some of the sodium atoms can be "dissolved" from the surface of the zeolite pore and can be completely coordinated by H_2O in the pore. Figure 5.5 compares the adsorption and desorption branches of water adsorption in 13X. These were simulated via GCMC by taking the final configuration of a simulation at a particular fugacity as the starting configuration for a new simulation at 95% of the previous fugacity. As water desorbs from the structure, the sodium could then be stabilized by the pore walls again, which may be a reason that hysteresis during desorption from high loading was not observed.

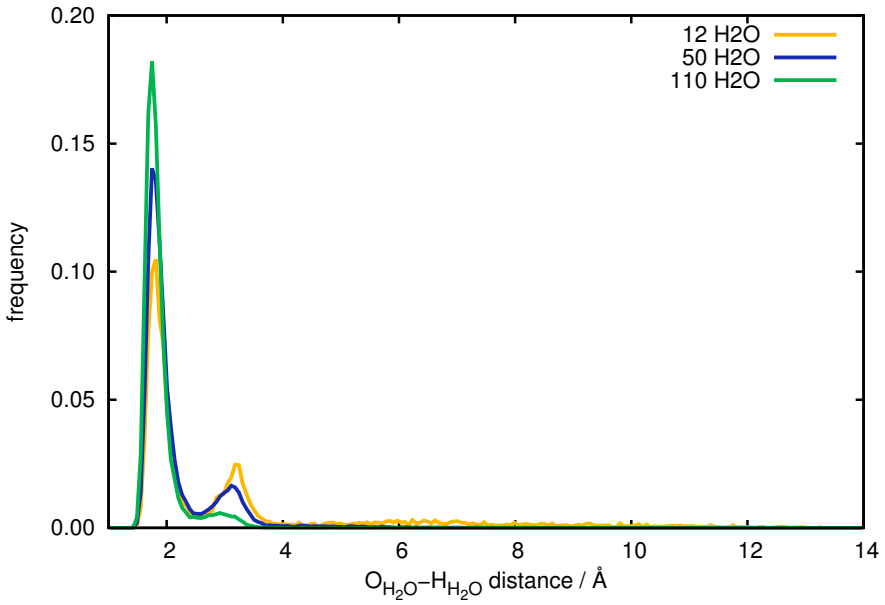

Figure 5.4: Histograms of nearest-neighbor distances between water oxygen atoms and hydrogen atoms on different molecules. The distance was calculated for each proton to the nearest oxygen on another molecule.

GCMC simulations of pure CO_2 adsorbing in zeolite 13X at 273, 323, and 373 K are shown in Figure 5.7. Additional simulations were performed in this work using the NVT ensemble at several loadings of CO_2. Figure 5.8 shows histograms of the distribution of Na-O_{CO_2} distances at different total loadings of CO_2 (in molecules per unit cell) at 323 K. As the loading of CO_2 increases, the shape of the distribution stays essentially the same, and the peak value shifts to slightly lower distances as a larger loading of CO_2 forces the molecules together. The distributions decay rapidly, likely due to the favorable interaction between these atoms and the high density of Na atoms, hence CO_2 cannot find a volume to adsorb in that isolates it from Na. Figure 5.10 shows the distributions of different O-C distances between different CO_2 molecules. At low loadings, the CO_2 molecules can occupy distant parts of the unit cell, yielding two broad peaks. As the loading increases, the distance

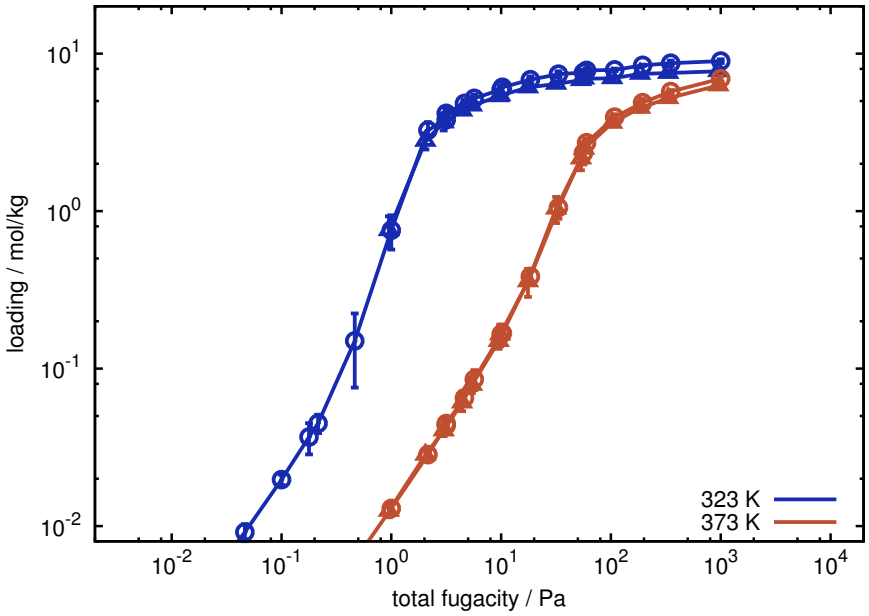

Figure 5.5: Comparison of adsorption and desorption isotherms for H_2O in zeolite 13X at 323 and 373 K predicted by GCMC. The close agreement between the branches indicate there is little or no hysteresis in the water isotherm, due to the stabilization of water by the extra-framework sodium cations.

between CO_2 molecule decreases as the CO_2 fill the available volume. Figure 5.9 shows histograms of the distances between sodium and aluminum atoms in the framework in the presence of different loadings of CO_2. The distributions are essentially the same for all loadings of CO_2. Compared to H_2O (see Fig. 5.6), CO_2 does not influence the positions of sodium atoms, owing to the relatively weaker interactions between CO_2 and sodium.

Figure 5.11 shows the H_2O and CO_2 isotherms for 1% mixture of H_2O in CO_2 at 323 K and 373 K. Below the elbow of the isotherm, the two components appear to adsorb independently. Given that the abscissa plots the total fugacity, the partial fugacity of water is on the order of 100 times lower than the CO_2 fugacity. However, due to the strong interaction of water with this material, it adsorbs close to it's pure component loadings. The inflection point in the H_2O isotherm comes around 100 Pa at 323 K and 3400 Pa at 373 K, which would correspond to water partial fugacities of about 1 Pa and 34 Pa, respectively. Once the water isotherms pass the inflection point and enter the plateau regime, the corresponding CO_2 isotherms pass through a maximum and begin to decrease even as the total fugacity continues to increase. At the flue gas conditions, the partial pressure of CO_2 will be about 17 kPa, while H_2O will be about 5 kPa. With these partial fugacities, water will like be near its saturation loading, and the CO_2 loading will be reduced by an order of magnitude.

To improve sampling of the CO_2 isotherms, we performed simulations where CO_2 was

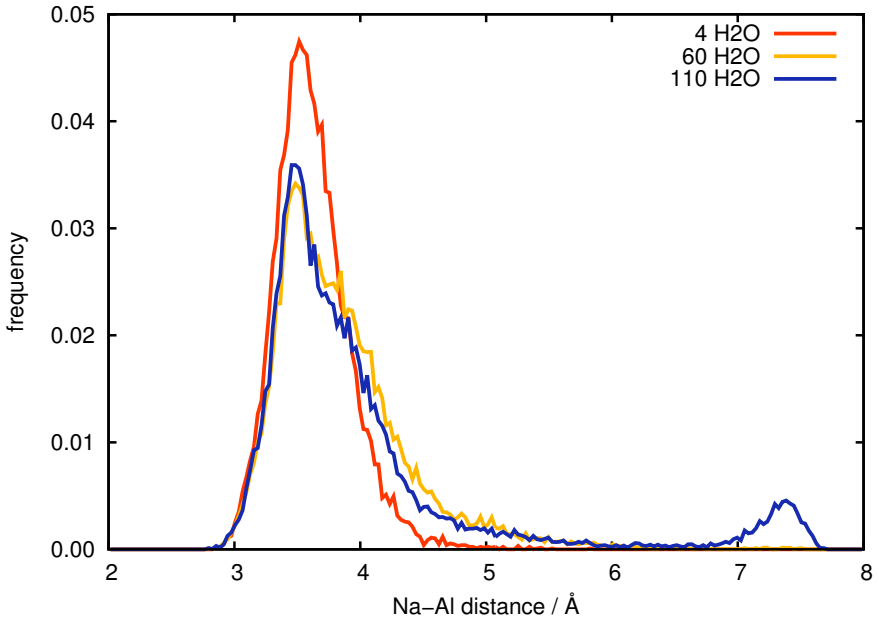

Figure 5.6: Histograms of sodium-aluminum distances at different H_2O loadings at 323 K.

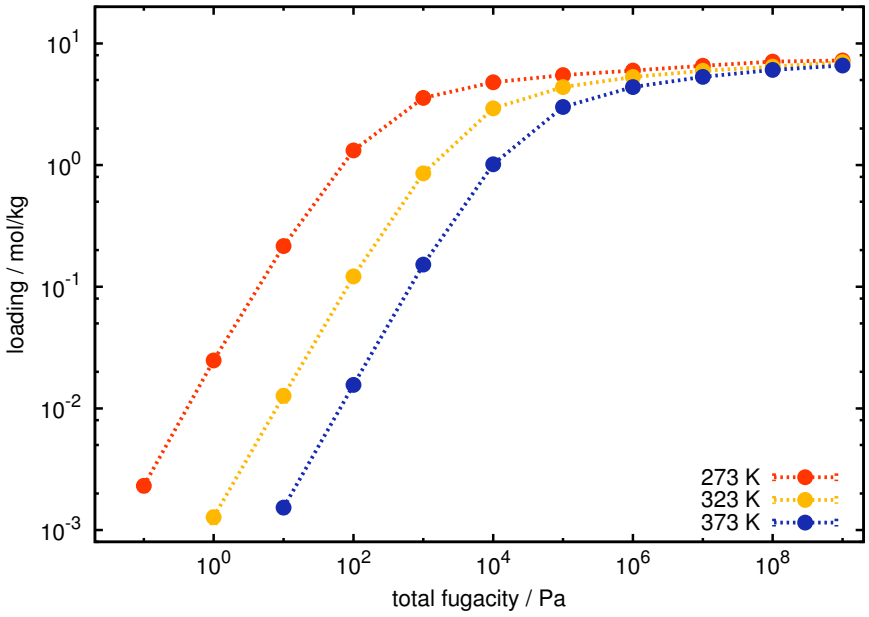

Figure 5.7: Pure component isotherms of CO_2 in 13X.

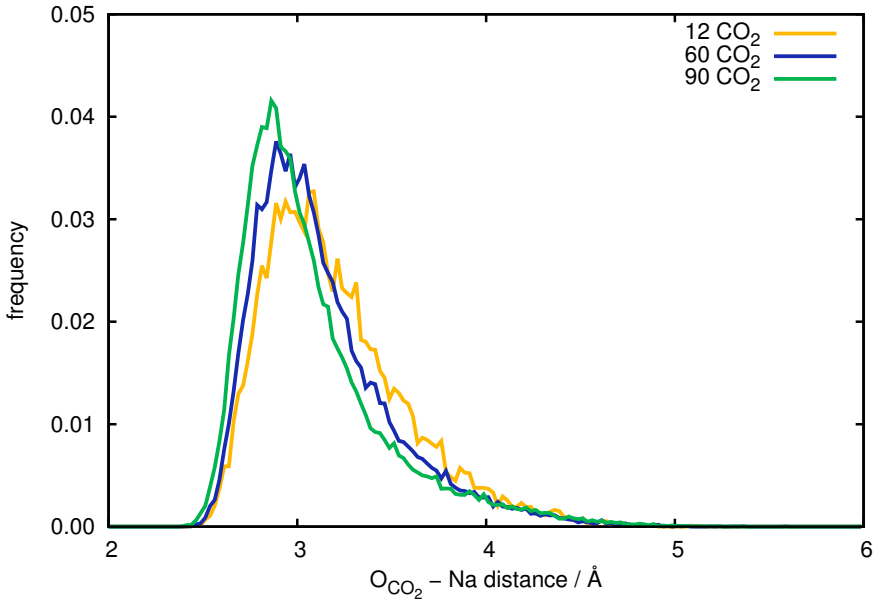

Figure 5.8: Histogram of Na-O_{CO_2} distances in zeolite 13X at 323K.

treated with GCMC moves and H_2O was treated with CNC moves at different constant loadings of water. Figure 5.12 shows the adsorption isotherms for CO_2 at different total water loadings at 323 K. The dashed line indicates the pure isotherm without water present. As expected, increasing the water loading reduces the equilibrium loading of CO_2 at all pressures. Water interactions more favorably with the sodium cations than CO_2 due to its molecular dipole. The formation of a hydrogen bond network will also tend to exclude CO_2 since it can at best act as a weak donor in the network and would be easily replaced by another water molecule.

To more effectively study the structure of the adsorbed solution of CO_2 and H_2O NVT simulations were performed at different number of CO_2 and H_2O molecules. Figure 5.13 shows the distribution of Na-O_{CO_2} distances at different H_2O loadings. The CO_2 loading was fixed at 8 molecules per unit cell. As with the pure CO_2 case, the average distance between Na and oxygen on CO_2 decreases. At the highest water loading, the most likely distance is smaller (2.8 Å vs. 3 Å) than the pure CO_2 case, even at the highest loading. As the water hydrogen bonding network becomes more extensive, the it is more favorable to force the CO_2 molecule closer to the Na cations than to disrupt the network. Figure 5.14 shows the distribution of O-H distances between different water molecules as the water loading increases with 8 CO_2 molecules per unit cell. As with the pure H_2O simulations (see Fig. 5.4), it becomes more likely to find the molecules within hydrogen bond distance, and this does not appear to be disrupted by the presence of CO_2 molecules.

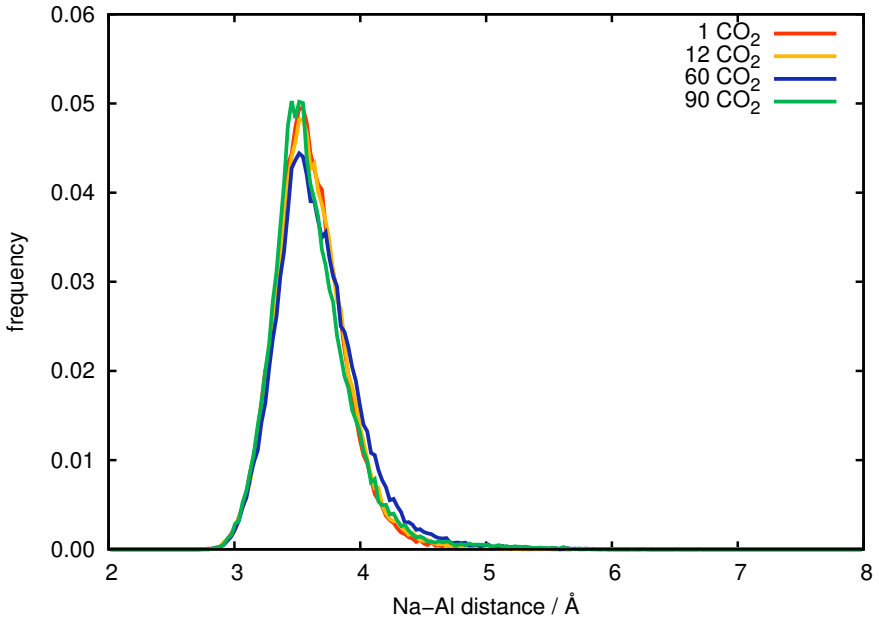

Figure 5.9: Histograms of minimum sodium-aluminum distances at 323 K and different loadings of CO_2.

5.4 Summary

We have performed a molecular simulation study of water and CO_2 adsorption in zeolite 13X, a prototypical alumniosilicate zeolite. Our model is able to reproduce the trends in experimental isotherms for water at different temperatures. When a mixture of H_2O and CO_2 adsorbs, H_2O dominates and adsorbs near its pure component isotherm, which dramatically reduces the available adsorption sites for CO_2. H_2O tends to form as extensive a hydrogen bond network as possible. At the highest H_2O loadings, some sodium cations can become dislodged from the zeolite framework surface and stabilized by water near closer to the center of the pore. This rearrangement may be responsible for the steep elbow observed in the H_2O isotherms. Due the the ubiquitous presence of water in combustion-related gas streams targeted for carbon capture and sequestration, expensive drying operations may be required to allow materials to provide sufficient CO_2 adsorption capacity.

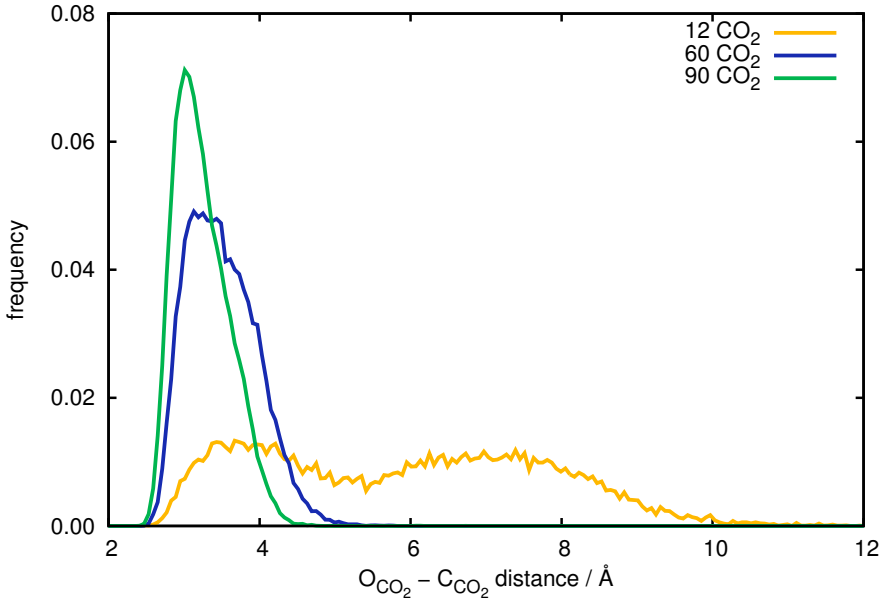

Figure 5.10: Histograms of CO_2-CO_2 distances at different total CO_2 loadings at 323 K.

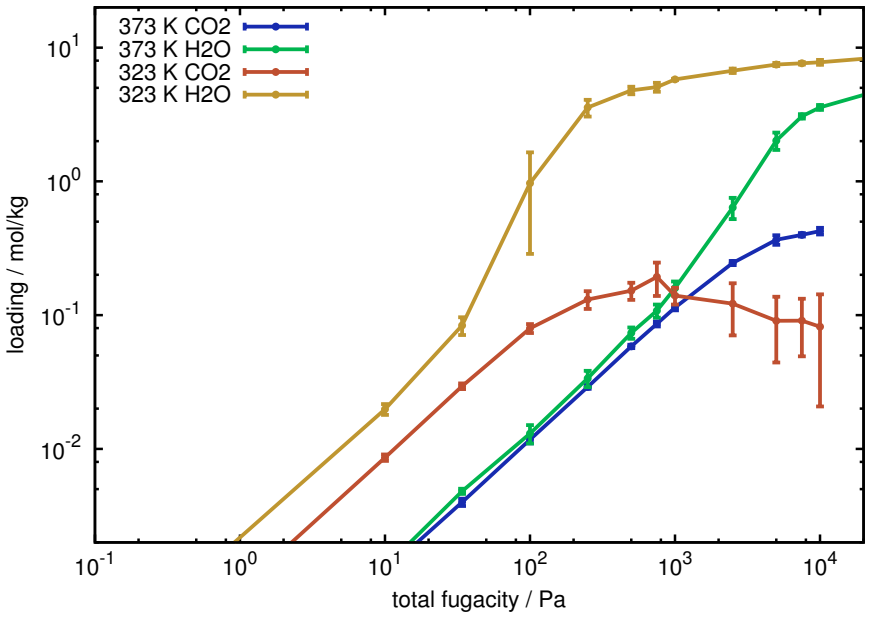

Figure 5.11: Mixture isotherms for a 99% CO_2, 1% H_2O mixture adsorbing in zeolite 13X at 323 and 373 K.

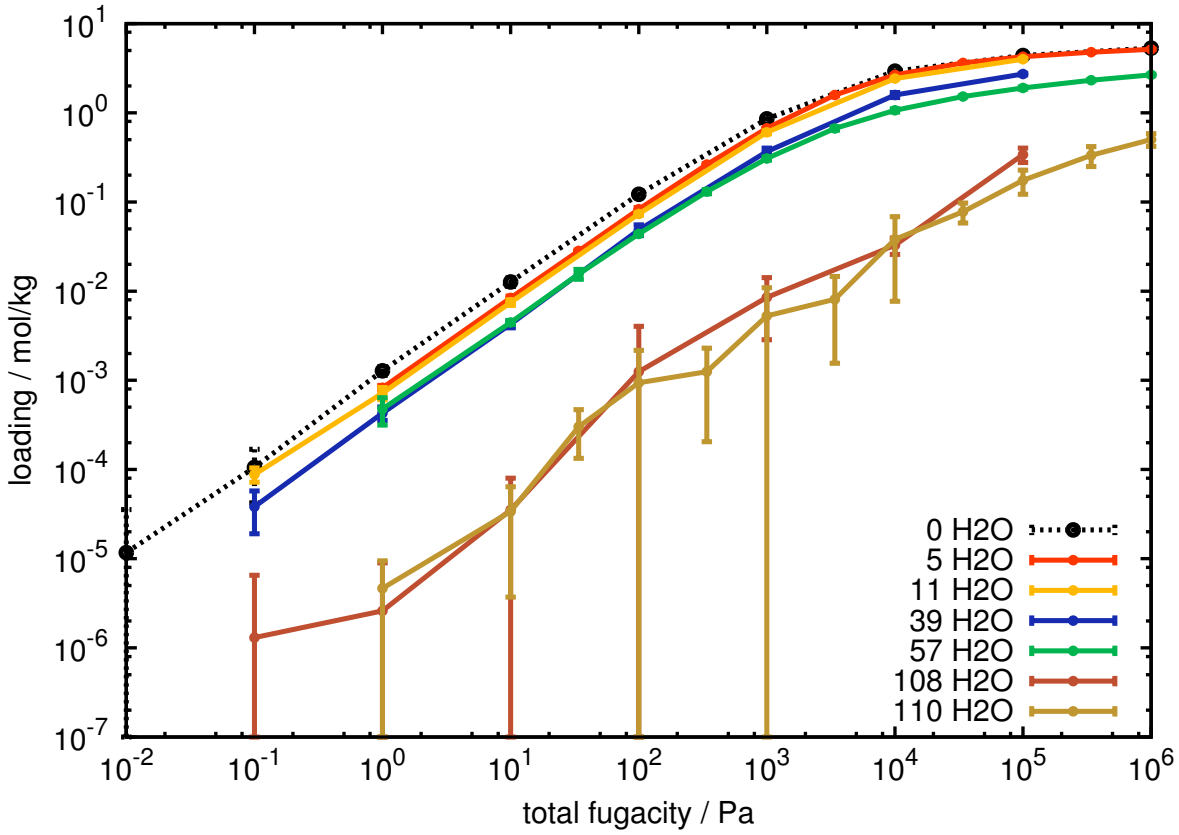

Figure 5.12: Adsorption isotherms for CO_2 in 13X with fixed loadings of water at 323 K. Water loadings are reported in molecules per unit cell. As the concentration of water in the material increases, the equilibrium CO_2 loading is reduced due to the occupation of pore volume and competition for coordination sites at the sodium cations.

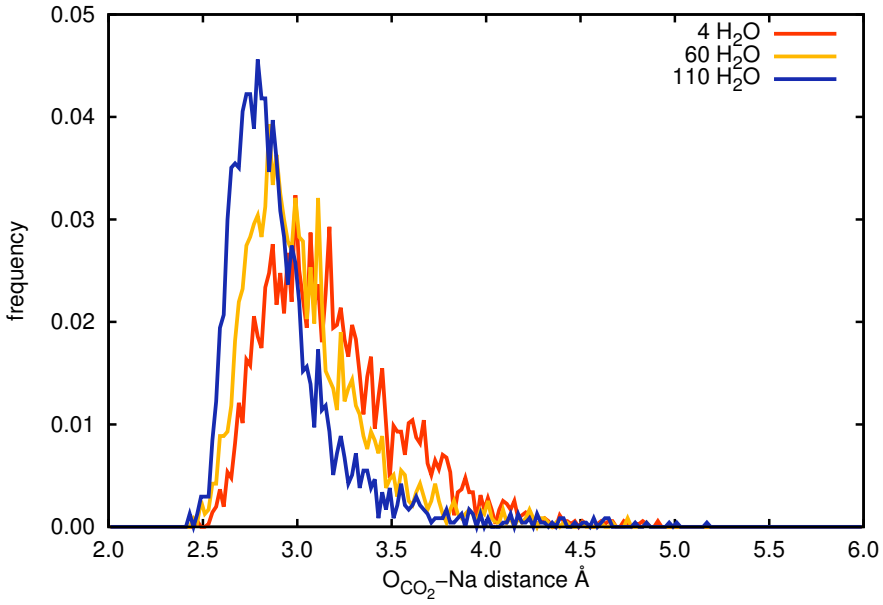

Figure 5.13: Histograms of O_{CO_2}-Na distances with different constant loadings of H_2O at 323 K.

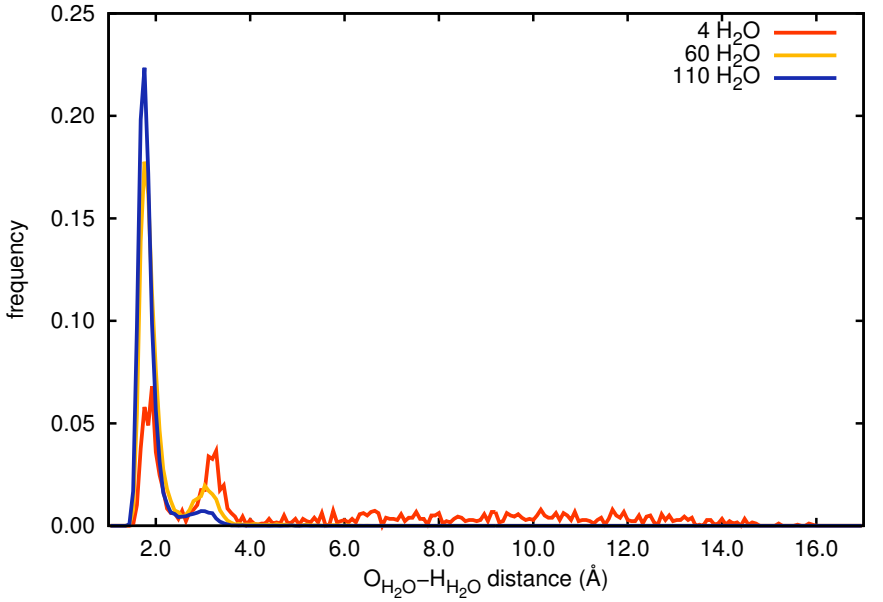

Figure 5.14: H_2O-H_2O distance histograms at different loadings of H_2O and 8 CO_2 per unit cell at 323 K.

Chapter 6

Conlusions

Improving carbon capture via adsorption processes is an important area of research to enable the use of CCS to reduce CO_2 emissions. Adsorption-based processes could potentially reduce the energy required to separate a unit of CO_2 and reduce the impact such processes would have on the net production of electricity. Molecular simulations have been used to study porous adsorbents and this dissertation has explored some of the issues related to simulating and interpreting adsorption data needed to evaluate solid sorbents.

The proper modeling of mixture adsorption requires accounting for any spatial segregation in the material. By applying ideal adsorption theory to separate Langmuir sites provides a better description of adsorption in these materials, especially when there are separate cavities where molecules can adsorb. It is important to take account of the fact that even a weakly adsorbing component may be able to adsorb at these sites, too. When some components adsorb weakly, like N_2 in a CO_2/N_2 mixture, it is important to get a good estimate of the saturation loading to correctly apply IAST, although the pressure required to saturate the pure component would be far larger than would be practical to measure in experiments.

To evaluate thousands of materials for CO_2 separations, chapter 3 presented a streamlined molecular simulation approach and coupled it with an equilibrium model of an adsorption process to score zeolite structures from a database based on their efficiency in separating CO_2 from the flue gas of a coal-fired power plant. Many materials were identified with a lower energy penalty than the standard amine scrubbing process. A GPU-based code was developed that accelerated the molecular simulations and allowed screening of millions of hypothetical zeolite structures.

For novel materials like metal-organic frameworks, this dissertation also addressed the use of quantum calculations to parameterize a classical force field to perform Monte Carlo simulations and predict adsorption isotherms. To properly model the interaction of CO_2 with the open metal sites in the MOF-74 series of materials, and additional attractive r^{-5} term was added to the pairwise potential to account for the additional interaction between the metal and CO_2 due to predominately short range forces like charge transfer and polarization. GCMC simulations using this potential were able to model experimental data for both Mg-MOF-74 and Zn-MOF-74.

Finally, the issue of H2O adsorption and H_2O/CO_2 co-adsorption was investigated in the zeolite 13X. GCMC simulations indicated that the presence of even 1% H2O in a gas mixture would dramatically reduce the capacity of this material to adsorb CO_2 at the conditions relevant for post-combustion CO_2 capture processes. The Type V shape of the pure H2O isotherms could be attributed to the rearrangement of sodium cations away from the Al-sites in the framework toward the center of the pores as water molecules can solvate and stabilize the sodiums in that location. The hydrogen bond network of H2O in the pores does not appear to be affected by the presence of CO_2.

References

[1] Tans, P.; Keeling, R.; 2012. `www.esrl.noaa.gov/gmd/ccgg/trends/`.

[2] Keeling, R. F.; Piper, S. C.; Heimann, M. *Nature* **1996**, *381*, 218–221.

[3] Le Quéré, C.; Aumont, O.; Bopp, L.; Bousquet, P.; Ciais, P.; Francey, R.; Heimann, M.; Keeling, C. D.; Keeling, R. F.; Kheshgi, H.; Peylin, P.; Piper, S. C.; Prentice, I. C.; Rayner, P. J. *Tellus B* **2003**, *55*, 649–656.

[4] *IPCC Special Report on Carbon Capture and Storage*; Tech. Rep.; Working Group III, Intergovernmental Panel on Climate Change; Geneva, Switzerland; 2005.

[5] Pierrehumbert, R. T. *Physics Today* **2011**, *64*, 33–38.

[6] Muller, R.; Curry, J.; Groom, D.; Jacobsen, R.; Perlmutter, S.; Rohde, R.; Rosenfeld, A.; Wickham, C.; Wurtele, J. *JGR-Atmospheres* **2011**, submitted.

[7] EIA; *Annual Energy Outlook 2011*; Tech. Rep. DOE/EIA-0383(2011); US Department of Energy; Washington, DC; 2011.

[8] Tabuchi, H. *The New York Times* **2012**.

[9] *Germany: Nuclear power plants to close by 2022*; 2011. `http://www.bbc.co.uk/news/world-europe-13592208`.

[10] EPRI; *The Power to Reduce CO2 Emissions: The Full Portfolio: 2009 Technical Report*; Tech. Rep. 1020389; Electric Power Research Institute; Palo Alto, CA; 2009.

[11] DOE/NETL; *DOE/NETL Carbon Dioxide Capture and Storage RDD Roadmap*; Tech. Rep.; National Energy Technology Laboratory; Pittsburgh, PA; 2010.

[12] Bottoms, R. R.; *Process for separating acidic gases*; 1930; US Patent 1,783,901.

[13] Rochelle, G. T. *Science* **2009**, *325*, 1652–1654.

[14] Freeman, S. A.; Dugas, R.; Wagener, D. V.; Nguyen, T.; Rochelle, G. T. *Energy Procedia* **2009**, *1*, 1489 – 1496.

[15] Merkel, T. C.; Lin, H.; Wei, X.; Baker, R. *J. Membr. Sci.* **2010**, *359*, 126 – 139.

[16] Bhown, A. S.; Freeman, B. C. *Environ. Sci. Technol.* **2011**, *45*, 8624–8632.

[17] Rota, R.; Wankat, P. C. *AIChE J.* **1990**, *36*, 1299–1312.

[18] Smit, B.; Maesen, T. L. M. *Chem. Rev.* **2008**, *108*, 4125–4184.

[19] Wilmer, C. E.; Leaf, M.; Lee, C. Y.; Farha, O. K.; Hauser, B. G.; Hupp, J. T.; Snurr, R. Q. *Nat. Chem.* **2012**, *4*, 83–89.

[20] Liu, B.; Smit, B. *J. Phys. Chem. C* **2010**, *114*, 8515–8522.

[21] Babarao, R.; Jiang, J. *Energy Environ. Sci.* **2008**, *1*, 139–143.

[22] Frenkel, D.; Smit, B. *Understanding Molecular Simulation: From Algorithms to Applications*, 2nd ed.; Academic Press: San Diego, 2002.

[23] Ewald, P. P. *Annalen der Physik* **1921**, *369*, 253–287.

[24] Dubbeldam, D.; Calero, S.; Vlugt, T. J. H.; Krishna, R.; Maesen, T. L. M.; Smit, B. *J. Phys. Chem. B* **2004**, *108*, 12301–12313.

[25] Dubbeldam, D.; Calero, S.; Vlugt, T. J. H.; Krishna, R.; Maesen, T. L. M.; Beerdsen, E.; Smit, B. *Phys. Rev. Lett.* **2004**, *93*, 088302.

[26] Dzubak, A. L.; Lin, L.-C.; Kim, J.; Swisher, J. A.; Poloni, R.; Maximoff, S. N.; Smit, B.; Gagliardi, L. *Nat. Chem.* **2012**, *advance online publication*.

[27] McDaniel, J. G.; Yu, K.; Schmidt, J. R. *J. Phys. Chem. C* **2012**, *116*, 1892–1903.

[28] Commission, I. S.; *Database of Zeolite Structures*; 2011. `http://www.iza-structure.org/databases/`.

[29] Park, K. S.; Ni, Z.; Côté, A. P.; Choi, J. Y.; Huang, R.; Uribe-Romo, F. J.; Chae, H. K.; O'Keeffe, M.; Yaghi, O. M. *Proc. Natl. Acad. Sci. U. S. A.* **2006**, *103*, 10186–10191.

[30] Yaghi, O. M.; O'Keeffe, M.; Ockwig, N. W.; Chae, H. K.; Eddaoudi, M.; Kim, J. *Nature* **2003**, *423*, 705–714.

[31] Deng, H.; Doonan, C. J.; Furukawa, H.; Ferreira, R. B.; Towne, J.; Knobler, C. B.; Wang, B.; Yaghi, O. M. *Science* **2010**, *327*, 846–850.

[32] Banerjee, R.; Phan, A.; Wang, B.; Knobler, C.; Furukawa, H.; O'Keeffe, M.; Yaghi, O. M. *Science* **2008**, *319*, 939–943.

[33] G. E. Keller, I.; Anderson, R. A.; Yon, C. M. In *Handbook of Separation Process Technology*; Rousseau, R. W., Ed.; John Wiley & Sons: New York, 1987; Chapter 12, pp 644–696.

[34] Myers, A. L.; Prausnitz, J. M. *AIChE J.* **1965**, *11*, 121–127.

[35] Costa, E.; Sotelo, J. L.; Calleja, G.; Marrón, C. *AIChE J.* **1981**, *27*, 5–12.

[36] Myers, A. L. *AIChE J.* **1983**, *29*, 691–693.

[37] Talu, O.; Zwiebel, I. *AIChE J.* **1986**, *32*, 1263–1276.

[38] Moon, H.; Tien, C. *Chem. Eng. Sci.* **1988**, *43*, 2967–2980.

[39] Eiden, U.; Schlünder, E. *Chem. Eng. Process.* **1990**, *28*, 1–11.

[40] Eiden, U.; Schlünder, E. *Chem. Eng. Process.* **1990**, *28*, 13–22.

[41] Chen, H.; Sholl, D. S. *Langmuir* **2007**, *23*, 6431–6437.

[42] Krishna, R.; van Baten, J. *Sep. Purif. Technol.* **2008**, *61*, 414–423.

[43] Myers, A. L. *Adsorption* **2005**, *11*, 37–42.

[44] Valenzuela, D. P.; Myers, A. L.; Talu, O.; Zwiebel, I. *AIChE J.* **1988**, *34*, 397–402.

[45] Cerofolini, C. F.; Rudzinski, W. In *Studies in Surface Science and Catalysis*; Rudzinski, W.; Steele, W. A.; Zgrablich, G., Eds.; Elsevier: Amsterdam, 1997; Vol. 104, Chapter 1, pp 1–103.

[46] Arnrich, S.; Kalies, G.; Bräuer, P. *Adsorption* **2011**, *17*, 823–831.

[47] Ritter, J. A.; Bhadra, S. J.; Ebner, A. D. *Langmuir* **2011**, *27*, 4700–4712.

[48] Cessford, N. F.; Seaton, N. A.; Düren, T. *Ind. Eng. Chem. Res.* **2012**, *51*, 4911–4921.

[49] Jee, S. E.; Sholl, D. S. *J. Am. Chem. Soc.* **2009**, *131*, 7896–7904.

[50] Van Heest, T.; Teich-McGoldrick, S. L.; Greathouse, J. A.; Allendorf, M. D.; Sholl, D. S. *J. Phys. Chem. C* **2012**, *116*, 13183–13195.

[51] Li, J.-R.; Sculley, J.; Zhou, H.-C. *Chem. Rev.* **2012**, *112*, 869–932.

[52] Pophale, R.; Cheeseman, P. A.; Deem, M. W. *Phys. Chem. Chem. Phys.* **2011**, *13*, 12407–12412.

[53] D'Alessandro, D. M.; Smit, B.; Long, J. R. *Angew. Chem., Int. Ed.* **2010**, *49*, 6058–6082.

[54] Sumida, K.; Rogow, D. L.; Mason, J. A.; McDonald, T. M.; Bloch, E. D.; Herm, Z. R.; Bae, T.-H.; Long, J. R. *Chem. Rev.* **2012**, *112*, 724–781.

[55] Suh, M. P.; Park, H. J.; Prasad, T. K.; Lim, D.-W. *Chem. Rev.* **2012**, *112*, 782–835.

[56] Lin, L.-C.; Berger, A. H.; Martin, R. L.; Kim, J.; Swisher, J. A.; Jariwala, K.; Rycroft, C. H.; Bhown, A. S.; Deem, M. W.; Haranczyk, M.; Smit, B. *Nat. Mater.* **2012**, *11*, 633–641.

[57] Smit, B. *Mol. Phys.* **1995**, *85*, 153–172.

[58] Walton, K. S.; Millward, A. R.; Dubbeldam, D.; Frost, H.; Low, J. J.; Yaghi, O. M.; Snurr, R. Q. *J. Am. Chem. Soc.* **2008**, *130*, 406–407.

[59] Scholl, S.; Schachtl, M.; Sievers, W.; Schweighart, P.; Mersmann, A. *Chem. Eng. Technol.* **1991**, *14*, 311–324.

[60] Richter, E.; Wilfried, S.; Myers, A. L. *Chem. Eng. Sci.* **1989**, *44*, 1609–1616.

[61] Sievers, W.; Mersmann, A. *Chem. Eng. Technol.* **1994**, *17*, 325–337.

[62] Hu, X.; Do, D. D. *AIChE J.* **1995**, *41*, 1585–1592.

[63] Krishna, R.; Calero, S.; Smit, B. *Chem. Eng. J.* **2002**, *88*, 81–94.

[64] Gumma, S.; Talu, O. *Langmuir* **2010**, *26*, 17013–17023.

[65] García-Pérez, E.; Parra, J.; Ania, C.; García-Sánchez, A.; van Baten, J.; Krishna, R.; Dubbeldam, D.; Calero, S. *Adsorption* **2007**, *13*, 469–476.

[66] García-Sánchez, A.; Ania, C. O.; Parra, J. B.; Dubbeldam, D.; Vlugt, T. J. H.; Krishna, R.; Calero, S. *J. Phys. Chem. C* **2009**, *113*, 8814–8820.

[67] Calero, S.; Dubbeldam, D.; Krishna, R.; Smit, B.; Vlugt, T. J. H.; Denayer, J. F. M.; Martens, J. A.; Maesen, T. L. M. *J. Am. Chem. Soc.* **2004**, *126*, 11377–11386.

[68] Talu, O.; Myers, A. L. *AIChE J.* **2001**, *47*, 1160–1168.

[69] Bae, T.-H.; Hudson, M. R.; Mason, J. A.; Queen, W. L.; Dutton, J. J.; Sumida, K.; Micklash, K. J.; Kaye, S. S.; Brown, C. M.; Long, J. R. *Energy Environ. Sci.* **2012**, –.

[70] Cavenati, S.; Grande, C. A.; Rodrigues, A. E. *J. Chem. Eng. Data* **2004**, *49*, 1095–1101.

[71] Wang, Y.; LeVan, M. D. *J. Chem. Eng. Data* **2010**, *55*, 3189–3195.

[72] Ciferno, J. P.; Marano, J. J.; Munson, R. K. *Chem. Eng. Prog.* **2011**, *107*, 34–44.

[73] Ferey, G. *Chem. Soc. Rev.* **2008**, *37*, 191–214.

[74] Krishna, R.; van Baten, J. M. *Phys. Chem. Chem. Phys.* **2011**, *13*, 10593–10616.

[75] Krishna, R.; Long, J. R. *J. Phys. Chem. C* **2011**, *115*, 12941–12950.

[76] Yazaydin, A. Ö.; Snurr, R. Q.; Park, T.-H.; Koh, K.; Liu, J.; LeVan, M. D.; Benin, A. I.; Jakubczak, P.; Lanuza, M.; Galloway, D. B.; Low, J. J.; Willis, R. R. *J. Am. Chem. Soc.* **2009**, *131*, 18198–18199.

[77] NETL; *Carbon Dioxide Capture from Existing Coal-Fired Power Plants*; Tech. Rep. DOE/NETL-401/110907; National Energy Technology Laboratory; Pittsburg, Pa; 2007.

[78] Lemmon, E. W.; Huber, M. L.; McLinden, M. O.; *NIST Reference Fluid Thermodynamic and Transport Properties Database (REFPROP): Version9.0*; 2010. `http://www.nist.gov/srd/nist23.cfm`.

[79] Deem, M. W.; Pophale, R.; Cheeseman, P. A.; Earl, D. J. *J. Phys. Chem. C* **2009**, *113*, 21353–21360.

[80] Sanders, M. J.; Leslie, M.; Catlow, C. R. A. *J. Chem. Soc., Chem. Commun.* **1984**, 1271–1273.

[81] van Beest, B. W. H.; Kramer, G. J.; van Santen, R. A. *Phys. Rev. Lett.* **1990**, *64*, 1955–1958.

[82] Willems, T. F.; Rycroft, C. H.; Kazi, M.; Meza, J. C.; Haranczyk, M. *Microporous Mesoporous Mater.* **2012**, *149*, 134 – 141.

[83] García-Pérez, E.; Dubbeldam, D.; Liu, B.; Smit, B.; Calero, S. *Angew. Chem., Int. Ed.* **2007**, *46*, 276–278.

[84] Löwenstein, W. *Am. Mineral.* **1954**, *39*, 92–96.

[85] Mayo, S. L.; Olafson, B. D.; Goddard, W. A. *J. Chem. Phys.* **1990**, *94*, 8897–8909.

[86] Potoff, J. J.; Siepmann, J. I. *AIChE J.* **2001**, *47*, 1676–1682.

[87] Xu, Q.; Zhong, C. *J. Phys. Chem. C* **2010**, *114*, 5035–5042.

[88] Kim, J.; Rodgers, J. M.; Athènes, M.; Smit, B. *J. Chem. Theory Comput.* **2011**, *7*, 3208–3222.

[89] Bates, S. P.; van Well, W. J. M.; van Santen, R. A.; Smit, B. *J. Am. Chem. Soc.* **1996**, *118*, 6753–6759.

[90] Haranczyk, M.; Sethian, J. A. *Proc. Natl. Acad. Sci. U. S. A.* **2009**, *106*, 21472–21477.

[91] Haranczyk, M.; Sethian, J. A. *J. Chem. Theory Comput.* **2010**, *6*, 3472–3480.

[92] Rao, M. B.; Sircar, S. *Langmuir* **1999**, *15*, 7258–7267.

[93] Martin, R. L.; Smit, B.; Haranczyk, M. *J. Chem. Inf. Model.* **2012**, *52*, 308–318.

[94] Simancas, R.; Dari, D.; Velamazán, N.; Navarro, M. T.; Cantín, A.; Jordá, J. L.; Sastre, G.; Corma, A.; Rey, F. *Science* **2010**, *330*, 1219–1222.

[95] Jariwala, K.; Haranczyk, M.; *Carbon Capture Materials Database*; 2011. `http://www.carboncapturematerials.org`.

[96] Valenzano, L.; Civalleri, B.; Sillar, K.; Sauer, J. *J. Phys. Chem. C* **2011**, *115*, 21777–21784.

[97] Chui, S. S.-Y.; Lo, S. M.-F.; Charmant, J. P. H.; Orpen, A. G.; Williams, I. D. *Science* **1999**, *283*, 1148–1150.

[98] Millward, A. R.; Yaghi, O. M. *J. Am. Chem. Soc.* **2005**, *127*, 17998–17999.

[99] Dietzel, P. D. C.; Besikiotis, V.; Blom, R. *J. Mater. Chem.* **2009**, *19*, 7362–7370.

[100] Mason, J. A.; Sumida, K.; Herm, Z. R.; Krishna, R.; Long, J. R. *Energy Environ. Sci.* **2011**, *4*, 3030–3040.

[101] Grajciar, L.; Bludský, O.; Nachtigall, P. *J. Phys. Chem. Lett.* **2010**, *1*, 3354–3359.

[102] Getman, R. B.; Bae, Y.-S.; Wilmer, C. E.; Snurr, R. Q. *Chem. Rev.* **2012**, *112*, 703–723.

[103] Wu, J. Y.; Liu, Q. L.; Xiong, Y.; Zhu, A. M.; Chen, Y. *J. Phys. Chem. B* **2009**, *113*, 4267–4274.

[104] McDonald, T. M.; Lee, W. R.; Mason, J. A.; Wiers, B. M.; Hong, C. S.; Long, J. R. *J. Am. Chem. Soc.* **2012**, *134*, 7056–7065.

[105] Liu, B.; Smit, B. *Langmuir* **2009**, *25*, 5918–5926.

[106] Rappe, A. K.; Casewit, C. J.; Colwell, K. S.; Goddard, W. A.; Skiff, W. M. *J. Am. Chem. Soc.* **1992**, *114*, 10024–10035.

[107] Hagberg, D.; Karlström, G.; Roos, B. O.; Gagliardi, L. *J. Am. Chem. Soc.* **2005**, *127*, 14250–14256.

[108] Engkvist, O.; Åstrand, P.-O.; Karlström, G. *Chem. Rev.* **2000**, *100*, 4087–4108.

[109] Krishna, R.; van Baten, J. M. *J. Membr. Sci.* **2011**, *377*, 249 – 260.

[110] Gagliardi, L.; Lindh, R.; Karlstrom, G. *J. Chem. Phys.* **2004**, *121*, 4494–4500.

[111] Boys, S.; Bernardi, F. *Mol. Phys.* **1970**, *19*, 553–566.

[112] Karlström, G.; Lindh, R.; Malmqvist, P.-Å.; Roos, B. O.; Ryde, U.; Veryazov, V.; Widmark, P.-O.; Cossi, M.; Schimmelpfennig, B.; Neogrady, P.; Seijo, L. *Comp. Mater. Sci.* **2003**, *28*, 222 – 239.

[113] Aquilante, F.; Pedersen, T. B.; Lindh, R. *J. Chem. Phys.* **2007**, *126*, 194106.

[114] Aquilante, F.; Malmqvist, P.-Å.; Pedersen, T. B.; Ghosh, A.; Roos, B. O. *J. Chem. Theory Comput.* **2008**, *4*, 694–702.

[115] Aquilante, F.; Pedersen, T. B.; Lindh, R.; Roos, B. O.; de Meras, A. S.; Koch, H. *J. Chem. Phys.* **2008**, *129*, 024113.

[116] Hess, B. A. *Phys. Rev. A* **1986**, *33*, 3742–3748.

[117] Roos, B. O.; Lindh, R.; Malmqvist, P.-Å.; Veryazov, V.; Widmark, P.-O. *J. Phys. Chem. A* **2004**, *108*, 2851–2858.

[118] Roos, B. O.; Lindh, R.; Malmqvist, P.-Å.; Veryazov, V.; Widmark, P.-O. *J. Phys. Chem. A* **2005**, *109*, 6575–6579.

[119] Holt, A.; Boström, J.; Karlström, G.; Lindh, R. *J. Comput. Chem.* **2010**, *31*, 1583–1591.

[120] Soler, J. M.; Artacho, E.; Gale, J. D.; García, A.; Junquera, J.; Ordejón, P.; Sánchez-Portal, D. *Journal of Physics: Condensed Matter* **2002**, *14*, 2745.

[121] Kresse, G.; Furthmüller, J. *Comp. Mater. Sci.* **1996**, *6*, 15 – 50.

[122] Kresse, G.; Furthmüller, J. *Phys. Rev. B* **1996**, *54*, 11169–11186.

[123] Giannozzi, P.; et al. *J. Phys. Cond. Mat.* **2009**, *21*, 395502.

[124] Lee, K.; Murray, E. D.; Kong, L.; Lundqvist, B. I.; Langreth, D. C. *Phys. Rev. B* **2010**, *82*, 081101.

[125] Lee, K.; Murray, E. D.; Kong, L.; Lundqvist, B. I.; Langreth, D. C. *Phys. Rev. B* **2010**, *82*, 081101.

[126] Román-Pérez, G.; Soler, J. M. *Phys. Rev. Lett.* **2009**, *103*, 096102.

[127] Moreno, J.; Soler, J. M. *Phys. Rev. B* **1992**, *45*, 13891–13898.

[128] Queen, W. L.; Brown, C. M.; Britt, D. K.; Zajdel, P.; Hudson, M. R.; Yaghi, O. M. *J. Phys. Chem. C* **2011**, *115*, 24915–24919.

[129] Rosi, N. L.; Kim, J.; Eddaoudi, M.; Chen, B.; O'Keeffe, M.; Yaghi, O. M. *J. Am. Chem. Soc.* **2005**, *127*, 1504–1518.

[130] Dietzel, P. D. C.; Blom, R.; Fjellvåg, H. *Eur. J. Inorg. Chem.* **2008**, *2008*, 3624–3632.

[131] Vuong, T.; Monson, P. A. *Langmuir* **1996**, *12*, 5425–5432.

[132] Simmons, J. M.; Wu, H.; Zhou, W.; Yildirim, T. *Energy Environ. Sci.* **2011**, *4*, 2177–2185.

[133] Liu, J.; Benin, A. I.; Furtado, A. M. B.; Jakubczak, P.; Willis, R. R.; LeVan, M. D. *Langmuir* **2011**, *27*, 11451–11456.

[134] Bao, Z.; Yu, L.; Ren, Q.; Lu, X.; Deng, S. *J. Colloid Interface Sci.* **2011**, *353*, 549 – 556.

[135] Caskey, S. R.; Wong-Foy, A. G.; Matzger, A. J. *J. Am. Chem. Soc.* **2008**, *130*, 10870–10871.

[136] Herm, Z. R.; Swisher, J. A.; Smit, B.; Krishna, R.; Long, J. R. *J. Am. Chem. Soc.* **2011**, *133*, 5664–5667.

[137] Kizzie, A. C.; Wong-Foy, A. G.; Matzger, A. J. *Langmuir* **2011**, *27*, 6368–6373.

[138] Sillar, K.; Hofmann, A.; Sauer, J. *J. Am. Chem. Soc.* **2009**, *131*, 4143–4150.

[139] NETL; *Cost and Performance Baseline for Fossil Energy Plants*; Tech. Rep. DOE/NETL-2010/1397; National Energy Technology Laboratory; Pittsburgh, PA; 2010.

[140] Jänchen, J.; Ackermann, D.; Stach, H.; Brösicke, W. *Solar Energy* **2004**, *76*, 339–344.

[141] Hou, Y.; Vidu, R.; Stroeve, P. *Ind. Eng. Chem. Res.* **2011**, *50*, 8954–8964.

[142] Mérel, J.; Clausse, M.; Meunier, F. *Environ. Prog.* **2006**, *25*, 327–333.

[143] Ko, D.; Siriwardane, R.; Biegler, L. T. *Ind. Eng. Chem. Res.* **2003**, *42*, 339–348.

[144] Chue, K. T.; Kim, J. N.; Yoo, Y. J.; Cho, S. H.; Yang, R. T. *Ind. Eng. Chem. Res.* **1995**, *34*, 591–598.

[145] Wang, Y.; LeVan, M. D. *J. Chem. Eng. Data* **2009**, *54*, 2839–2844.

[146] Brandani, F.; Ruthven, D. M. *Ind. Eng. Chem. Res.* **2004**, *43*, 8339–8344.

[147] Ferreira, D.; Magalhães, R.; Taveira, P.; Mendes, A. *Ind. Eng. Chem. Res.* **2011**, *50*, 10201–10210.

[148] Lee, K.-M.; Lim, Y.-H.; Jo, Y.-M. *Environ. Technol.* **2012**, *33*, 77–84.

[149] Castillo, J.; Dubbeldam, D.; Vlugt, T.; Smit, B.; Calero, S. *Mol. Sim.* **2009**, *35*, 1067–1076.

[150] Lee, S. H.; Moon, G. K.; Choi, S. G.; Kim, H. S. *J. Phys. Chem.* **1994**, *98*, 1561–1569.

[151] Faux, D. A.; Smith, W.; Forester, T. R. *J. Phys. Chem. B* **1997**, *101*, 1762–1768.

[152] Beauvais, C.; Boutin, A.; Fuchs, A. H. *Comptes Rendus Chimie* **2005**, *8*, 485–490.

[153] Bellat, J.-P.; Paulin, C.; Jeffroy, M.; Boutin, A.; Paillaud, J.-L.; Patarin, J.; Di Lella, A.; Fuchs, A. *J. Phys. Chem. C* **2009**, *113*, 8287–8295.

[154] Di Lella, A.; Desbiens, N.; Boutin, A.; Demachy, I.; Ungerer, P.; Bellat, J.-P.; Fuchs, A. H. *Phys. Chem. Chem. Phys.* **2006**, *8*, 5396–5406.

[155] Hutson, N. D.; Zajic, S. C.; Yang, R. T. *Ind. Eng. Chem. Res.* **2000**, *39*, 1775–1780.

[156] Boddenberg, B.; Rakhmatkariev, G. U.; Hufnagel, S.; Salimov, Z. *Phys. Chem. Chem. Phys.* **2002**, *4*, 4172–4180.

[157] Olson, D. H. *J. Phys. Chem.* **1970**, *74*, 2758–2764.

[158] Berendsen, H. J. C.; Grigera, J. R.; Straatsma, T. P. *J. Phys. Chem.* **1987**, *91*, 6269–6271.

[159] Sing, K. S. W.; Everett, D. H.; Haul, R. A. W.; Moscou, L.; Pierotti, R. A.; Rouquérol, J.; Siemieniewska, T. *Pure Appl. Chem.* **1985**, *57*, 603–619.

[160] *NIST Chemistry WebBook*; 2012. `http://webbook.nist.gov`.

[161] Mähler, J.; Persson, I. *Inorg. Chem.* **2012**, *51*, 425–438.

[162] Do, D.; Do, H. *Carbon* **2000**, *38*, 767 – 773.

[163] Neitsch, M.; Heschel, W.; Suckow, M. *Carbon* **2001**, *39*, 1437 – 1438.

[164] Talu, O.; Meunier, F. *AIChE J.* **1996**, *42*, 809–819.

[165] R Development Core Team; *R: A Language and Environment for Statistical Computing*; R Foundation for Statistical Computing; Vienna, Austria; 2011; ISBN 3-900051-07-0. `http://www.R-project.org/`.

[166] Stone, A. J. *The theory of intermolecular forces*; Clarendon Press; Oxford University Press, 1996.

Appendix A

Additional information for "Evaluating mixture adsorption models using molecular simulation"

Tables A.1-A.4 give parameters for the dual-site Langmuir isotherm for the pure components adsorbing in the materials considered in this study. All fitting was performed with the R statistical package.[165]

Table A.1: Dual-site Langmuir isotherm parameters for PCOD8286959.

	b_1 Pa^{-1}	m_1 $mol\ kg^{-1}$	b_2 Pa^{-1}	m_2 $mol\ kg^{-1}$
CO_2	5.439×10^{-3}	0.4229	5.342×10^{-7}	8.811
N_2	3.894×10^{-7}	0.4229	4.548×10^{-8}	7.298

Table A.2: Dual-site Langmuir isotherm parameters for PCOD8200029.

	b_1 Pa^{-1}	m_1 $mol\ kg^{-1}$	b_2 Pa^{-1}	m_2 $mol\ kg^{-1}$
CO_2	4.924×10^{-4}	1.510	5.226×10^{-7}	0.7354
N_2	3.837×10^{-7}	1.510	9.083×10^{-8}	0.7564

Table A.3: Dual-site Langmuir isotherm parameters for MOR.

	b_1 Pa^{-1}	m_1 $mol\ kg^{-1}$	b_2 Pa^{-1}	m_2 $mol\ kg^{-1}$
CO_2	4.490×10^{-4}	4.165	1.203×10^{-6}	13.39
C_3H_8	3.322×10^{-4}	3.005	1.603×10^{-8}	4.993

Table A.4: Dual-site Langmuir isotherm parameters for NaX.

	b_1 Pa^{-1}	m_1 $mol\ kg^{-1}$	b_2 Pa^{-1}	m_2 $mol\ kg^{-1}$
CO_2	2.576×10^{-4}	4.687	8.122×10^{-7}	1.994
N_2	2.827×10^{-7}	4.687	5.468×10^{-9}	3.055

Appendix B

Additional information for "In silico screening of carbon capture materials"

We have collected all results obtained in this work in a database, accessible at *www.carboncapturematerials.org*. The investigated materials have been characterized in terms of:

- Their pore geometry (pore measured by the diameter of the largest included and free spheres, accessible volume and surface areas)
- Adsorption properties (Henry coefficients and heats of adsorption for CO_2 and N_2, estimated Langmuir isotherms and in some cases simulated isotherms)
- Performance using the model discussed in the article (including parasitic energy, working capacity, and CO_2 purity)

The web interface allows the user to search for specific materials or materials with certain properties, and provides a graphical interface to browse the results. For example, plotting the parasitic energy as a function of the CO_2 Henry coefficient gives Figure 3.2. In this figure each point is clickable and takes the user to the material entry page, which contains all the relevant properties for a particular material.

Appendix C

Additional information for "Ab initio carbon capture in open-site metal organic frameworks"

C.1 Description of the clusters

Atom types for the framework (Mg-MOF-74) were defined based on the symmetry of the periodic system, which has 9 distinct atom types. All metal sites are equivalent (Mg), each 2,5-dioxido-1, 4-benzenedicarboxylate (dobdc) linker has 3 types of oxygen atoms (O_a, O_b, O_c), 4 types of carbon atoms (C_a, C_b, C_c, C_d), and 1 type of hydrogen (H) shown in Figure 4.1. For each atom type (excluding H), a cluster was defined in a way to best represent the local environment of that atom type, shown in Figures C.1-C.11. Hydrogen was not explicitly considered for our parameterization due to its small contribution to the total interaction energy. The standard Universal force field parameters for H were adapted to our functional form.[106]

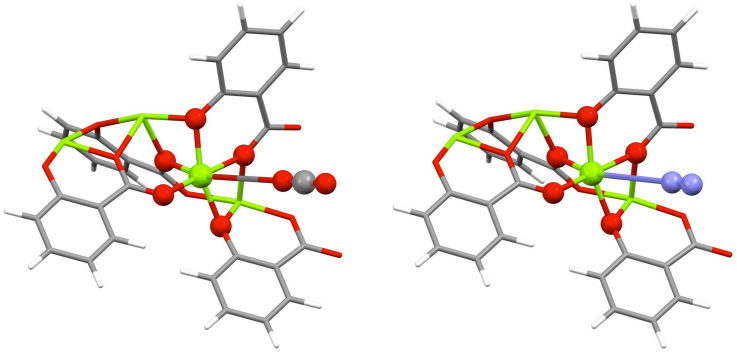

Figure C.1: (Mg-MOF-74) Mg atom type cluster with CO_2 (left) and N2 (right) approaching. Color and basis function contraction code: Green (Mg) ball = 17s12p6d2f2g/4s3p1d, Green (Mg) capped stick = 17s12p6d2f2g/3s2p, Red (O) ball = 14s9p4d3f2g /3s2p1d, Red (O) capped stick = 14s9p4d3f2g/2s1p, Gray (C) ball = 14s9p4d3f2g/3s2p1d, Gray (C) capped stick = 14s9p4d3f2g/2s1p, Purple (N) ball = 14s9p4d3f2g /3s2p1d, White (H) capped stick = 8s4p3d1f/1s.

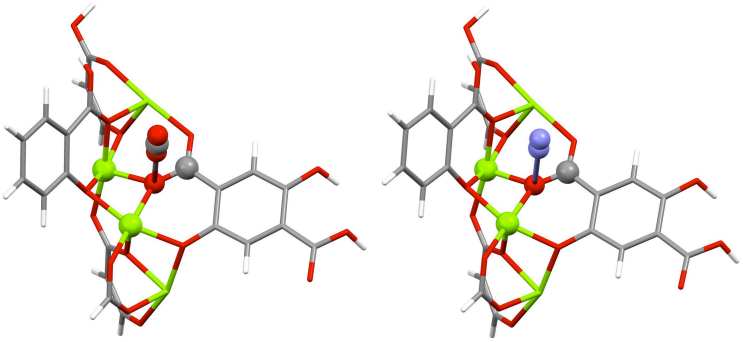

Figure C.2: (Mg-MOF-74) O_a atom type cluster with CO_2 (left) and N2 (right) approaching. Color and basis function contraction code: Green (Mg) ball = 17s12p6d2f2g/4s3p1d, Green (Mg) capped stick = 17s12p6d2f2g/3s2p, Red (O) ball = 14s9p4d3f2g /3s2p1d, Red (O) capped stick = 14s9p4d3f2g/2s1p, Gray (C) ball = 14s9p4d3f2g/3s2p1d, Gray (C) capped stick = 14s9p4d3f2g/2s1p, Purple (N) ball = 14s9p4d3f2g /3s2p1d, White (H) capped stick = 8s4p3d1f/1s.

C.2 NEMO decomposition

The partitioned contributions to the interaction energy are computed by a similar (truncated) version of the formula presented by Holt et al.[119] Prior to the calculation of the partitioned

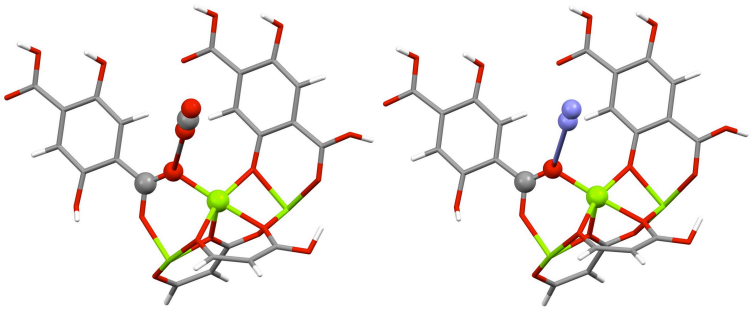

Figure C.3: (Mg-MOF-74) O_b atom type cluster with CO_2 (left) and N2 (right) approaching. Color and basis function contraction code: Green (Mg) ball = 17s12p6d2f2g/4s3p1d, Green (Mg) capped stick = 17s12p6d2f2g/3s2p, Red (O) ball = 14s9p4d3f2g /3s2p1d, Red (O) capped stick = 14s9p4d3f2g/2s1p, Gray (C) ball = 14s9p4d3f2g/3s2p1d, Gray (C) capped stick = 14s9p4d3f2g/2s1p, Purple (N) ball = 14s9p4d3f2g /3s2p1d, White (H) capped stick = 8s4p3d1f/1s.

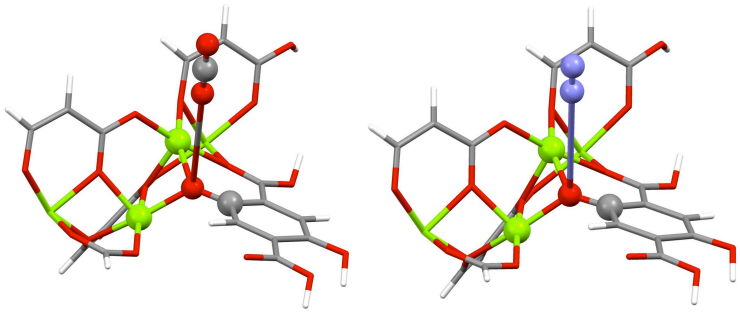

Figure C.4: (Mg-MOF-74) O_c atom type cluster with CO_2 (left) and N2 (right) approaching. Color and basis function contraction code: Green (Mg) ball = 17s12p6d2f2g/4s3p1d, Green (Mg) capped stick = 17s12p6d2f2g/3s2p, Red (O) ball = 14s9p4d3f2g /3s2p1d, Red (O) capped stick = 14s9p4d3f2g/2s1p, Gray (C) ball = 14s9p4d3f2g/3s2p1d, Gray (C) capped stick = 14s9p4d3f2g/2s1p, Purple (N) ball = 14s9p4d3f2g /3s2p1d, White (H) capped stick = 8s4p3d1f/1s.

contributions, the LoProp properties are simplified. The polarizabilities are made isotropic, the dipoles are modified to reproduce the molecular quadrupole, and the quadrupoles are deleted.

The electrostatic energy contribution, E_{elec} , polarization energy contribution, E_{pol}, and dispersion energy contribution, E_{disp}, are given by the following equaiotns, where T is the interaction energy tensor (see Stone[166]). Indices A and B are associated with either MOF or guest molecules (i.e. no intramolecular contribution), and i, j are atomic sites.

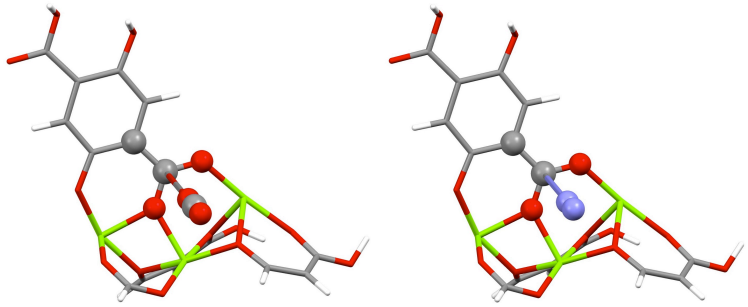

Figure C.5: (Mg-MOF-74) C_a atom type cluster with CO_2 (left) and N2 (right) approaching. Color and basis function contraction code: Green (Mg) capped stick = 17s12p6d2f2g/3s2p, Red (O) ball = 14s9p4d3f2g /3s2p1d, Red (O) capped stick = 14s9p4d3f2g/2s1p, Gray (C) ball = 14s9p4d3f2g/3s2p1d, Gray (C) capped stick = 14s9p4d3f2g/2s1p, Purple (N) ball = 14s9p4d3f2g /3s2p1d, White (H) capped stick = 8s4p3d1f/1s.

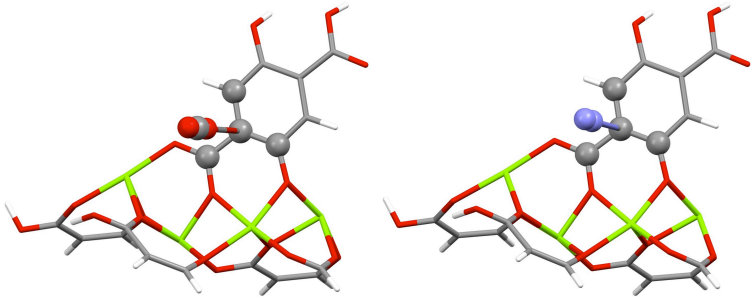

Figure C.6: (Mg-MOF-74) C_b atom type cluster with CO_2 (left) and N2 (right) approaching. Color and basis function contraction code: Green (Mg) capped stick = 17s12p6d2f2g/3s2p, Red (O) ball = 14s9p4d3f2g /3s2p1d, Red (O) capped stick = 14s9p4d3f2g/2s1p, Gray (C) ball = 14s9p4d3f2g/3s2p1d, Gray (C) capped stick = 14s9p4d3f2g/2s1p, Purple (N) ball = 14s9p4d3f2g /3s2p1d, White (H) capped stick = 8s4p3d1f/1s.

$$E_{elec} = \sum_{i}^{A}\sum_{j}^{B}\left(T^{ij}(q^i q^j) + T^{ij}_{\alpha}(q^i\mu^j_{\alpha} - \mu^j_{\alpha}q^i) - T^{ij}_{\alpha\beta}(\mu^i_{\alpha}\mu^j_{\beta})\right) \tag{C.1}$$

$$E_{pol} = -\frac{1}{2}\sum_{i}^{A}\mu^{i,ind}_{\alpha}F(A)_{\alpha} \tag{C.2}$$

$$E_{disp} = -\sum_{i}^{A}\sum_{j}^{B}(D^{ij})\frac{E_{AB}}{4}\alpha^i_{\alpha\beta}\alpha^j_{\gamma\delta}T^{ij}_{\alpha\gamma}T^{ij}_{\beta\delta} \tag{C.3}$$

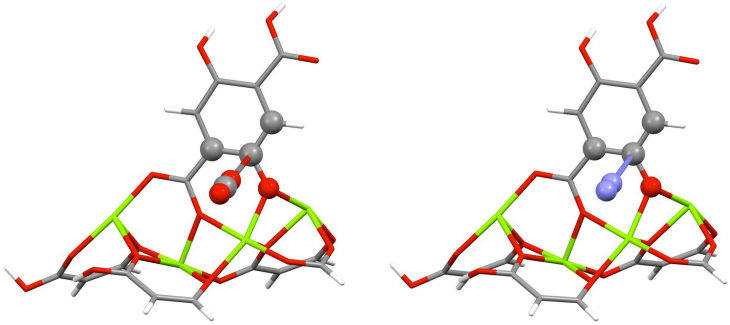

Figure C.7: (Mg-MOF-74) C_c atom type cluster with CO_2 (left) and N2 (right) approaching. Color and basis function contraction code: Green (Mg) capped stick = 17s12p6d2f2g/3s2p, Red (O) ball = 14s9p4d3f2g /3s2p1d, Red (O) capped stick = 14s9p4d3f2g/2s1p, Gray (C) ball = 14s9p4d3f2g/3s2p1d, Gray (C) capped stick = 14s9p4d3f2g/2s1p, Purple (N) ball = 14s9p4d3f2g /3s2p1d, White (H) capped stick = 8s4p3d1f/1s.

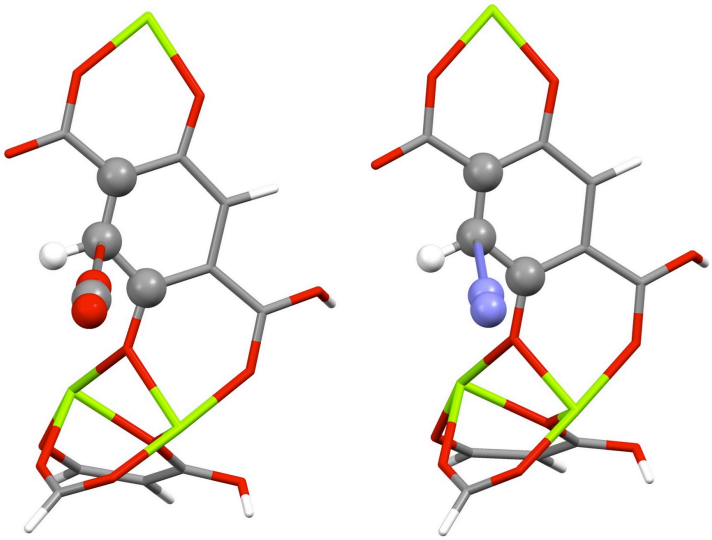

Figure C.8: (Mg-MOF-74) C_d atom type cluster with CO_2 (left) and N2 (right) approaching. Color and basis function contraction code: Green (Mg) capped stick = 17s12p6d2f2g/3s2p, Red (O) ball = 14s9p4d3f2g /3s2p1d, Red (O) capped stick = 14s9p4d3f2g/2s1p, Gray (C) ball = 14s9p4d3f2g/3s2p1d, Gray (C) capped stick = 14s9p4d3f2g/2s1p, Purple (N) ball = 14s9p4d3f2g /3s2p1d, White (H) ball = 8s4p3d1f/2s1p, White (H) capped stick = 8s4p3d1f/1s.

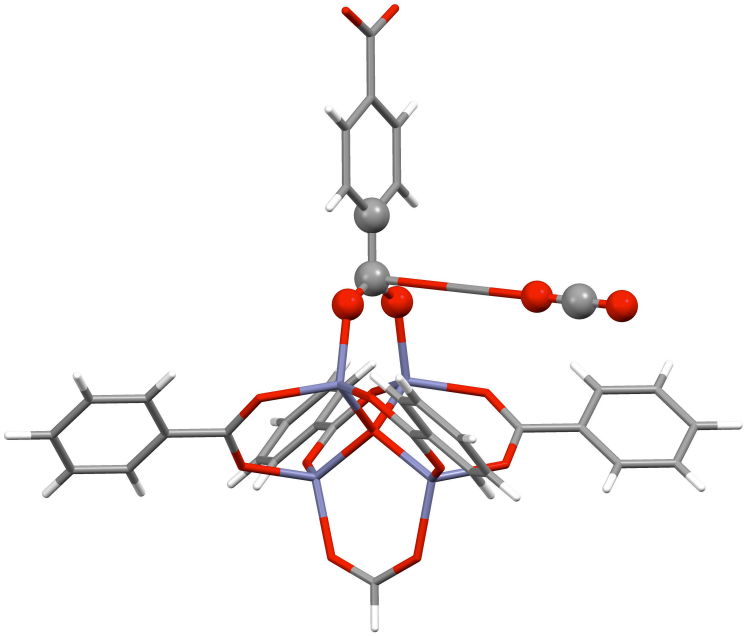

Figure C.9: (MOF-5) C_a atom type cluster with CO_2 approaching. Color and basis function contraction code: Purple (Zn) capped stick = 21s15p10d6f4g2h/4s3p1d, Red (O) ball = 14s9p4d3f2g /3s2p1d, Red (O) capped stick = 14s9p4d3f2g/2s1p, Gray (C) ball = 14s9p4d3f2g/3s2p1d, Gray (C) capped stick = 14s9p4d3f2g/2s1p, White (H) capped stick = 8s4p3d1f/1s.

For E_{elect}, μ are the modified dipoles. To estimate E_{pol}, we use an induced point-dipole model, which is iterated until convergence ($\delta E < 1.0E^{-10}$ a.u.). Equation C.2 gives the polarization contribution for molecule A in the presence of B (the same is true for B in the presence of A). Here $\mu_\alpha^{i,ind} = \alpha_{\alpha\beta}^i F(A)_\beta^{total}$ where $\alpha_{\alpha\beta}^i$ are the (isotropic) polarizabilities, and $F(A)_\beta^{total}$ includes the induction due to permanent moments as well as induced moments. For E_{disp}, it is the same definition for $\mu_\alpha^{i,ind} = \alpha_{\alpha\beta}^i F(A)_\beta^{total}$ where $\alpha_{\alpha\beta}^i$ as Equation C.2, and E_{AB} is the average molecular excitation energy given by $E_{AB} = \frac{E_A E_B}{E_A + E_B}$, where E_A is the ionization energy of molecule A, and D^{ij} is varied such that E_{rep} (Equation C.4) is always positive. The remainder E_{rep} (which behaves exponentially) is given by

$$E_{rep} = E_{int} - E_{elec} - E_{pol} - E_{disp} \tag{C.4}$$

where is the total from Equation 4.3. These terms are then grouped for the fitting, such that the total E_{rep} remains constant and is fitted to the Buckingham repulsion. The leading electrostatic term $T^{ij}(q^i q^j)$ is kept, where the q charges are those for the periodic framework. The difference $E_{int} - E_{rep} - T^{ij}(q^i q^j)$ gives the total attraction, which accounts for the higher order electrostatic moments, polarization, dispersion, and changes due to replacement of the

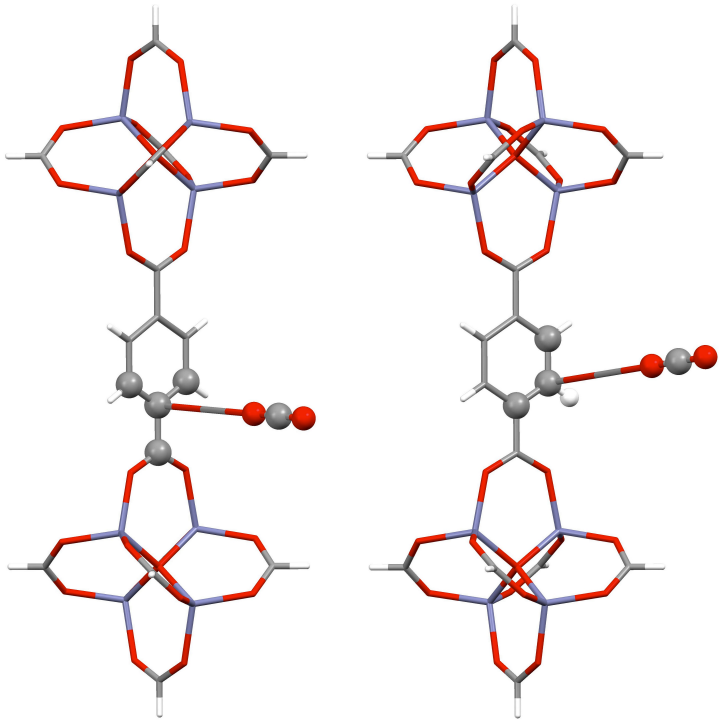

Figure C.10: (MOF-5) C_b atom type cluster (left) and C_d atom type cluster (right) with CO_2 approaching. Color and basis function contraction code: Purple (Zn) capped stick = 21s15p10d6f4g2h/4s3p1d, Red (O) ball = 14s9p4d3f2g /3s2p1d, Red (O) capped stick = 14s9p4d3f2g/2s1p, Gray (C) ball = 14s9p4d3f2g/3s2p1d, Gray (C) capped stick = 14s9p4d3f2g/2s1p, White (H) ball = 8s4p3d1f/2s1p, White (H) capped stick = 8s4p3d1f/1s.

charges in going to the periodic system. This remainder is fitted to the C and D attractive parameters.

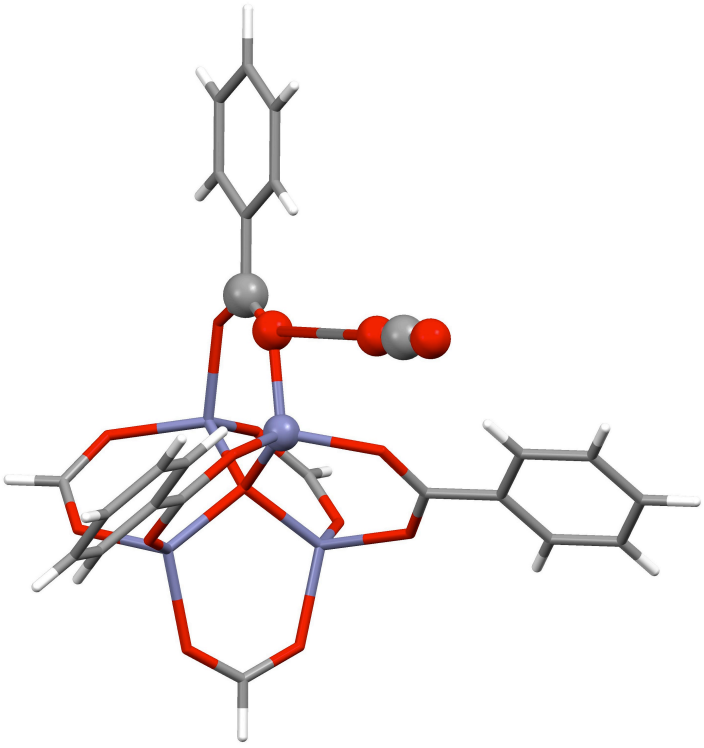

Figure C.11: (MOF-5) O_{ab} atom type cluster with CO_2 approaching. Color and basis function contraction code: Purple (Zn) ball = 21s15p10d6f4g2h/5s4p2d1f, Purple (Zn) capped stick = 21s15p10d6f4g2h/4s3p1d, Red (O) ball = 14s9p4d3f2g /3s2p1d, Red (O) capped stick = 14s9p4d3f2g/2s1p, Gray (C) ball = 14s9p4d3f2g/3s2p1d, Gray (C) capped stick = 14s9p4d3f2g/2s1p, White (H) capped stick = 8s4p3d1f/1s.

C.3 Force field parameters and charges

Pairwise potential parameters for the modified Buckingham potential model, Lennard-Jones potential model, and atomic partial charges are summarized in the tables below. Tables C.1, C.2, and C.3 give the repulsion (A, B) and attraction (C, D) parameters of the interactions between the MOFs and CO_2Ṫable C.4 gives the repulsion (A, B) and attraction (C, D) parameters of the interactions between the MOF and N2. Tables C.5-C.8 gives the charges for framework atoms. The Lorentz-Berthelot mixing rules were used for the interaction between any two different guest molecules. Charges and LJ parameters for the guest molecules were taken directly from TraPPE force field.[86]

Pairwise interactions		Force field parameters			
Framework	Molecule	A $\times 10^7$ K	B $Å^{-1}$	C $\times 10^5$ $KÅ^{-5}$	D $\times 10^5$ $KÅ^{-6}$
Mg	O_{CO_2}	4.067	4.152	0	4.062
O_a	O_{CO_2}	1.401	3.330	0.636	0
O_b	O_{CO_2}	1.673	3.520	0	0.891
O_c	O_{CO_2}	1.468	3.399	1.160	0
C_a	O_{CO_2}	2.280	4.065	1.445	0
C_b	O_{CO_2}	1.408	3.348	0	0.907
C_c	O_{CO_2}	2.139	3.786	1.194	0
C_d	O_{CO_2}	0.562	3.006	0	1.756
H	O_{CO_2}	2.153	4.180	0	0.824
Mg	C_{CO_2}	7.395	4.770	0	0
O_a	C_{CO_2}	23.047	4.990	0	0
O_b	C_{CO_2}	23.047	4.990	0	0
O_c	C_{CO_2}	23.047	4.990	0	0
C_a	C_{CO_2}	6.900	4.190	0	0
C_b	C_{CO_2}	6.900	4.190	0	0
C_c	C_{CO_2}	6.900	4.190	0	0
C_d	C_{CO_2}	4.584	4.050	0	0
H	C_{CO_2}	6.261	5.000	0	0

Table C.1: Pairwise parameters for the interactions between CO_2 and framework (Mg-MOF-74) atoms.

Pairwise interactions		Force field parameters			
Framework	Molecule	A $\times 10^7$ K	B $Å^{-1}$	C $\times 10^5$ $KÅ^{-5}$	D $\times 10^5$ $KÅ^{-6}$
Zn	O_{CO_2}	1.831	3.675	0	3.946
Zn	C_{CO_2}	8.205	5.000	0	0

Table C.2: Pairwise parameters for the interactions between CO_2 and framework (Zn-MOF-74) atoms.

Pairwise interactions		Force field parameters			
Framework	Molecule	A $\times 10^7$ K	B $Å^{-1}$	C $\times 10^5$ $KÅ^{-5}$	D $\times 10^5$ $KÅ^{-6}$
Zn	O_{CO_2}	24.53	5.000	0	1.228
O_{ab}	O_{CO_2}	1.957	3.600	1.052	0.018
O_{cent}	O_{CO_2}	5.121	4.040	0	1.684
C_a	O_{CO_2}	0.752	3.291	0	1.767
C_b	O_{CO_2}	1.771	3.527	0.403	1.742
C_d	O_{CO_2}	0.726	3.167	0	1.441
H	O_{CO_2}	2.153	4.180	0	0.824
Zn	C_{CO_2}	8.205	5.000	0	0
O_{ab}	C_{CO_2}	23.047	4.990	0	0
O_{cent}	C_{CO_2}	23.047	4.990	0	0
C_a	C_{CO_2}	6.900	4.190	0	0
C_b	C_{CO_2}	6.900	4.190	0	0
C_d	C_{CO_2}	4.584	4.050	0	0
H	C_{CO_2}	6.261	5.000	0	0

Table C.3: Pairwise parameters for the interactions between CO_2 and MOF-5 framework atoms.

Pairwise interactions		Force field parameters			
Framework	Molecule	A $\times 10^7$ K	B $Å^{-1}$	C $\times 10^5$ $KÅ^{-5}$	D $\times 10^5$ $KÅ^{-6}$
Mg	N_{N_2}	13.826	4.682	1.166	4.109
O_a	N_{N_2}	1.183	3.141	0	0
O_b	N_{N_2}	1.124	3.187	0	0.366
O_c	N_{N_2}	2.020	3.455	0	1.056
C_a	N_{N_2}	2.295	4.091	1.256	0
C_b	N_{N_2}	1.392	3.247	0	0.714
C_c	N_{N_2}	1.578	3.597	0	1.877
C_d	N_{N_2}	0.524	2.880	0	2.160
H	N_{N_2}	2.501	4.180	0	0.729
Mg	COM_{N_2}	0	0	0	0
O_a	COM_{N_2}	0	0	0	0
O_b	COM_{N_2}	0	0	0	0
O_c	COM_{N_2}	0	0	0	0
C_a	COM_{N_2}	0	0	0	0
C_b	COM_{N_2}	0	0	0	0
C_c	COM_{N_2}	0	0	0	0
C_d	COM_{N_2}	0	0	0	0
H	COM_{N_2}	0	0	0	0

Table C.4: Pairwise parameters for the interactions between N_2 and framework (Mg-MOF-74) atoms.

Atom	Charges $\lvert e \rvert$
Mg	1.5637
O_a	-0.7654
O_b	-0.7088
O_c	-0.8328
C_a	0.4820
C_b	-0.1354
C_c	0.1890
C_d	-0.1814
H	0.3891

Table C.5: Charges for Mg-MOF-74 atoms.

Atom	Charges $\lvert e \rvert$
Mg	1.55271
O_a	-0.77003
O_b	-0.7136
O_c	-0.83773
C_a	0.47603
C_b	-0.15132
C_c	0.20064
C_d	-0.14577
H	0.27731

Table C.6: Charges for Mg_2(dodpdc) atoms.

Atom	Charges $\lvert e \rvert$
Zn	1.4094
O_a	-0.7008
O_b	-0.6681
O_c	-0.7807
C_a	0.4812
C_b	-0.1237
C_c	0.1868
C_d	-0.1690
H	0.3649

Table C.7: Charges for Zn-MOF-74 atoms.

Atom	Charges $\lvert e \rvert$
Zn	1.3901
O_{ab}	-0.6583
O_{cent}	-1.4000
C_a	0.4681
C_b	-0.0398
C_d	-0.1352
H	0.23265

Table C.8: Charges for MOF-5 atoms.

Appendix D

Additional acknowledgements

Figures 2.4, 2.6, 2.8, and 5.1 were made with VMD software support. VMD is developed with NIH support by the Theoretical and Computational Biophysics group at the Beckman Institute, University of Illinois at Urbana-Champaign.